FACULTY OF SCIENCE
UNIVERSITY OF COPENHAGEN

Masters Thesis

Jack Christopher Hutchinson Rolph hkb266@alumni.ku.dk

Measurement of the total p-p cross-section using the ALFA detector at $\sqrt{s} = 13$ TeV

Supervisor: Peter Hansen

1st December 2017

Abstract

The total proton-proton cross-section was measured using data from the ALFA (Absolute Luminosity for ATLAS) detector using special high β^* optics and the optical theorem. This was achieved by measuring the differential elastic cross-section as a function of the momentum-transfer Mandelstam variable t and fitting to a Monte Carlo simulation including experimental effects by minimization of the χ^2 goodness-of-fit value with respect to parameters of interest. The preliminary total cross-section was measured to be:

$$\sigma_T = 105.716 \pm 0.129(\text{stat.}) \pm 1.295(\text{syst.}) \text{ mb} \quad (1)$$

The overall fit to data was poor. The measured cross-section was found to vary significantly depending on the time period chosen from data. The primary contribution to the poor χ^2 goodness-of-fit test was found to be in Arm 2 for the period $8 < \ell < 107$ over the entire fitting range. Furthermore, the background contribution exhibited anomalous peaks at approximately ± 5 mm in LHC x co-ordinates. This effect was also observed in unpaired bunches. No clear candidates for the causes of these effects were found.

Contents

List of Figures

List of Tables

Acknowledgments

I would like to begin by letting the reader know that, while life is rarely easy, there are certain battles that cannot be fought and won alone. I would like to tell you that my time at the Niels Bohr Institute has been as wonderful and kind to me as the people therein, but this would be a lie. The truth is that every day has been a struggle, through suicides, deaths, arrests, domestic troubles and financial insecurity in my family and the isolation of being in a foreign country while this has occurred. For this reason, I firstly find it of utmost importance to share with you, the reader, some of the individuals who have lessened the heavy weight of trial upon me with their kindness, wisdom and humanity.

I would firstly like to thank my advisor Peter Hansen, Jørgen Beck Hansen and particularly Simon Holm Stark for their continual guidance, support and friendship throughout my thesis. Furthermore, I would like to thank Sune Jakobsen, Christian Heinz, and Hasko Stenzel for all their fantastic support as part of the ALFA group. I also wish all the success in the world for my colleagues and friends: Henriette Petersen, Emil Bols, Alexander Lind, Nikolaj Sørensen and Bjarke Enkelund, who have been rays of sunshine throughout my time at the Niels Bohr Institute with their friendship and open ears. I also give thanks to my friends outside of work: Adomas Valentinas, Nicolas Taba and Karl Nyman, my stalwart companions in the Company of the Herb, with whom I have shared many fine hours rolling dice and spinning yarns. Finally, and most importantly, I thank my best friend in Denmark, Mantas Čepulkovskis and his lovely wife Arune Čepulkovskienė, who saved me in my time of need again and again with warmth unlike that which I have ever known. I pray that their marriage is blessed with the same happiness and hope that they have given me in my darkest hours.

This thesis is a testament to my battles against circumstance. Blood, sweat and tears went into every word, graph and table presented henceforth. There have been many moments of doubt throughout. However, though I may falter and stumble, I have never given up and will never give up. This is because I believe from the marrow of my soul that there is no future save the one we choose to build with our own hands. Of all the forces of nature, I feel that the potential arising from this belief is the only one that has driven this work to completion. In the darkness of despair or the fog of doubt and in spite of it all, I have learned to always tread towards the faint light of truth that sits low on the horizon.

This has been the hardest task of my life so far. I conclude by saying that I am proud to present the fruit of my work and that I hope you find the information that follows insightful and useful.

"I am a simple hunter, seeking one illusive mark,
wilier yet than any beast I've hunted in the dark.
I will not be bested, in spite of my quarry;
I shall pursue, from dawn till dusk, all that cannot be."

1 Introduction

"We're making a lot of progress, boy, but we ain't getting any farther."
– My Grandfather.

When a child asks: "Why is the sky blue?" or "Why do hot things glow?", they are asking questions that have confronted mankind for millenia but have remained unanswered until relatively recently. Today, the baffling question that scientists seek to answer for the hypothetical child of tomorrow is: "What is the really world made of?". In the pursuit of this knowledge, mankind has found itself delving ever deeper into the enigmatic world of our subatomic reality.

The Large Hadron Collider (LHC), the world's most powerful particle accelerator at the time of writing, spearheads this work at CERN (European Center for Nuclear Research). For example, ATLAS (A Toroidal LHC ApparatuS) and CMS (Compact Muon Spectrometer) were credited with the discovery of the Higgs Boson in 2012 [6], which helps to explain the nature of massive bosons. This has been one of the most important discoveries within the field of physics of the twenty-first century, providing ever more evidence that the Standard Model is a reliable and valid theory to describe nature. However, to this end, there are many theorized particles that may exist that have not yet been observed, such as Majorana neutrinos and WIMPs, as well as an array of potential particles that form the basis of the theory of supersymmetry.

Within high p_T hadron physics, the cross-section of an event represents the likelihood of that particular event to occur during a collision with a target or another beam. This is an important quantity within particle physics, as it dictates the probability with which one expects to observe a particular interaction. This thesis will measure the total p-p cross-section for a special LHC beam run at $\beta^* = 2.5$ km using elastic protons detected with the Absolute Luminosity For ATLAS (ALFA) forward physics detector. The many contributing aspects of this measurement will be discussed and analyzed henceforth, culminating in a measurement of the total p-p cross-section and two other parameters of interest: the ratio of the imaginary to real part of the nuclear scattering amplitude, ρ, and a parameterization factor, B.

2 Theory

2.1 The Standard Model

The Standard Model (SM) of particle physics is the most universally accepted theory of the elementary particles that exist within the universe, based on the framework of Quantum Field Theory (QFT).

The Standard Model is a theory that describes the matter of the universe as a set of particles, which are defined as quantized wave packets of the fields that cause the forces of nature. There are, at the time of writing, 12 elementary fermionic particles and their respective antiparticles from which all matter is composed and the five bosons by which the forces between them are mediated. The two main groups of particles may be described as follows: fermions, which have non-integer spin and bosons, which have integer spin. Of the fermions, there are two further groups: the quarks, which interact via gravity, the strong nuclear and electroweak forces and have non-integer charge and the leptons, which interact only through gravity and electroweak forces and have integer charge. Of the quarks and leptons, there are six *flavors*, which refer to the species of the particle in question.

The names, charges and spins of the particles of the Standard Model are shown in Figure 1.

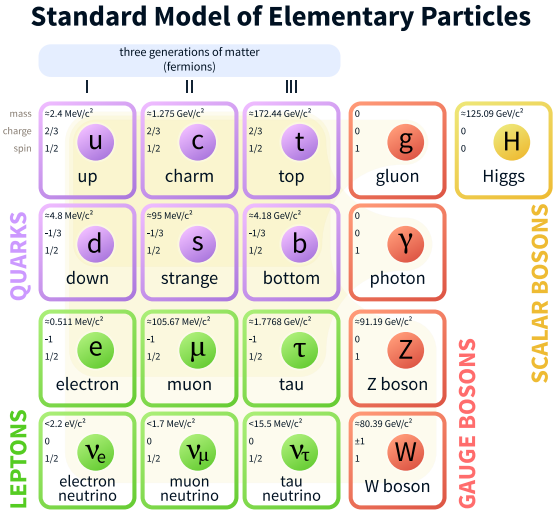

Figure 1: The Standard Model of particle physics. [1]

Particles carry degrees of freedom about how they interact with the fundamental forces of nature in the form of charges, a rational number that describes a degree of freedom for the particle to interact with a certain field. For example, both leptons and hadrons carry electric charge and therefore both interact with the electromagnetic force, yet leptons do not carry color charge and are thus 'invisible' to the strong force. Quarks, on the other hand, do carry color charge and therefore do interact via the strong force. There are six color charges: three normal charges and their anticharges. Particles consisting of quarks must always exist in a bound triad or pair that are both *color neutral* and referred to as hadrons. The triads are referred to as baryons and the pairs as mesons. A proton is, for example, a hadron consisting of two up quarks and a down quark and is therefore a baryon.

Bosons are the force-carrying particles of nature. The most recent addition to the Standard Model is the Higgs boson, which is a scalar boson. Within the context of QFT, the Higgs boson helps to explain the origin of mass for the Z and W gauge bosons by electroweak symmetry breaking.

The Standard Model fits so well to measurement that it is rarely considered to be a theory. However, there are still many unsolved problems, such as the nature of dark matter, that it cannot yet describe. As such, research is ongoing to extend the Standard Model to cover new physics.

2.2 QCD in Hadron Physics

In the context of high p_T particle physics, a hard process exhibits large momentum transfers between particles. In the case of proton-proton interactions, this type of process is able to probe the substructure of the particles. Soft processes exhibit low momentum transfers and probe at approximately the size of the proton. Elastic scattering is considered a soft process, whereas inelastic scattering is considered a hard process.

In the case of hard processes, the running strong coupling constant, α, decreases in magnitude to the extent that the interactions of said protons may be treated as a loosely bound collection of valence quarks, gluons and sea-quarks produced by gluon interactions. This is known as the *asymptotic freedom*. Furthermore, given these conditions, individual subcomponents of the proton may be treated as interacting independently of one another. This concept is known as the *QCD Factorisation Theorem*. The upshot of these theories is that the cross-section for a hard process may be estimated using perturbative Quantum Chromodynamics (pQCD). This represents the underlying process behind many of the theoretical calculations of new particles and processes in particle physics today. The only dimensionful parameter used in pQCD is [7]:

$$\Lambda_{QCD} \simeq 250 \text{ MeV} \tag{2}$$

It is required that the momentum transfer be many orders of magnitude larger than Λ_{QCD} in order to use pQCD. Soft processes, on the other hand, involve a much larger strong coupling constant, which prohibits the aforementioned perturbative method of cross-section calculation. The elastic p-p cross-section is a soft process and cannot be described with pQCD. As such, the measurement of the elastic p-p cross-section is instead achieved using the optical theorem, discussed in Section 2.4.

2.3 Luminosity and Cross-Section

Luminosity is a measure of the amount of incident radiation upon a given area, usually integrated over a period of time. The unit *barn* (100 fm^2) is a common unit used to measure interaction cross-sections in particle physics. Though this has the same unit as area, it does not represent the physical area of a subatomic particle. Rather, it it is an analogy for *effective probability* for a particle to interact via a given process.

The relationship between the number of expected events, N, for a given luminosity, $\mathcal{L}$ and a cross-section, σ is [8]:

$$N = \mathcal{L}\sigma \tag{3}$$

In the case of an accelerator such as the LHC, the luminosity of the beam may be derived as the number of particles that collide over all of the protons that interact at the LHC per revolution, per unit of area of the beam:

$$\mathcal{L} = \frac{n_{bunches} N_{B_1} N_{B_2} f_{rev}}{A} \tag{4}$$

Where $n_{bunches}$ represents the number of proton bunches, N_{B_1} and N_{B_2} are the number of particles in each bunch, f_{rev} is the frequency of revolutions of the LHC (currently 11.24 kHz) and the A is the area over which two beams overlap.

The measurement of the luminosity is very important for the calculation of cross-sections. This is because it provides the predominant error to any measurement of the cross-section. At present, Van der Meer scans are the most common tool for measuring luminosity.

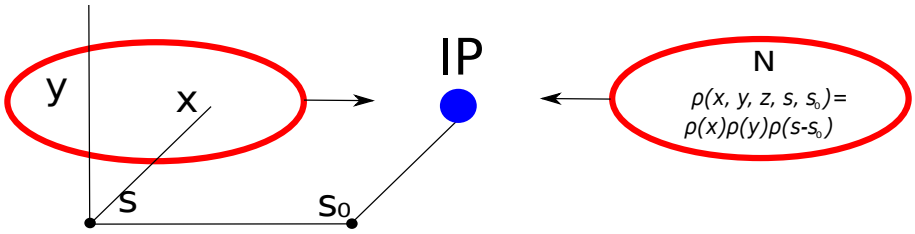

Figure 2: Diagram explaining luminosity. The red ellipses represent bunches of protons. Luminosity depends upon the number of particles in the bunch and their density therein. This is modeled as a product of Gaussian distributions.

2.4 The Optical Theorem

Measurement of the interaction cross-section (σ_T) may be achieved through the use of the optical theorem. This theorem was originally part of optical scattering theory before being developed for the case of two wavefunctions scattering.

Consider a propagating proton that scatters off some small perturbation within the LHC beam. Suppose now that this proton is elastically scattered from a collision or interaction with another particle. It is non-trivial to solve the Schrödinger equation analytically for proton collisions. However, it is possible to estimate a solution by separating the wave function into near and far field solutions.

The near-field case, which represents solutions close to the interaction point, renders little significance in regards to the final state of the scattered proton. However, in the far field case, both wavefunctions act as if they were free particles, as expected from an elastic scattering event; this limit is much closer to what is observed in nature. The total wavefuction, ψ_T, may be split into the incident wavefuction, ψ_I and the scattered wavefunction, ψ_S [9][10]:

$$\psi_T \simeq \psi_I + \psi_S \tag{5a}$$

Using the plane wave solution for the wave function, this may be rewritten as:

$$\psi_T \simeq e^{i(kz+\omega t)} + f(\theta)\frac{e^{i(kr+\omega t)}}{r} + O(\frac{1}{r^2}) \tag{5b}$$

Where $f(\theta)$ is the scattering amplitude of the proton at a given angle, θ. Upon calculating the probability distribution function of the wave function given, any higher order terms than those stated above may be neglected as they fall off as $\frac{1}{r^2}$. It is thus trivial to calculate the probability density function of this wave function, where $r = \sqrt{x^2+y^2+z^2}$.

We may expand r with respect to z using the Binomial theorem:

$$(1+x)^{\frac{1}{2}} = 1 + \frac{nx}{1!} + \frac{n(n-1)x^2}{2!}... \tag{6a}$$

$$r(z) = (x^2+y^2+z^2)^{\frac{1}{2}} \rightarrow z(1+\frac{x^2+y^2}{z^2})^{\frac{1}{2}} \tag{6b}$$

We may expand this as z tends to infinity by substitution of a test variable, z', where $z = \frac{1}{z'}$, since expanding $z' \rightarrow 0$ will yield the expansion of $z \rightarrow \infty$:

$$r(z) = z(1+z'^2(x^2+y^2))^{\frac{1}{2}} \tag{7a}$$

$$\frac{r(z)}{z} = (1 + z'^2(x^2 + y^2))^{\frac{1}{2}} \tag{7b}$$

Using the Binomial theorem and expanding to first order, since the distance in the z direction traveled by the proton is large relative to the angle at which it was scattered at:

$$(1 + z'^2(x^2 + y^2))^{\frac{1}{2}} = 1 + \frac{(x^2 + y^2)z'^2}{2} + O(z'^2) \tag{8}$$

Thus, we may revert to the original variable, z, to obtain an expression for r:

$$r(z) \simeq z + \frac{(x^2 + y^2)}{2z} \tag{9}$$

We may thus argue, assuming the scattering angle is small ($z = r\cos(\theta) \simeq r$), that the wave function may be rewritten as:

$$\psi_T \simeq e^{i(kz+\omega t)} + f(\theta)\frac{e^{ik\frac{(x^2+y^2)}{2z}}e^{i(kz+\omega t)}}{z} \tag{10}$$

The probability density function of the proton may be calculated by taking the modulus squared of the wave function, $P(r,t) = |\psi(r,t)|^2$. Using the new formulation of the wave function:

$$|\psi_T|^2 \simeq |e^{i(kz+\omega t)} + f(\theta)\frac{e^{ik\frac{(x^2+y^2)}{2z}}e^{i(kr+\omega t)}}{z}|^2 \tag{11a}$$

$$|\psi_T|^2 = 1 + f(\theta)\frac{e^{ik\frac{(x^2+y^2)}{2z}}}{z} + f^*(\theta)\frac{e^{-ik\frac{(x^2+y^2)}{2z}}}{z} + \frac{|f(\theta)|^2}{z^2} \tag{11b}$$

As previously argued, terms that vanish as $\frac{1}{r^2}$ may be neglected. Furthermore, using the fact that for a complex number c, $c + c^* = 2\mathrm{Re}(c)$:

$$|\psi_T|^2 = 1 + 2\mathrm{Re}(\frac{f(\theta)}{z}e^{ik\frac{(x^2+y^2)}{2z}}) \tag{12}$$

It has already been argued that the scattered wave is approximately traveling in the same direction as the initial plane wave. Using that the scattering angle, θ, tends to zero, one may calculate the probability of observing the scattered proton at infinity:

$$\int_{-\infty}^{\infty} |\psi_T|^2.dxdy = A + 2\mathrm{Re}(\frac{f(0)}{z}\int_{-\infty}^{\infty} e^{\frac{ikx^2}{2z}}.dx \int_{-\infty}^{\infty} e^{\frac{iky^2}{2z}}.dy) \tag{13}$$

Where A is the area spanned by a surface to which the particle may be seen to scatter. Assuming there exists some negligibly small imaginary component of the wave vector, k and using the identity, $\int_{-\infty}^{\infty} e^{iax^2} = \sqrt{\frac{\pi}{-ia}}$ for the limit $\mathrm{Im}(a) > 0$, we may find that:

$$\int_{-\infty}^{\infty} |\psi_T|^2.dxdy = A + 2\mathrm{Re}(\frac{f(0)}{z}\frac{2\pi z}{-ik}) \tag{14a}$$

$$\int_{-\infty}^{\infty} |\psi_T|^2.dxdy = A + \frac{4\pi}{k}\mathrm{Re}(if(0)) \tag{14b}$$

Finally, using the identity $\mathrm{Re}(ix) = -\mathrm{Im}(x)$, we arrive at the solution:

$$\int_{-\infty}^{\infty} |\psi_T|^2 . dxdy = A - \frac{4\pi}{k}\mathrm{Im}(f(0)) \tag{15}$$

We may interpret this result such that the coefficient A corresponds to the probability the scattered particles arrive at the flat surface in question, reduced by a function related to the scattering amplitude at low angles. The amount that the total intensity is reduced must therefore be the total cross-section:

$$\sigma_{tot} = \frac{4\pi}{k}\mathrm{Im}(f(0)) \tag{16}$$

The most important feature of Equation 16 is that the total cross-section is related to the imaginary part of the scattering amplitude where the scattering angle tends to zero. Note that this version of the cross-section is non-relativistic since the the wave vector, k, is not Lorentz invariant.

The differential cross-section is defined as:

$$\frac{d\sigma}{d\theta} = |f(\theta)|^2 \tag{17}$$

This result is important, as it instructs the manner in which the true cross-section may be measured.

2.5 Mandelstam t

This section deals with the nature of the Mandelstam variables and how the t variable may be extracted from observables of the LHC beam. Consider an event where two particles with four-momenta p_1 and p_2 interact and produce two daughter particles with four momenta, p_1', p_2'.

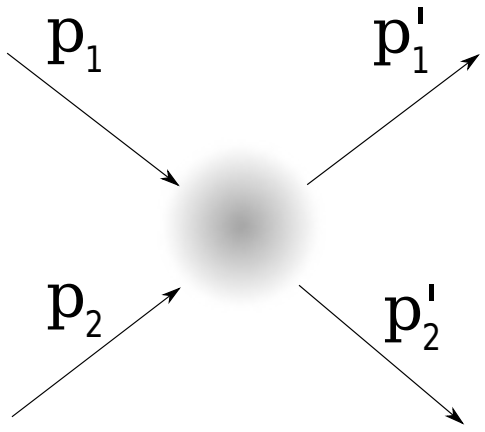

Figure 3: An example of an 2-2 event, from which the Mandelstam variables are defined.

The energy of relativistic particles, in natural units, is given by the relation:

$$E^2 = p^2 + m^2 \tag{18}$$

It is clear that such a system has requirements for the conservation of both energy and momentum. Using the fact that the total energy of a 2-2 scattering process must be conserved, we may state that:

$$p_1^2 = m_1^2 \tag{19}$$
$$p_2^2 = m_2^2 \tag{20}$$
$$p_1'^2 = m_2'^1 \tag{21}$$
$$p_2'^2 = m_2'^2 \tag{22}$$

Also, by conservation of momentum:

$$p_1 + p_2 - p_1' - p_2' = 0 \tag{23}$$

Using the previous relation, the following relations arise:

$$s = (p_1 + p_2)^2 = (p_1' + p_2')^2 \tag{24}$$

$$t = (p_1 - p_1')^2 = (p_2' - p_2)^2 \tag{25}$$

$$u = (p_1 - p_2')^2 = (p_1' - p_2)^2 \tag{26}$$

In particle physics, these are known as Mandelstam variables. These variables render the energies and momenta of a scattering process in a Lorentz-invariant manner. The momentum transfer between elastically scattered protons may be described by the Mandelstam t variable. It is also worthy of note that, with respect to the Mandelstam variables, $\sqrt{s}$ is equal to the centre-of-mass energy of the scattering process. This parameter is often used in particle physics to describe the collision energy.

Like the cross-section, the Mandelstam variable t itself is not a directly measurable quantity. It is possible, however, to relate Mandelstam t to the scattering angle of the process. Using the fact that p_1 and p_1' are four-momenta ($p = (E, -\overrightarrow{p})$), we may expand the expression for t thusly:

$$t = (E_1 - E_1')^2 - (\overrightarrow{p'}_1 - \overrightarrow{p'}_1)^2 \tag{27}$$

Since the protons have approximately the same energy in an elastic scattering process, the energy term may be neglected. Using that an identity for the product of two vectors, $A \cdot B = |A|^2 + |B|^2 - |A||B|\cos(\theta_C)$:

$$t = -|\overrightarrow{p}_1|^2 + -|\overrightarrow{p'}|_1^2 + 2\overrightarrow{p'}_1 \cdot \overrightarrow{p}_1 \tag{28}$$

$$t = -\overrightarrow{p}_1^2 + -\overrightarrow{p}_1'^2 + 2|\overrightarrow{p}_1||\overrightarrow{p'}_1|\cos(\theta_C) \tag{29}$$

The momenta in such an interaction are conserved, and in the case of the low momentum transfers associated with elastic scattering, are approximately the same as the momentum of the beam ($|p_1| = |p_1'| \simeq |p_B|$).

$$t = -2|p_B|^2 + 2|p_B|^2\cos(\theta_C) \tag{30a}$$

$$\therefore t \simeq -2|p_B|^2 + 2|p_B|^2(1 - \frac{\theta_C^2}{2}) \tag{30b}$$

$$-t \simeq |p_B|^2 \theta_C^2 \tag{30c}$$

where p_B is the beam momentum and θ_C is the forward scattering angle of the proton in question. Both of the quantities are observables that may be measured.

An analysis of elastic scattering from a stationary particle, such as a a beam gas proton, is discussed in Section 9.1.1.

2.6 Differential Cross-section

A theoretical function may be derived to describe the elastic differential cross-section. This provides a means to to measure the total cross-section. The proton may interact with the other proton in two ways: via the strong force or via electromagnetism. Consequently, the overall scattering amplitude is a combination of both interactions. The elastic differential cross section is related to the amplitude terms as follows:

$$\frac{d\sigma_{EL}}{dt} = |F_C(t \to 0)e^{i\alpha\phi} + F_N(t \to 0)|^2 \tag{31}$$

Where $F_C(t)$ refers to the Coulomb amplitude, arising from the electromagnetic interaction between the protons; $F_N(t)$ to the nuclear amplitude, arising from the strong force interaction between the protons and a complex phase, $e^{i\alpha\phi}$, corresponding to interference between these two effects where α is the fine-structure constant. These terms will be discussed henceforth.

2.6.1 Nuclear Interaction Term

The nuclear scattering amplitude describes the cross-section in terms of distances where the action of the strong force dominates. Currently, the calculation of the nuclear differential cross-section is impossible. The value is hence measured experimentally and fitted to a function.

At low values of Mandelstam t ($-t < 0.5GeV^2$), the function may be fitted to be of the form:

$$\frac{d\sigma_N}{dt} = \frac{d\sigma_N}{dt}|_{t\to 0} e^{-Bt} \tag{32}$$

Using this fact, we may derive that:

$$\frac{d\sigma_N}{dt}|_{t=0} e^{-Bt} = |F_N(t \to 0)|^2 e^{-Bt} \tag{33}$$

We can rewrite Equation 32:

$$\frac{d\sigma_N}{dt}|_{t=0} = |\mathrm{Re}(F_N(t \to 0)) + i\mathrm{Im}(F_N(t \to 0))|^2 e^{-Bt} \tag{34a}$$

$$\frac{d\sigma_N}{dt}|_{t=0} = |(\frac{\mathrm{Re}(F_N(t \to 0)}{\mathrm{Im}(F_N(t \to 0)} + i) \times \mathrm{Im}(F_N(t \to 0))|^2 e^{-Bt} \tag{34b}$$

$$\frac{d\sigma_N}{dt}|_{t=0} = |(\rho + i)\frac{\sigma_T}{4\sqrt{\pi}} e^{-\frac{Bt}{2}}|^2 \tag{34c}$$

$$\therefore F_N(t \to 0) = (\rho + i)\frac{\sigma_T}{4\sqrt{\pi}} e^{-\frac{Bt}{2}} \tag{34d}$$

Where ρ represents the ratio of the imaginary and real components of the scattering amplitude, $\rho = \frac{\mathrm{Re}(F_N(t\to 0))}{\mathrm{Im}(F_N(t\to 0))}$. ρ is an important parameter, as it is related to the imaginary part of the scattering amplitude which may be seen to compose the optical theorem definition of the total cross-section in Equation 16. The parameter B is a fitted parameterization factor. As of the writing of this thesis, it remains an open question as to whether or not the parameterization factor is, in fact, a polynomial or some other function than that which has been quoted.

2.6.2 Coloumb Term

The Coulomb interaction component of the scattering amplitude arises due to the fact that the proton is a charged particle, and will thusly interact with electromagnetic fields. Consequently, this term contributes to the total differential cross-section.

The Coulomb interaction may be described in terms of Quantum Electrodynamics (QED), which may be solved pertubatively. To qualitatively outline the main factors of the Coulomb interaction with respect to the Mandelstam t, we must consider that the protons exchange a virtual photon when interacting via the electromagnetic force. In short, depending upon the magnitude of the momentum transfer between the the protons, the wavelength of the photon will decrease. This is due to the photon propagator being related to the wavelength of the photon squared. In the case of this thesis, the momentum transfer is small and thus this effect has an important contribution to the overall scattering amplitude.

The best understood description for the Coulomb scattering amplitude argues that the proton may be described in terms of the dipole approximation. This is the argument that the interaction of light with the proton and vice versa may be estimated by the magnetic moment of the proton to first order. By taking the Fourier transform of the charge density of the proton and the dipole approximation, one may obtain the Electric Form Factor. This describes the relative change in strength of the proton interaction due to the fact that the point-like behavior of the protons is no longer a valid assumption. This quantity may be estimated to be:

$$G(t) = \left(\frac{\Lambda}{\Lambda + |t|}\right)^2 \tag{35}$$

$$\Lambda = 0.71 \text{ GeV}^2 \tag{36}$$

While this has been refuted as the complete description of the form factor, there is no existing model that currently describes data more accurately. Different parameterizations of the Form Factor exist [11]. In a particular parameterization, one may write the Coulomb interaction term as :

$$F_C(t) = \frac{-2\sqrt{\pi}\alpha G^2(t)}{|t|} \tag{37}$$

2.6.3 Coloumb-Nuclear Interference Term

The Coloumb Nuclear Interference phase term arises from the interference between Coloumb and Nuclear amplitudes. This term was first derived by West and Yennie [12] using first-order Feynman Diagrams with both nuclear scattering and Coulomb scattering. The phase term is given to be:

$$\phi(t) = -\gamma_E - \ln\frac{B|t|}{2} \tag{38}$$

$$\gamma_E \simeq 0.5\dot{7} \tag{39}$$

Other models do exist that do not rely on the assumptions made by phenomenological models, such as the exponentially decaying term in the nuclear interaction scattering amplitude with respect to Mandelstam t [13].

2.6.4 Elastic Differential Cross Section

To conclude, the elastic differential cross-section may be ascertained by solving Equation 31 and inserting the components discussed:

$$\frac{d\sigma_{EL}}{dt} = |F_C(t\to 0)e^{i\alpha\phi} + F_N(t\to 0)|^2 \tag{40a}$$

$$\frac{d\sigma_{EL}}{dt} = |\frac{-2\sqrt{\pi}\alpha G^2(t)}{|t|}e^{i\alpha\phi} + (\rho+i)\frac{\sigma_T}{4\sqrt{\pi}}e^{-\frac{Bt}{2}})|^2 \tag{40b}$$

$$= \frac{4\pi\alpha^2 G^4(t)}{|t|^2} - \sigma_t\frac{\alpha G^2(t)}{|t|}(\rho\cos(\alpha\phi(t)) + \sin(\alpha\phi(t)))e^{\frac{-B|t|}{2}} + \sigma_t^2\frac{\rho^2+1}{16\pi}e^{-B|t|} \tag{40c}$$

$$= \frac{d\sigma_C}{dt} + \frac{d\sigma_{CNI}}{dt} + \frac{d\sigma_N}{dt} \tag{40d}$$

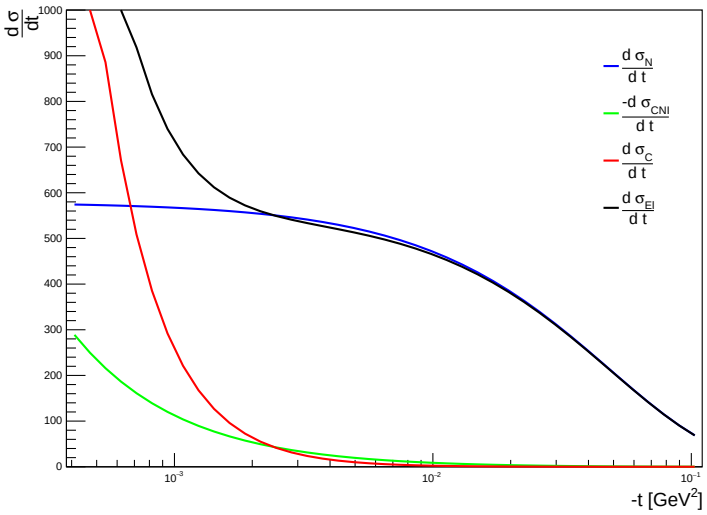

Figure 4: The total elastic differential cross-section decomposed into its constituent terms. The negative of the CNI component is shown for ease of reading. The components shown were calculated at $\sigma_{tot} = 105.716$ mb, $\rho = 0.119$, $B = 20.671$ GeV^{-2}

The total cross section is composed of three terms: the Coulomb term; the Nuclear term and the Coulomb Nuclear Interference term as shown in Figure 4.

An important point to note is that the elastic differential cross section with respect to Mandelstam t is directly proportional to the distribution of events observed at a given Mandelstam t:

$$\frac{d\sigma}{dt} = \frac{1}{L}\frac{dN}{dt} \tag{41}$$

2.7 The Froissart Bound

It is worthy of mention that it is possible to consider the maximum rate at which the total cross-section increases with the center-of-mass energy of the accelerator in question. This is known as the Froissart Bound on any total interaction cross-section. The primary result is that the cross-section ought not rise faster than $\ln^2(\sqrt{s})$, where $\sqrt{s}$ refers to the centre-of-mass energy of colliding protons within the model.

As of the publication of this thesis, it remains an open question in physics as to whether the rate of increase observed is the same or less than the Froissart Bound. While it is beyond the scope of this thesis to fully derive the relations, there are numerous derivations from a number of different standpoints of this limit [14]. This bound limits the resulting cross-section, and thus further instructs a reason to measure the cross section at new energies.

3 Apparatus

3.1 The Large Hadron Collider

The Large Hadron Collider (LHC) is a synchrotron particle accelerator located at the CERN (European Organization for Nuclear Research) complex in Geneva, Switzerland. At the time of writing, the LHC is the world's highest energy particle accelerator ($\sqrt{s} = 13$ TeV). The LHC has been instumental in various discoveries in the field of particle physics, most notably that of the Higgs Boson in 2012 [6]. A brief description of the LHC design will be given henceforth.

The LHC is a synchrotron. This is a machine designed to accelerate and collide charged particles. In the case of the LHC, the colliding particles are primarily protons but also other particles such as lead ions may be used. The particles are rotated about a ring 27 km in circumference and incrementally accelerated until they travel at speeds very close to the speed of light. When this has been achieved, the protons are collided together at a locations known as the *interaction points* (IPs), around which are located various detectors. In the LHC, the acceleration of protons involves a number of steps. Firstly, hydrogen gas is pumped into a chamber and ionised using a strong electric field. This leaves the positively charged protons available to accelerate. These protons are carried to Linac 2, the first accelerator of the group that feed the LHC. This is a linear accelerator, and accelerates to an energy of 50 MeV. They are then passed to various small synchrotrons; the Proton Synchrotron Booster (PSB), which accelerates to 1.4 GeV; the Proton Synchrotron (PS), which accelerates to 25 GeV and the Super Proton Synchrotron, which accelerates the protons to 450 GeV. At this point, the protons are passed into the LHC, wherein they are accelerated to the full 6.5 TeV currently achievable [15].

Synchrotrons are preferred for high energy physics over linear accelerators due to the fact that, in the former, the particle may be supplied with energy many times before collision. In contrast, a linear machine only allows the particle to be accelerated once. However, synchrotrons do have limitations. To achieve maximum collision energy, it is only feasible to accelerate hadrons due to synchrotron radiation: the energy radiated away from the accelerated particle in this form is a function of the Lorentz γ factor to the fourth power [16]. Since the mass of a proton is many orders of magnitude larger than that of an electron, it follows that an electron accelerated by the LHC would lose a very large amount of energy per turn compared to a proton; in reality, there is a factor of 10^{13} between the energy losses of the two particles. Consequently, high energy physics is nearly always performed with hadrons like the LHC, whereas non-hadron physics, such as e^+e^- accelerators, tend to be linear to avoid the aforementioned problem. A famous example of such an experiment was the Stanford Linear Accelerator at the SLAC National Accelerator Laboratory, in Menlo Park, California. However, non-hadron synchrotrons do and have existed, such as Large Electron Positron Collider (LEP) at CERN, which had a maximum collider energy of 209 GeV.

There are two main requirements for a particle accelerator to function: the actual acceleration of the protons and the control of the beam. Proton acceleration in synchrotrons and linear accelerators is achieved through feeding radio frequency (RF) packets into the accelerator tunnel from superconducting RF cavities, with frequencies ranging between 10MHz and 30GHz. Since the proton is a charged particle, it interacts with the RF source as a result of the Lorentz force. If a proton interacts with the RF wave out of phase, it accelerates. Should the proton arrive too late with respect to the frequency of the RF, it will experience a greater potential from the RF; conversely, should it arrive too early, the potential is less. This balances the acceleration out between protons, causing them to form *bunches* about the point at which a proton would be synchronous with the RF due to this effect. Protons in the LHC are injected with a spacing related to the frequency of the LHC in order that the protons always experience a potential in the LHC with respect to the RF. This region is called an *RF bucket*. There may be more than one bunch in an RF bucket. With respect to the injection chain, the Proton Synchrotron is responsible for ensuring that there is a 25 ns spacing between bunches.

In the case of beam control, the beam is bent into a circle and held in position by an array of powerful superconducting magnets, which prevent the beam from expanding in width and being destroyed. In the case of the LHC, there are 1232 main dipole magnets with a field strength of 8.33 T, which are used to keep the beam in the tightly confined beam pipe, which is only 4

cm in diameter. It should be noted that the LHC employs several types of magnets in order to confine the beam: the aforementioned dipoles, which are used for directing the beam; quadrupoles, which are used for focusing the beam and sextupole magnets, which are used to correct for the chromaticity of the beam. Chromaticity is an effect arising due to the fact that momentum dispersion causes variations in the amount the protons in the beam interact with the magnetic fields of the synchrotron. Since the theory of focusing the beam, or beam optics, are an integral part of the measurement of the proton interaction cross-section, the subject is discussed at length in Section 3.1.1.

There are four main experiments at CERN that use the LHC for collisions. These are CMS, ALICE, LHcB and ATLAS. The detector used in this thesis is one of the subdetectors of the ATLAS experiment, ALFA. Both of these detectors will be described in depth in Section 3.2 and Section 3.3.

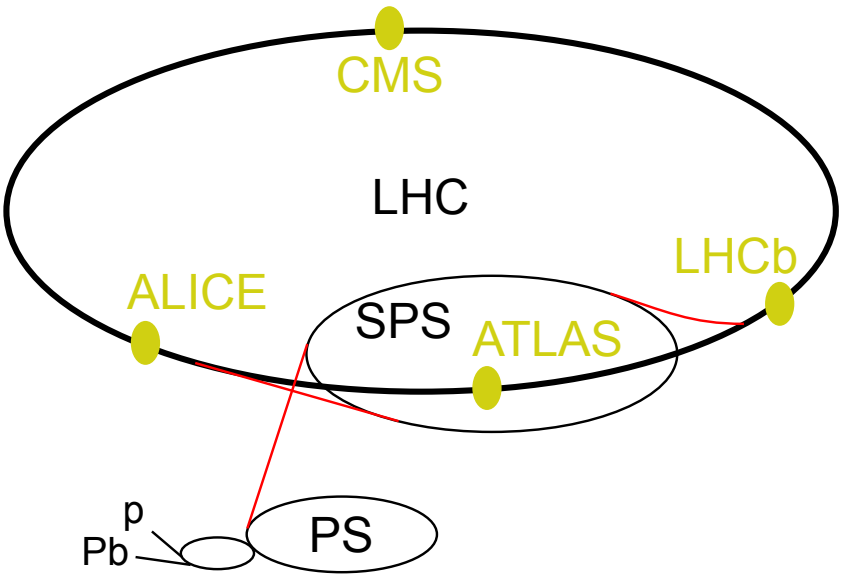

Figure 5: Schematic of the LHC with the approximate locations of the detectors shown. The *Pb* and *p* sections refer to the seperate injection of lead ions and protons [17].

3.1.1 Beam Optics

As previously discussed in Section 2.6, the Mandelstam variable, t, must be minimized as much as possible in order to be able to use the optical theorem. This corresponds to very low scattering angles, which may be achieved in the LHC by using special beam optics. The requirement for these beam optics in regards to the physics measured at ALFA is discussed henceforth.

The conditions for proton beam confinement may be found as solutions to Hill's Equation:

$$\frac{d^2u}{ds^2} + K(s)u = 0 \qquad K(s+L) = K(s) \tag{42}$$

where u is an arbitrary co-ordinate perpendicular to the beam axis, $K(s)$ is a restoring coefficient corresponding to the effects of the magnets, s is the co-ordinate along the beam axis and L refers to the circumference of the synchrotron.

The solutions to Hill's equation for accelerators is shown in Equation 43 with respect to the spatial component, u, an angular component, u'. This matrix is referred to as the *transport matrix*:

$$\begin{bmatrix} u \\ u' \end{bmatrix} = \begin{bmatrix} \sqrt{\frac{\beta}{\beta^*}}(\cos(\psi) + \alpha^* \sin(\psi)) & \sqrt{\beta\beta^*}\sin(\psi) \\ \frac{((\alpha^* - \alpha)\cos(\psi) - (1+\alpha\alpha^*))}{\sqrt{\frac{\beta}{\beta^*}}} & \sqrt{\frac{\beta}{\beta^*}}(cos(\psi) - \alpha\sin(\psi)) \end{bmatrix} \times \begin{bmatrix} u_0 \\ u'_0 \end{bmatrix} \tag{43}$$

The variables that compose Equation 43 are known as *Twiss Parameters*. Each component is related to the Beta Function, $\beta(s)$, which describes the position-dependent amplitude of the beam:

$$\alpha(s) = -\frac{1}{2}\frac{d\beta(s)}{ds} \tag{44a}$$

$$\gamma(s) = \frac{1 + \alpha(s)^2}{2} \tag{44b}$$

$$\psi(s) = \int_0^s \frac{ds}{\beta(s)} \tag{44c}$$

ψ refers to a phase advance of the beam, which is mentioned at various points throughout this thesis. Variables denoted with '$*$' represent values taken at the IP. It should also be noted also that the u variable may equally refer to either the x and y LHC co-ordinates, as these are independent.

Throughout this thesis, the matrix elements of the transport matrix are referred to using shorthand. A further point to note is that there are unique matrix elements depending on the direction and distance to the IP that the particle is being transported to. In this thesis, the transport matrix will be referred to as M. The individual components of the transport matrix will be denoted by further indices ($M^{A/C}_{ij,I/O}$), where A/C refers to the side of the IP, I/O refers to the inner or outer detector and ij is the index of the matrix element. Furthermore, where appropriate, the substitution $u' = \theta_u$. or the u component of the total proton angle, θ, is made implicitly henceforth.

A derivation of the minimum observable Mandelstam t at the ALFA detector is discussed henceforth [2]. For reference, the ALFA detector is discussed in Section 3.3.

The spatial part of the transport equation may be written to be:

$$u = \sqrt{\frac{\beta}{\beta^*}}(\cos(\psi) + \alpha^* \sin(\psi))u^* + \sqrt{\beta\beta^*}\sin(\psi)\theta^*_u \tag{45}$$

It is worth noting that, for optimal ALFA running conditions, $\psi \simeq \frac{\pi}{2}$ and $\alpha^* \simeq 0$. We see that the result of this is that the co-ordinate has negligible dependence on the initial vertex of the proton collision. This is known as *parallel-to-point optics*. At present, this effect is only achievable for the y co-ordinate.

Since we are considering elastic scattering, whereby elastically scattered protons carry the same momentum on either side of the IP (*back-to-back* scattering), we expect the total angle between the two to be equal with opposite sign. Thus, we may state:

$$u_L - u_R = 2\sqrt{\beta\beta^*}\sin(\psi)\theta^*_u \tag{46a}$$

$$\theta^*_u = \frac{u_L - u_R}{2\sqrt{\beta\beta^*}} \tag{46b}$$

Using the definition of the Mandelstam variable in Equation 30c, we may argue that:

$$-t_{min} = (p\theta_{min})^2 = \frac{p^2 y_d^2}{\beta\beta^*} \tag{47}$$

where y_d is the minimum possible distance between the detector and the beam ($y_L - y_R = 2y_d$).

The detectors are placed at a distance in the order of beam widths from the beam. The size of the beam spot is:

$$\sigma = \sqrt{\epsilon\beta} \tag{48}$$

Therefore, the minimum distance to the beam in terms of the number of beam widths, n_d, is:

$$y_d = n_d\sqrt{\epsilon\beta} \tag{49}$$

Hence, the minimum Mandelstam t may be derived:

$$-t_{min} = p^2 n_d^2 \frac{\epsilon}{\beta^*} \tag{50}$$

Having derived an expression for the Mandelstam variable t, we are now able to see which variables contribute: the emittance, ϵ; the distance to the beam in multiples of beam spot size, n_d and the Beta Function at the IP, β^*. In reality, the minimum Mandelstam t value observable is limited to the distance that the ALFA *Roman Pots* (RPs, see Section 3.3.4) would receive too much radiation or potentially come into direct contact with the beam. This true distance is in the order of millimeters. Consequently the detection of Mandelstam t is limited to the order of 1×10^{-4} GeV^2.

3.1.2 β^* Parameter

The Twiss Parameter β^* describes how tightly the beam is confined at the interaction point of a synchrotron collider. It is sometimes defined as the distance from the IP after which the beam width has doubled. During normal LHC operation, the β^* is typically reduced to the order

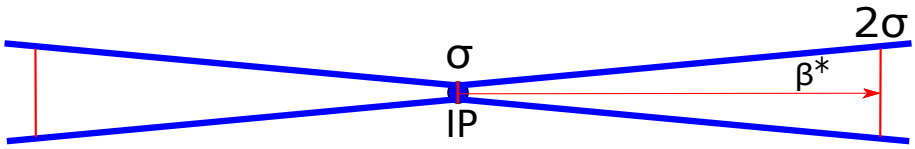

Figure 6: Diagram explaining the concept of β^*. The blue lines represent the limits of the beam. Red lines represent measurements. σ refers to the width of the beam at the IP.

of tenths of meters in order to maximize the number of collisions and to consequently observe as many rarely occurring processes as possible. In the case of elastic scattering, very different requirements exist. It is clear from Equation 50 that the minimum Mandelstam t value observable reduces as β^* increases. In summary, a large β^* allows much smaller elastic scattering angles and therefore a probe into the t distribution at these low values, as the divergence of the beam is significantly reduced in this case.

3.1.3 Emittance

The emittance of the LHC beam refers to the width of the spread of the LHC beam in a phase space of momentum and position wherein 95% of protons in the beam reside. The variables map an ellipse in the phase space. This quantity is important, as it helps to describe the physical size of the beam.

The emittance is defined as [8]:

$$\epsilon = \gamma u^2 + 2\alpha u u^{'} + \beta u^{'2} \tag{51}$$

Where u and $u^{'}$ are the position and angular co-ordinate respectively, while α, β and γ are the *Twiss parameters* that define the solutions for the equation of motion of the beam. The limits of the beam in the phase space may be found to be:

$$u_{max} = \sqrt{\epsilon\beta} \tag{52a}$$

$$u^{'}_{max} = \sqrt{\epsilon\gamma} \tag{52b}$$

The emittance of the beam is measured by wire scans. This process achieves a measurement of the beam spot size by passing a wire through the beam. The wire is moved to different positions throughout the beam, causing protons to scatter away. Scintillators then measure these particles. Thus, a distribution can be generated which mirrors the physical parameters of the beam profile.

For reference, the normalized emittance, or emittance normalized to the absolute size of the beam, is defined as:

$$\epsilon_N = \beta\gamma\epsilon \tag{53}$$

where β and γ refer to the Lorentz factors, $\gamma = \frac{E}{m}$, $\beta = \frac{v}{c}$.

3.2 The ATLAS Detector

The ATLAS Experiment (A Toroidal LHC ApparatuS) is a multipurpose particle detector designed to capture as much information as possible on the particles produced by the collisions in the Large Hadron Collider (LHC). It is one of the several experiments at CERN, and is used for general-purpose particle physics research.

3.2.1 Detector Design

ATLAS is composed of many subcomponents, the most important and relevant of which are discussed henceforth [18].

The Inner Detector is closest to the beam, extending to a maximum of 2.1 meters away from the center of the beam pipe. The purpose of this detector is to measure the charged tracks from particles passing through the detector such that they may be distinguished from the neutral particles later in the experimental process, as well as information that enables the calculation of important parameters such as the initial vertices of a decay and the transverse momentum. This layer consists of three components: the Semiconductor Tracker (SCT), Pixel detector and Transition Radiation Tracker; these all work in concert with one another to provide accurate information about the initial positions and momenta of charged particles within the detector. Closest to the beam is a seperate detector called the Insertable B-Layer (IBL), an additional pixel layer designed to measure tracks, specifically for B-tagging, yet also protect the other delicate components in the LHC tracking layer from the significantly higher luminosity of the Phase-II runs. The IBL has a lifetime of around 300 fb^{-1}, or 5 years of LHC operation [19].

Calorimeters follow the tracking layer, measuring the energy of the particles produced by the LHC. In the case of ATLAS, this stage is the Liquid Argon Calorimeter (LAr) and Tile Hadronic Calorimeter (TileCal). The LAr uses liquid argon, kept at -183°C as a scintillator. This part of the detector also extends to the end cap region of the detector. The TileCal performs a similar task. The LAr is used for electromagnetic calorimetry and the TileCal is used for hadronic calorimetry.

Relevant to this thesis are the Minimum Bias Trigger Scintillators, which consist of a set of 2 cm thick polystyrene discs mounted at $z = \pm 3.7$ cm from the IP. This detector has a broad coverage

in detector phase space ($2.08 \leqslant |\eta| \leqslant 2.78$ for the outer layers, $2.78 \leqslant |\eta| \leqslant 3.75$ for the inner detectors, where η is the pseudorapidity, a Lorentz-invariant co-ordinate representative of the angle of a given particle with respect to the beam axis) [20]. As such, they fire on nearly all inelastic events; this is useful when measuring elastic background in order to determine whether or not said event was caused by a diffractive-type event or from the beam halo.

The outermost layer of the detector is called the Muon Spectrometer. Muons before this point rarely interact, and hence the muon spectrometer is placed furthest from the detector. The Barrel Toroid and End Cap Toroid are used to bend the muon, while drift chambers, resistive plate chambers and other components are used to measure the position of a passing muon.

The Magnet system bends charged particles produced by LHC collisions in order to separate them from neutral particles. This component consists of the Central Solenoid Magnet, the Barrel Toroid and the End Cap Toroid. The Central Solenoid of this part of the detector has a field strength of around 2 T, while the other two have one of around 4 T. These magnets are superconducting and as such are kept at 4.7 K.

This coverage is sufficient to observe and track many of the particles of the Standard Model. Particles and resonances which are too short-lived to detect directly are detected via their decay products, while any remaining particles such as neutrinos are detected through missing energy from decays, which is achieved using sophisticated computational techniques that reconstruct the events from tracking and calorimeter data.

There are two detector experiments dedicated to the measurement of forward physics at ATLAS. LUCID (Luminosity Measurements Using Cherenkov Radiation) is placed ± 17 m from the ATLAS IP, with a pseudorapidity range of of $5.6 \leqslant |\eta| < 6$. LUCID detects protons using Cherenkov light, which is detected via photomultiplier tubes to amplify the signal [21]. ALFA (Absolute Luminosity for ATLAS) is discussed at length in Section 3.3. In brief contrast, ALFA is able to observe much more forward protons and uses scintillating fibers.

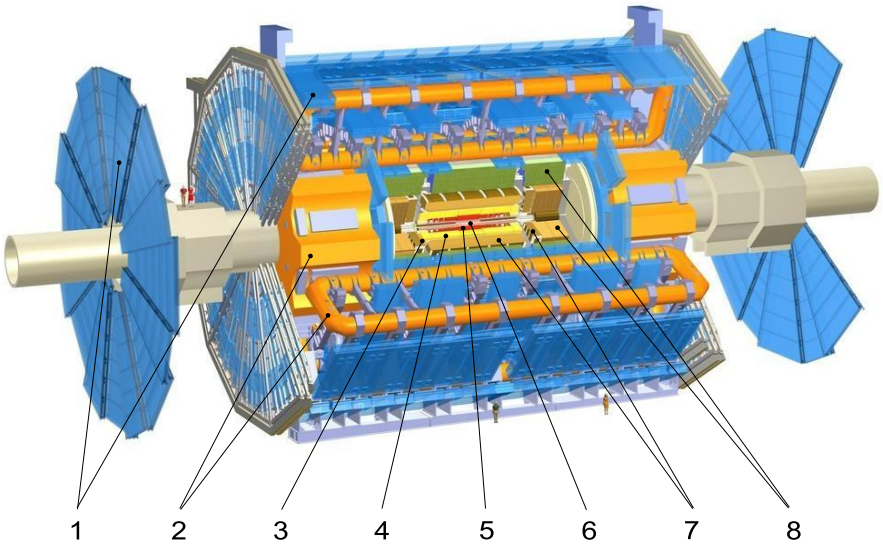

Figure 7: Schematic of the ATLAS Detector with labeled subcomponents:
1. Muon Detectors Magnet system 2. Toroid Magnets; 3. Solenoid Magnet Inner Detector; 4. Transition Radiation Tracker; 5. Semi-Conductor Tracker; 6. Pixel Detector Calorimeters ; 7. Liquid Argon Calorimeter; 8. Tile Calorimeter. [22]

3.2.2 Data Acquisition and Triggers

The LHC delivered an integrated luminosity of 35.8 fb^{-1} of collisions in 2016 [23]. This represents the largest amount of events per femtobarn of cross-section than has ever been previously available in an accelerator, and thus increases the amount of data available to use for analysis. However, at

present, it is impossible to store each and every event that is produced by a collision. In reality, only a hundred out of a billion events are ever stored by the ATLAS Data Acquisition Process (DAQ) and this is achieved through the use of a set of conditions that an event must pass in order to qualify as an 'event of interest'. The part of the DAQ responsible for the management of these conditions are known as triggers. In ATLAS, there are three levels of trigger resolution, each for consecutively more specific and computationally intensive conditions. These are known as Levels 1, 2 and 3 respectively.

The Level 1 Trigger is the first layer, and applies simple binary conditions upon which to trigger. For example, a commonly used tool for the estimation of background events in ATLAS is the bunch group trigger, which fires randomly throughout the run. Triggers can be a broad range of parameters and always consist of hardware-based solutions. These triggers are passed to the Central Trigger Processor (CTP), which has access to the information about other detectors. The CTP may also be used to regulate the flow of information by using prescales. If a prescale is applied, only one of a given number of events with a certain trigger will be passed to the next level. If the event passes at this level, it goes to Level 2, which admits more complex trigger criteria and involves processes such as jet reconstruction. Finally, the Level 3, or High Level Trigger, reconstructs the entire event, and admits the event to either pass or fail the full selection criteria. This data is then written to physical storage media.

3.3 The ALFA Detector

3.3.1 Detector Summary

Elastically scattered protons at ATLAS tend to have a minimum scattering angle in the order of tens of microradians. The ALFA Detector (Absolute Luminosity for ATLAS) is a very forward instrument used for the detection of such protons. The ALFA detector has been designed in order to be able to resolve very forward protons as well as is possible. This is paramount for the measurement of the p-p cross-section through the optical theorem. The detector is also used in other forward physics research, such as studies of diffractive physics.

ALFA is located at the end of the straight part of the LHC beam pipe around which ATLAS is located, with detectors located on either side of the IP. ALFA is able to measure significantly higher pseudorapidity regions than ATLAS. For comparison, the ATLAS Calorimeter has a maximum pseudorapidity coverage of $\eta = |4.9|$, while the ALFA Detector observes particles produced at $\eta > |8.3|$. This is ideal to measure elastically scattered protons and other processes that exhibit low momentum-transfer.

There are eight detectors at ALFA, consisting of two pairs of detectors for each side of the IP. The sides are denoted by 'A' in the direction of $+z$ in LHC co-ordinates from the IP and 'C' for the other side. The detectors are located at distances of 237 m and 245 m from the IP for the innermost and outermost pairs respectively. The naming convention and general information about each detector are listed in Table 3.3.1. The layout of the detector is represented in Figure 8. Furthermore, throughout this thesis, the information shown in many figures is described with respect to a diagram representing ALFA. This diagram is shown in Figure 9.

Detector	Arm	Number	Side	Orientation	Distance
B71LU	1	1	A	Upper	245 m
B7L1L	2	2	A	Lower	245 m
A71LU	1	3	A	Upper	237 m
A7L1L	2	4	A	Lower	237 m
B71LU	2	5	C	Upper	237 m
B7L1L	1	6	C	Lower	237 m
A71LU	2	7	C	Upper	245 m
A7L1L	1	8	C	Lower	245 m

Table 1: Table of information about the detectors that compose ALFA.

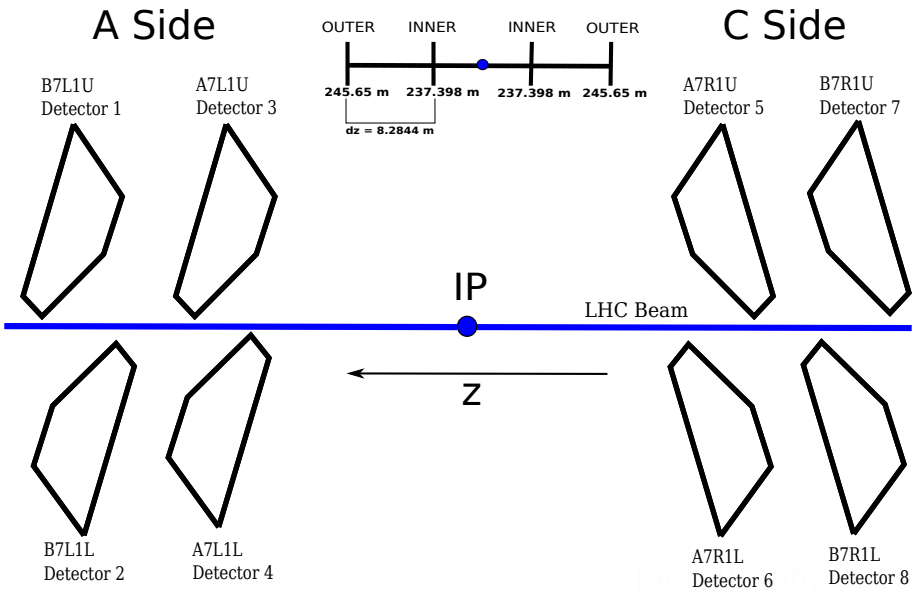

Figure 8: Representation of the ALFA detectors with respect to the IP. Information about individual detectors also shown in Table 3.3.1 is shown.

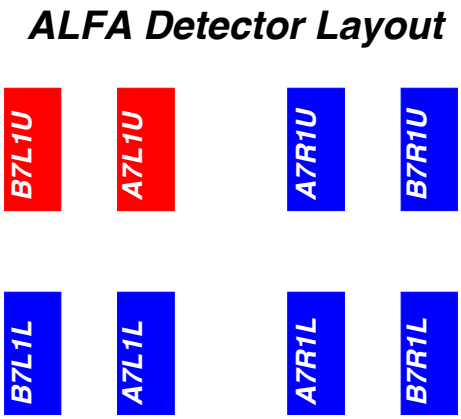

Figure 9: Representation of the layout of the ALFA detector appended to various figures throughout this thesis. The squares represent the detectors of ALFA. The red squares represent the detectors used in the figure. In this instance, the diagram refers to the upper station on the A side, B7L1U-A7L1U.

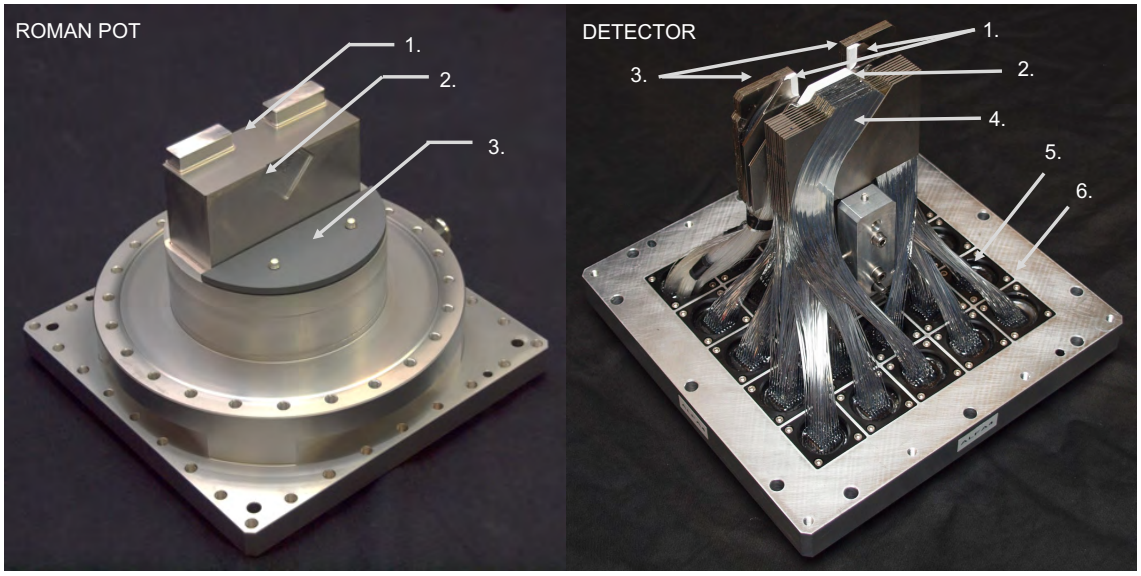

Figure 10: Pictures of the Roman Pot and Detector [2].
Roman Pot: 1. Thin MD window; 2. Thin wall in front of detector; 3. Ferrites.
Detector: 1. Overlap Detector (OD) Trigger Tiles; 2. Main Detector (MD) Trigger Tiles; 3. Overlap Detectors (OD); 4. Main Detectors (MD); 5. Fiber Connector; 6. Base Plate

3.3.2 Main Detectors

A Main Detector (MD) consists of 64 square scintillating fibers of side length 0.5mm which have been applied to either side of a titanium plate stacked in layers of 10. This forms a set of 20 fiber layers, where the direction of the fibers in the layer glued to the front of the titanium substrate is perpendicular to that of the back. The overlapping points of the fiber layers form detector 'pixels' of 500×500 μm^2. The fibers on either side of are also skewed slightly by a small offset, corresponding to 50 μm, or a tenth of the width of a fiber. Each of these fibers has a resolution of around 0.3 μm , which is adequate in order to resolve protons that are scattered at very low angles. Protons cause the fiber to scintillate and this the light is guided by the fiber to a Multi-Anode Photomultiplier Tube (MAPMT) which produces a signal. The MD is shown as a labeled component in Figure 10.

3.3.3 Overlap Detectors

The Overlap Detectors (ODs) are used for the purpose of detector alignment between the upper and lower stations. The process of aligning the detectors is discussed in Section 3.3.8.

Many features of the overlap detectors (ODs) are very similar to the MDs. The OD consists of two sections of 30 scintillating fibers glued to a titanium substrate in the same manner as the MD. The ODs are staggered in three layers in order to increase the resolution of the detector. The second layer is staggered at 166 μm and the third layer is staggered at 333 μm. They are placed on each side of the center of the detector, and are designed such that, for two adjacent detectors, the ODs of the upper pot overlap those of the lower pot. This is shown in the perspective diagram in Figure 16. The ODs start to overlap when the RPs are moved within 8.5 mm of the beam axis and fully overlap at 15 mm [3].

In order to allow for their position in the detector, the fibers must be bent around in order to connect to the MAPMTs, which leads to a significant loss in resolution in certain regions of the detector. The spectrum of resolution ranges between 1 μm and 380 μm. Consequently, the only available region for measurement is that area in which the fibers are not bent, which corresponds to an area of 15×6 mm^2 that may be used to measure protons. A further contrast is the inclusion of a layer of titanium between the layers in the OD. This is in order to increase the probability of a particle shower occurring in the detector in order to ensure that there is a high likelihood of an event being observed. The OD is shown as a labeled component in Figure 10.

3.3.4 Roman Pots

The Roman Pot (RP) is the housing for the ODs and MDs, designed to isolate the two parts of the detector from the LHC hard vacuum while allowing the MD and OD regions as close to the beam as possible. The Roman Pot is so-named as homage to the Italian physicists at the CERNRome Group who worked on the design of the RP in order to study similar physics in the Intersecting Storage Rings (ISR), a precursor to the LHC. The 'Pot' aspect of the name refers to the cylindrical container in which the MD and OD is placed. In order that the fibers in the detector may be placed close to the beam as possible while minimizing damage, the RP window and walls that surround the detector are thinner than elsewhere. Nonetheless, these cause a loss of resolution for the outer detectors corresponding to around an additional 3 μm of uncertainty on the position of the protons. To prevent the material warping under pressure, a secondary vacuum is used in ALFA. The Roman Pots have adjustable positions, allowing for movement accurate to the order of 1 μm, in order to minimize the amount of radiation received during normal beam operation and to get as close to the beam as possible during operation. The Roman Pot is shown in Figure 10.

3.3.5 ALFA Trigger

As with the ATLAS trigger, the main purpose of the ALFA trigger is to rapidly determine whether or not a pair of scattered protons from the IP had qualities of interest, such as being elastic. As such, signals received from the ODs and MDs must be processed within a very short timescale, generally in the order of nanoseconds, to select the optimal events for further processing. There are two 3 mm scintillating plastic tiles that are used to trigger in ALFA. These tiles cover the active OD region of the detector. The trigger requires a co-incidence of two such fiber plates in order to fire; this is sufficient to reduce the effect of the MAPMT noise. The MAPMT output is then passed to the ATLAS CTP, which receives a trigger signal for each of the pots, which is then combined with respect to co-incidences of interest that are then recorded.

It is important to note that the output from ALFA comes in two streams: the calibration stream and the physics stream. Due to the nature of the ATLAS trigger, prescales are often used to reduce the flow of data to a manageable level. The calibration stream was used in this thesis. This is because only trigger information and ALFA data is recorded in the calibration stream and therefore may be used unprescaled due to faster read-out rates, which is important for background analysis. The physics stream, on the other hand, contains all the information from ATLAS and has a much slower read-out rate, and requires co-incidences between the triggers in ALFA in order that the event may be stored without prescale. In either case, the L1_ALFA_ELAST15 and L1_ALFA_ELAST18 trigger efficiency is great enough and the trigger rate low enough that they may be used unprescaled in the physics stream. The trigger efficiency is discussed in Section 5.10.

Name	Logic
L1_ALFA_ELAST11	B7L1U AND A7L1U AND A7R1L AND B7R1L
L1_ALFA_ELAST12	B7L1L AND A7L1L AND A7R1U AND B7R1U
L1_ALFA_ELAST13	(B7L1U OR A7L1U) AND A7R1L AND B7R1L
L1_ALFA_ELAST14	B7L1U AND A7L1U AND (A7R1L OR B7R1L)
L1_ALFA_ELAST15	**(B7L1U OR A7L1U) AND (A7R1L OR B7R1L)**
L1_ALFA_ELAST16	(B7L1L OR A7L1L) AND A7R1U AND B7R1U
L1_ALFA_ELAST17	B7L1L AND A7L1L AND (A7R1U OR B7R1U)
L1_ALFA_ELAST18	**(B7L1L OR A7L1L) AND (A7R1U OR B7R1U)**

Table 2: Table of the names and logic of elastic trigger items. The boldface entries are the loosest elastic triggers and the ones used for elastic analysis in this thesis.

3.3.6 Co-ordinate System

Within the context of a data analysis setting, an important feature of the MDs is the co-ordinate system. The scintillators run at $\pm 45^\circ$ to the LHC co-ordinate system, which a design feature to

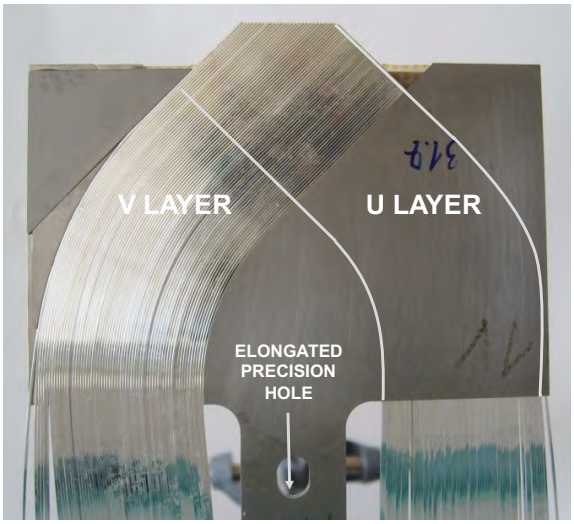

Figure 11: The U and V layers of ALFA. The V(U) Layer is glued to the front (back) of the titanium substrate. The precision hole is shown. [2].

maximise the detector acceptance region. This is referred to henceforth as U-V co-ordinates. The co-ordinate system in the detector is measured from a precision hole at $y = -135$ mm [4]. The values may be adjusted for alignment as discussed in the Section 3.3.8.

3.3.7 Track Reconstruction

The reconstruction of tracks at ALFA is achieved through the fact that protons striking the detector penetrate multiple fiber layers and consequently a signal from an elastic proton will cause a signal in the fibers that overlap in these layers. The position of the proton in a fiber is determined by finding the Gaussian distribution of the locations where a particle was detected in the fiber and taking the average position. As previously mentioned, the fibers in the MD are skewed by around $50\mu m$, and, as such, events that are well defined within the detector ought to interact with fibers within multiple fiber layers in the MD. Furthermore, the theoretical resolution (14.4 μm) is heavily influenced by the effect of fiber cross-talk[2].

As discussed in Section 5.1.2, simultaneous detections of protons lead to multiple reconstructed tracks. For this reason, the track combinations are ranked by likelihood when recorded.

The passage of the proton through the detector, assuming it is elastic, will be almost parallel from the first layer to the last, traversing multiple layers in the MD and causing multiple fibers to scintillate. As such, any track reconstruction attempt must take into account the number of overlapping fibers in the reconstructed track and the number of recorded fiber hits that were detected from each of the fibers in a layer. The minimum criteria for a track to be reconstructed in ALFA are three overlapping fibers in the U plane and V plane and three U and V-layers with between one and three fiber hits in each. The exact specifics of the track quality criteria used in this thesis are discussed thoroughly in Section 5.1.

3.3.8 Alignment

3.3.8.1 Beam Based Alignment

As is often the case in experimental physics, analyses must account for the limitations of the detector itself. It is often the case that the ALFA Detector can become misaligned such that it may be skewed at a small angle to the beam, or the center is offset by some small amount, for example. For safety reasons, the RPs are moved away from the beam when not in operation, as the electronics of the detector are not radiation hard and may be damaged otherwise. However,

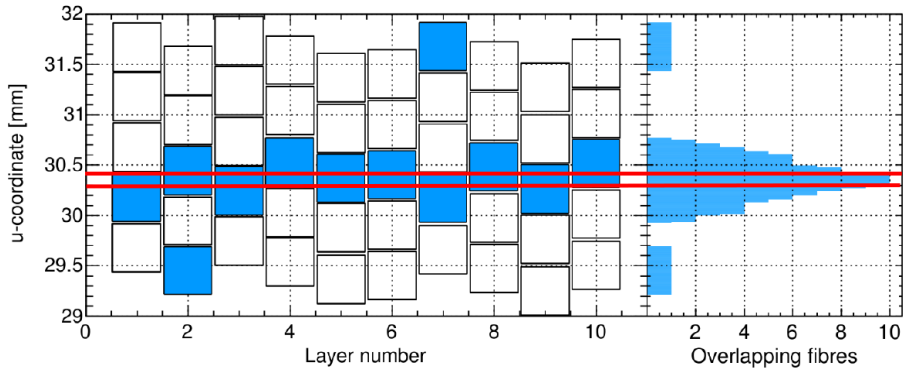

Figure 12: A representation of the reconstructed track from individual fiber hits in the ALFA MD [2].

this leads to the problem that the servos that move the detector, although precise to microns, contribute systematic error to any measurements taken.

At the beginning of a run, the RP is lowered into the beam pipe in increments of $5 - 10$ μm until the very edge of the RP touches the beam halo. As soon as the RPs come into contact with the edge of the beam, protons scatter from the RP, which will be observed by LHC Beam Loss Monitor. This signifies the point at which the position of the RP is known relative to the beam and the detector is then moved into a data-taking position. The entire process must be completed for all the RPs of ALFA and takes two to three hours. The data-taking position is of the order of several $\sigma_{nominal}$, which refers to the beam width of a normal LHC run where the emittance is 3.5 μrads $\cdot$ mm. This is to protect from accidental 'beam blow-up' whereby the emittance of the beam suddenly increases, potentially damaging ALFA.

3.3.8.2 Distance Measurement with Overlap Detectors

Intra-detector alignment between the upper and lower RPs is achieved by comparing measurements between the y positions measured in the ODs of each set of detectors. This is performed to find the distance between adjacent detectors. The ODs are placed far enough away from the MD such that only beam-halo events are expected to be observed there. Consequently, by measuring the limits of the distribution of beam halo particles in the ODs of both detectors, the distance between the adjacent detectors may be measured [2]:

$$\overline{y}_{det} = \sum_{i=1}^{N} \frac{y_i^{lower} - y_i^{upper}}{N} \tag{54}$$

where $y_i^{upper/lower}$ is the y value of an event, i, in the upper/lower OD detector, and N is the number of events. From this value, the distances between the MDs can be inferred from the difference between the known distances between the top and bottom of the MD and the distance between the beam halo average and the top and bottom of the MD. This is shown in Figure 16. The distances between the top and bottom of the MDs, D_{low} and D_{high}, are known quantities. The distance between the beam halo average and the top of the MD, d_{low} and d_{high}, are calculated from knowledge of the beam halo average, $\overline{y}_{det}$, shown in Equation 54. It should be noted that the distance measurement is not the whole picture, as there may be a small vertical offset for each detector that must be accounted for. This is discussed in Section 5.4.

In order that the MDs be aligned properly, the measurement of the distance between the ODs and the MDs must also be known and to a greater precision than the distance between the ODs. This was achieved during 2010 by placing a high resolution beam telescope in front of the new ALFA Detectors [4]. Protons were then measured passing through the telescope, the ODs and the MDs, with the aim of measuring the various positions and skews in each of the fibers layers, which provide a major contribution to the error on the measurement of the distance from the OD to the MD. In the case of the ODs, only 20 of the overall 30 fibers of each layer were measured due

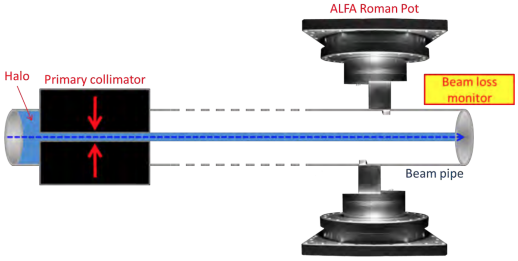

Figure 13: The first step of the alignment process. The RP is normally housed far from the beam during normal LHC operation to prevent damage to the detector [2].

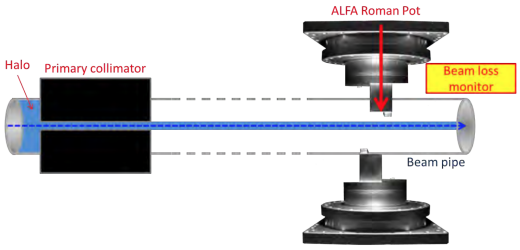

Figure 14: The second step of the alignment process. The RP is moved in small steps (5-10 μm) down towards the beam [2].

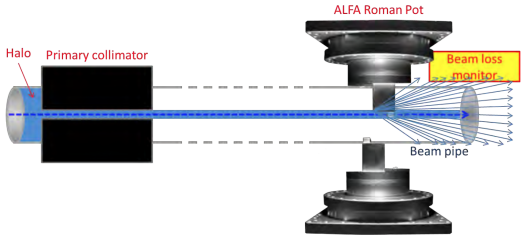

Figure 15: The third step of the alignment process. Contact of the RP with the beam is measured when a sharp increase in the trigger rates in the Beam Loss Monitor is observed as it makes contact with the hard edge of the beam halo.[2].

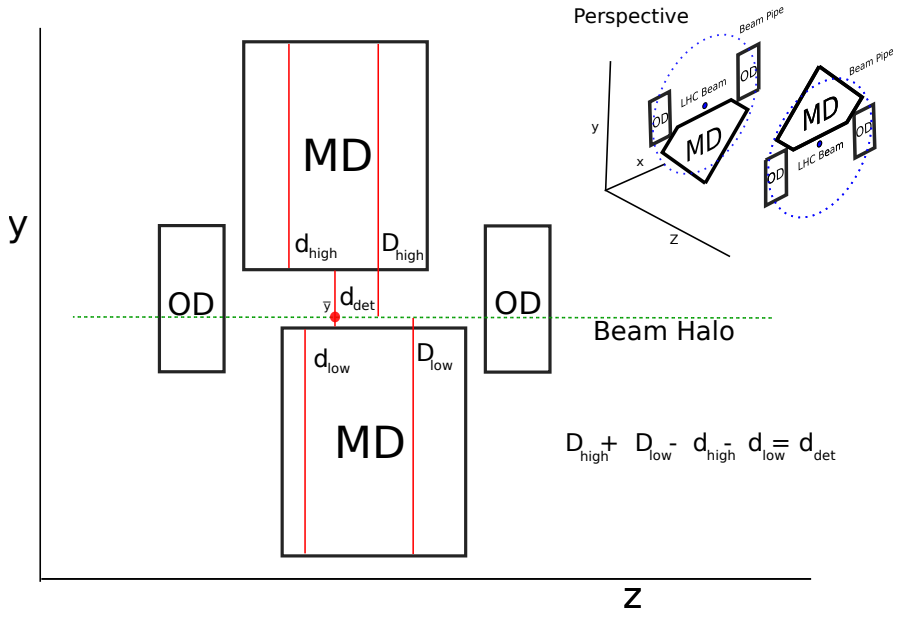

Figure 16: Diagram explaining how the distance measurement is extracted from the ODs. LHC coordinates are shown. A perspective diagram is shown for reference. This diagram was based on figures from [3]

to the aforementioned resolution problem referred to in Section 3.3.3. As such, the unmeasured fiber positions were estimated using the information obtained on the other set of fibers. The fiber position uncertainty, convoluted with other contributions from random errors associated with the experiment, was found to be well within the resolution of the MD for all the detector pairs with the exception of the old detector pair B7L1U - B7L1L, for which the variables were not measured [4].

3.3.8.3 Data Driven Procedure

It is often useful to be able to estimate the alignment without prior knowledge. The information recorded in the detector may be used to align given the theoretical expectations of the qualities that data from an aligned detector should have. These properties, and the means of alignment, are discussed henceforth.

The angular skew of the detectors can be corrected for by applying a linear fit to the hitmap of the detector in the x and y co-ordinates. A perfectly aligned detector would have no angular dependence and therefore there would be no gradient for any fitted line. As such, by small angle approximation, the slope of such a linear fit will yield the angle at which the detector has been skewed. This is shown in Figure 17.

The x component of the measurement may be corrected for by considering that the beam profile ought to be Gaussian, whereby the mean is in the centre of the detector at $x = 0$ mm. Then, by fitting such a function to a distribution of the x co-ordinates, any discrepancy may be observed in the form of a displacement of the mean of the fit away from this point. This is shown in Figure 18.

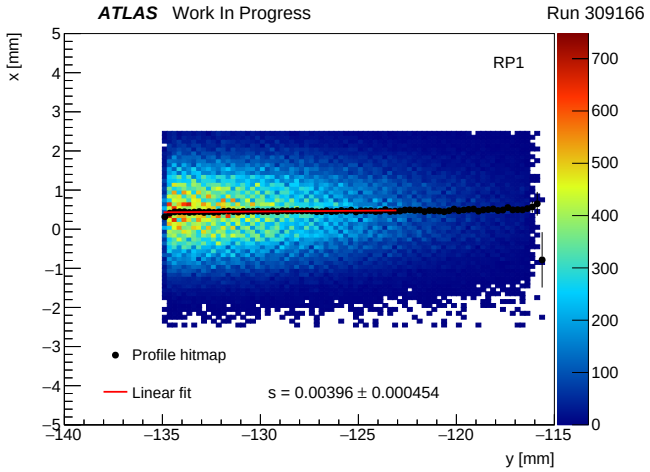

Figure 17: Hitmap used to align the skew angle of B71LU. The slope of the fit is used to estimate the angle at which the detector has been moved.

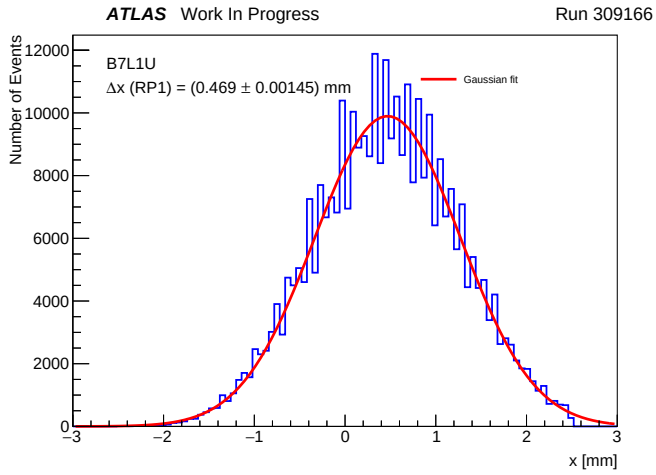

Figure 18: Distribution of the raw x values in Detector B71LU. The mean is displaced by the offset value.

The y component of the measurement may be corrected for by considering the relationship between the y components in the inner and outer detectors and the beam transport matrix. Since the protons are *back-to-back* ($y_I^A \simeq -y_I^C$) we may state that, assuming both sides have some offset in y, $\Delta y_{A/C,I/O}$:

$$y_I^A - \Delta y_I^A \simeq -y_I^C + \Delta y_I^C \tag{55a}$$

$$y_I^A \simeq -y_I^C + \Delta y_I^A + \Delta y_I^C \tag{55b}$$

As a simplification, we may argue that the total offset in y may be split evenly between the two inner detectors, such that $\frac{\Delta y_{C,I} + \Delta y_{A,I}}{2} \simeq \frac{\Delta y_I}{2}$.

By the same method as before, one may obtain the misalignment of the detectors on one side of the arm. In this instance, the inner detectors already have the contribution from Equation 55b, and so this is treated as a known variable. By the same method, one may obtain:

$$y_O^A \simeq y_I^A + \Delta y_O^A + \frac{\Delta y_I}{2} \tag{56}$$

Equations 55b and 56 inform the process used to align.

The correlation plot between the y values for inner detectors is first plotted for the raw data recorded from ALFA. A first order polynomial is fitted to the data, and the offset of this plot is

taken to be the total misalignment of the inner detectors. This is shown in Figures 19 and 20. The value is then fixed. Half of the offset is then added (subtracted) from the y values for the Inner A(C) side detectors. The outer detectors are then aligned in the same way. This is shown in Figures 21, 22, 23 and 24. The process is then repeated and iterated recursively for each of the armlets. With multiple iterations, the fit is improved.

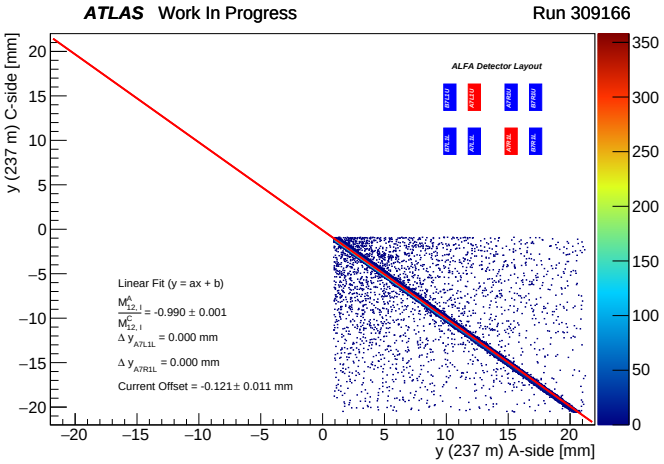

Figure 19: The first iteration of alignment of the inner detectors for Arm 1.

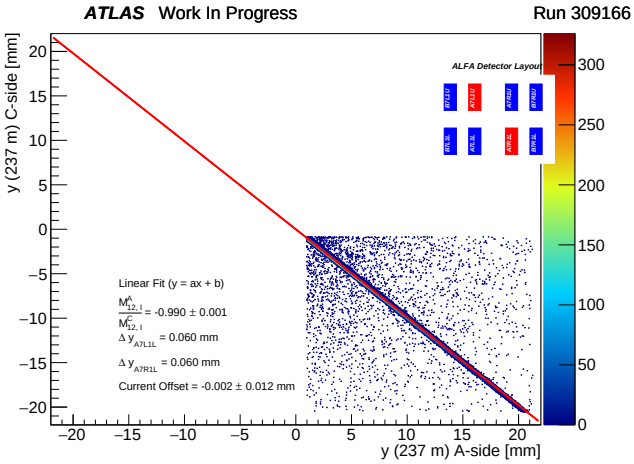

Figure 20: The final iteration of alignment of the inner detectors for Arm 1.

Notably, throughout the process, there is a simple cut applied to the data such that -2.5 mm $< x < 2.5$ mm. This is in order to isolate main bulk of data, since if no cuts are applied, diffractive events, which lose energy, have a bias to one side of the detector. This would result in a similar bias in the alignment.

The above process will yield a set of x and y offsets and a set of angular offsets. These are applied as a matrix operation to the raw co-ordinates in order to align them.

$$\begin{bmatrix} x_{Corr} \\ y_{Corr} \end{bmatrix} = \begin{bmatrix} \cos(\theta_Z) & -\sin(\theta_Z) \\ \sin(\theta_Z) & cos(\theta_Z) \end{bmatrix} \times \begin{bmatrix} x_{raw} - \Delta x \\ y_{raw} - \Delta y \end{bmatrix} \tag{57}$$

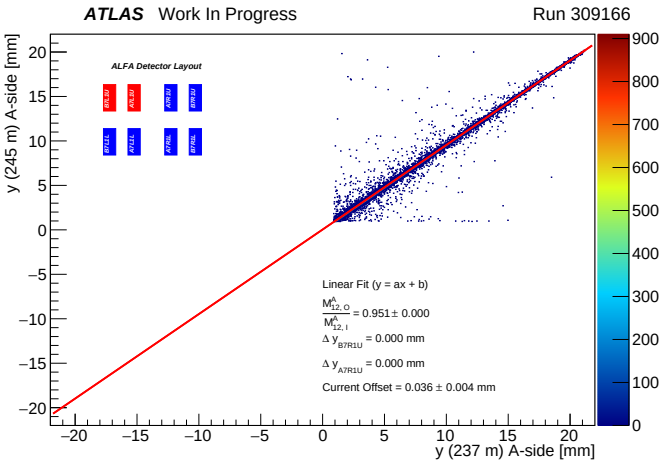

Figure 21: The first iteration of alignment of the outer detectors for Arm 1, A side.

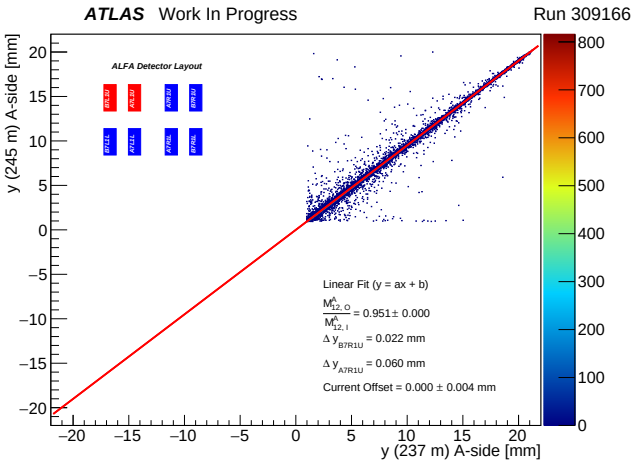

Figure 22: The final iteration of alignment of the outer detectors for Arm 1, A side.

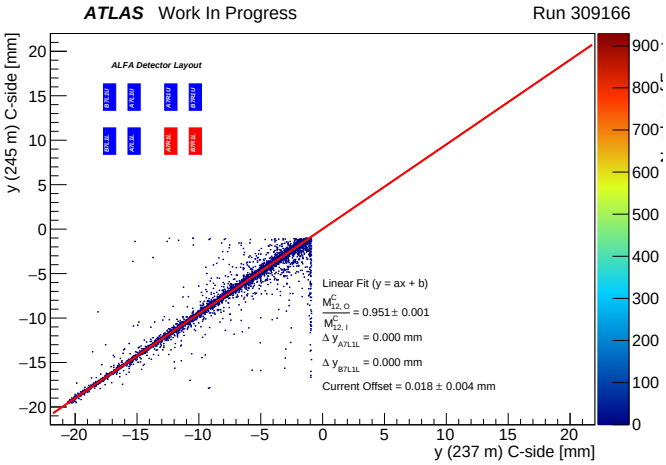

Figure 23: The first iteration of alignment of the outer detectors for Arm 1, C side.

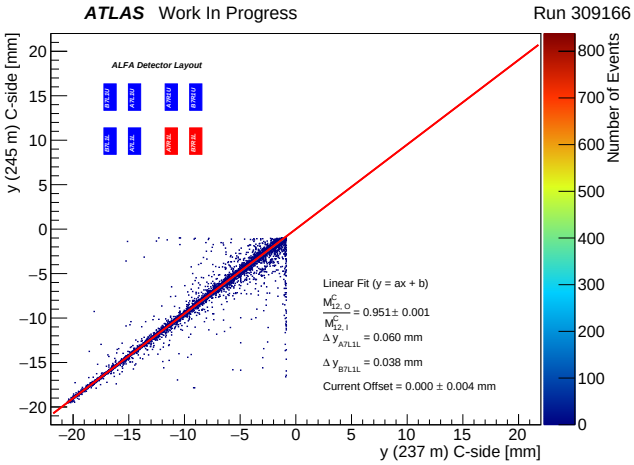

Figure 24: The final iteration of alignment of the outer detectors for Arm 1, C side.

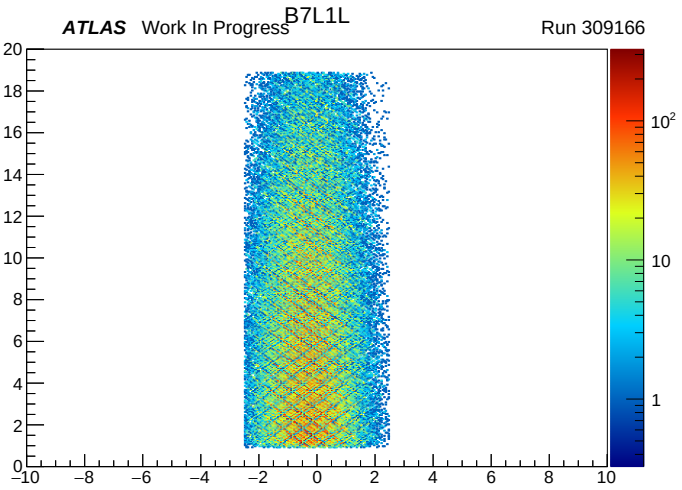

Figure 25: The hitmap of Detector A7L1U prior to alignment.

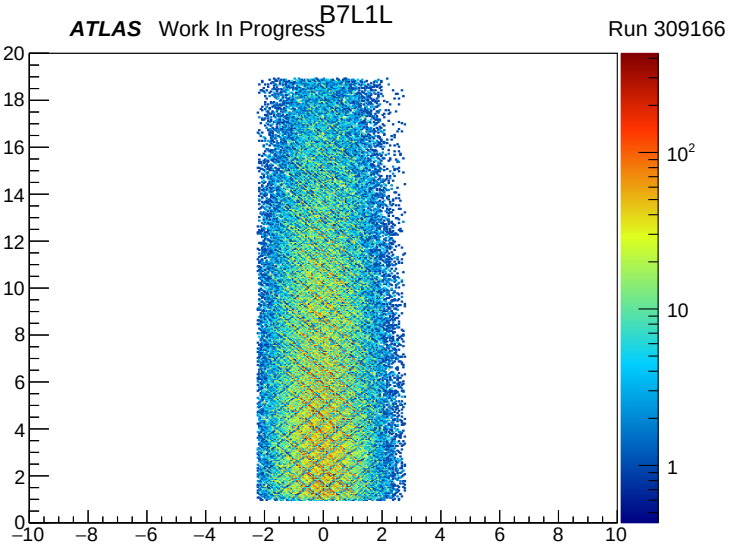

Figure 26: The hitmap of Detector A7L1U after alignment.

4 Data Acquisition

The data for this experiment was taken from *Run 309166*. This run was performed at the LHC on September 23^{rd} October 2016 as part of a larger ALFA $\beta^* = 2.5$ km campaign.

4.0.1 Collimators and Scraping

Collimators at the LHC are used for a number of reasons. The first is to prevent the magnets from heating due to wayward protons such that they do not lose their superconductivity. The point at which a magnet loses its superconducting properties is known as *quenching*. Magnet quenches are fairly common at the LHC, though the effects of unexpected quenching can prove disastrous. For example, an unexpected quench of magnets in 2008 caused significant damage to the machine when part of the cryogenic cooling system failed [24]. The rapid expansion of cryogenic gas caused a large rupture in the LHC which took many months to repair. Though this was not directly attributable to the collimators themselves, the effect is nonetheless important. Secondly, the collimators, particularly in the case of the ALFA experiment, are used to help reduce the accumulation of beam halo background around the main beam. This is of primary concern for the ALFA Detector to measure elastic protons.

The collimation process is simple. A block of material is moved towards the beam to within a distance corresponding to the order of beam widths. Collimators are composed of radiation hard carbon based and other, absorptive, metallic materials, and are lowered into the beam pipe in order to prompt multiple scattering within said material. As such, the wayward beam halo protons will scatter away from the main beam. This process is repeated by secondary and tertiary collimators placed additional beam widths from the beam. This is similar to a Matryoshka doll centered around the beam. These additional steps are in order to further collimate the consequent nuclear showers caused by the interaction of protons with the initial collimator. This process is known as *scraping*. The beam is scraped several times throughout an LHC run, as the amount of beam halo continuously grows with each cycle of the beam, which is particularly relevant in this thesis, as the proportion and type of background observed depends on the time period the event was observed in.

During the $\beta^* = 2.5$ km campaign, various collimator settings were tested, both offline and online, in order to optimise the taking of data. Specifically, the positions during scraping and non-scraping periods were examined in order to find the optimal position such that there would be little background. This was achieved by directly monitoring the a new online estimation of the track reconstruction efficiency as well as the hitmaps at the ALFA stations, in order to scrape the beam at exactly the point at which background increased to an unsatisfactory level. A number of additional collimator setups were trialled. Most notably, a horizontal collimator was moved further than normal away from the beam during data taking periods.This process reduced the levels of background to remarkably low levels compared to previous analyses. It should be noted , however, that scraping the beam has the cost of reducing both the time during the run where elastic events may be observed and also the intensity of the beam in order to remove a greater proportion of background [4].

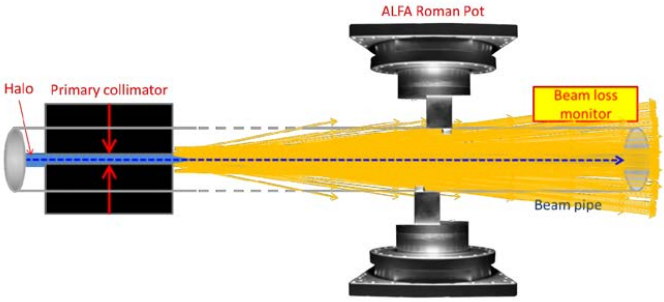

Figure 27: Diagram showing the first stage of collimation, where the collimators are moved to $2\sigma_{nominal}$. This produces a large shower which may be detected in the ATLAS Beam Loss Monitor [4].

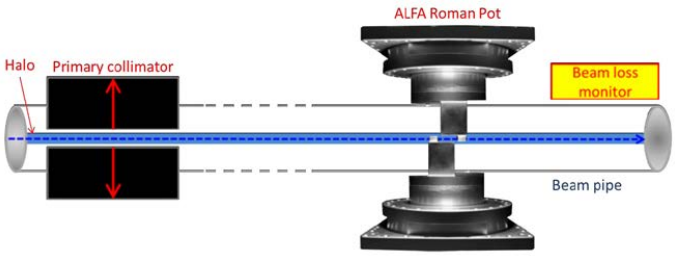

Figure 28: Diagram showing second stage of collimation, where the collimators are retracted a small amount (to $2.7\sigma_{nominal}$). The ALFA detectors are moved into position [4].

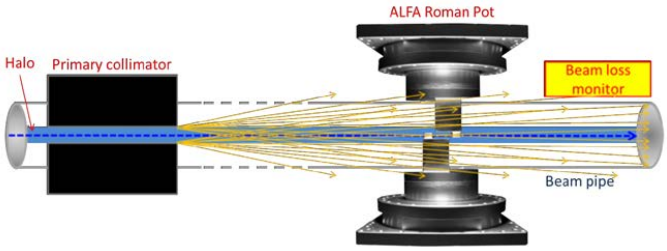

Figure 29: Diagram showing the behaviour following the initial scraping, whereby the background again increases over the course of the run until another scrape is performed [4].

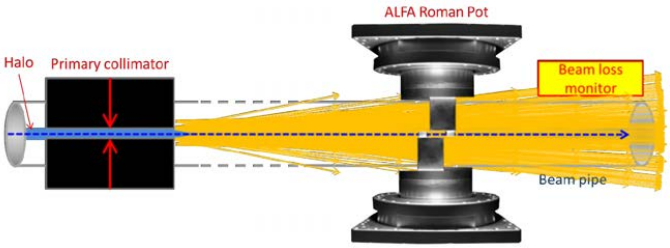

Figure 30: Diagram showing the consequent scraping.

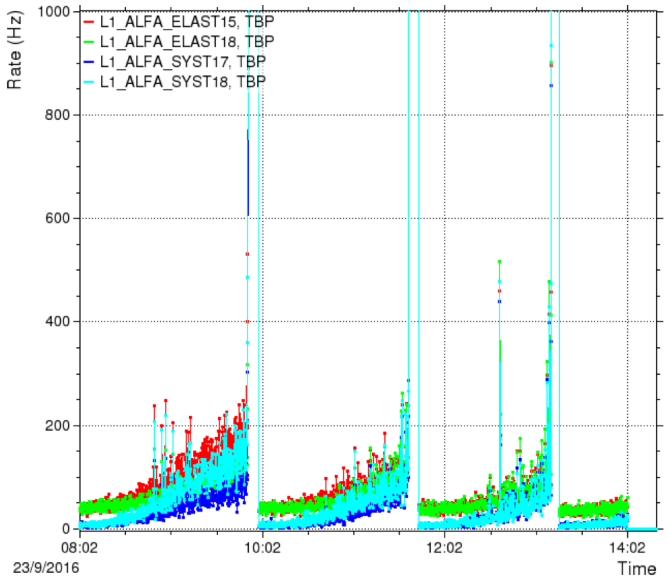

Figure 31: Raw Elastic and antigolden trigger rates as a function of time during *Run 309166*. The level of background slowly increases following scraping periods [4].

4.1 De-squeezing

The β^* used in this experiment was very significantly larger than for normal LHC conditions, since the goals of forward physics are very different to normal hadron physics. In order to match the specific requirements of a forward physics run, the beam must be *de-squeezed* from the injection optics, of the order of $\beta^* = 10m$, in order to do so. De-squeezing involves manipulating the magnet currents of the *Focus-Drift-Defocus-Drift* (FODO) cells to defocus the beam. However, this process corresponds to significant decreases in the phase advance parameter, ψ, and consequently the tune of the detector [25]. The tune of the detector describes the number of synchrotron oscillations per turn of the machine. It is very important that this parameter be controlled; for example, it is important that this value is never an integer such that the protons are not accelerated at exactly the same point as a previous turn in order that a given magnetic imperfection may not contribute periodically to the acceleration of the protons. Furthermore, as discussed in Section 3.1.1, the phase advance is important to ensure *parallel-to-point* optics.

To mitigate problems such as these, the beam is de-squeezed in small steps such that small adjustments may be made to the magnet currents to correct for these effects. Furthermore, in the case of the high β^* optics used in the experiment in this thesis, a special configuration of the magnet whereby the quadrupole magnet closest to the ALFA detector is reversed was used. It should be noted that this is generally inconvenient as two water-cooled pipes must be changed around in order to do so. This is inconvenient for forward physics runs as this requires dedicated beam time for ALFA and other forward experiments such as TOTEM.

4.2 Operation

For *Run 309166*, the operation carried out was as follows:

1. The LHC was filled. (Fill 5321)
2. The optics were de-squeezed to the required optics at $\beta^* = 2.5$ km.
3. The Roman Pots were aligned;
4. The beam was then scraped: vertical collimators were move to 2 $\sigma_{nominal}$ and the horizontal collimators to 3 $\sigma_{nominal}$;
5. When scraping completed, the collimators were moved back: the vertical collimators to 2.7 $\sigma_{nominal}$ and the horizontal collimators to 4 $\sigma_{nominal}$.
6. ATLAS Quiet Beam status was declared. No further alignment of ALFA was allowed during this period.
7. The ATLAS Inner Tracker was turned on;
8. Data taking continued until the background level was too great;
9. The ATLAS Inner Tracker was turned off;
10. The ATLAS Quiet Beam status was rescinded.
11. Steps 5-11 were repeated until the beam was either lost or scraped away.

$\sigma_{nominal}$ refers to a value which reflects the beam width corresponding to the larger emittances of a normal LHC run, where $\epsilon \simeq 3.5$ μrads $\cdot$ mm. This is for safety reasons, as an unintentional 'blow-up' of the beam could cause damage to ALFA if precautions are not taken [2]. A total of 383 lumiblocks, each corresponding to around a minute of data-taking, were taken during *Run 309166*. This corresponded to a total integrated luminosity of 56582.5 mb^{-1} according to the ATLAS Luminosity Calculator [26]. Of these, the good lumiblocks where data-taking was unimpeded were $8 < \ell < 107$ and $229 < \ell < 299$, where ℓ is lumiblock number. This corresponded to an available integrated luminosity of 28824.8 mb^{-1}. In the case of this run, the primary reason for the choice of lumiblock region was that there were errors in certain periods of the run, such as those where ATLAS Inner Detector was not ready for physics and to avoid regions where scraping took place.

5 Event Reconstruction

This section of the thesis will discuss the methods used to extract information from the elastic sample. As discussed in Section 2, the Mandelstam t value may be reconstructed entirely from the proton momentum and the initial scattering angle, the latter being measurable at ALFA using the positions of a detected proton track in multiple detectors and the transport matrix elements discussed in Section 3.1.1.

Selection criteria are applied to the data in order to ensure as pure a sample of elastic events as possible. Furthermore, a Monte Carlo (MC) simulation is generated which is used in this thesis to compare theory and experiment. The MC must include several contributing factors from the LHC beam and ALFA detector that would influence the measurement of elastic events. These include: the emittance of the beam, which influence the momentum divergence and beam width; the alignment of the ALFA RPs; the quality of the optics used to transport the protons to ALFA in simulation and to reconstruct Mandelstam t; the trigger and track reconstruction efficiencies of the ALFA detector and the proportion of background observed in the final sample of elastic events.

5.1 Event Selection

Given the behavior of an elastic event, one expects elastically scattered protons to travel in opposite directions from the IP and at a very small angle. As such, elastic protons are defined by the qualities exhibited by a *back-to-back* scattering event, where a proton is observed simultaneously with a detection in both the upper and lower stations on opposite sides of the detector. These are referred to as *detector arms*. This concept is shown in Figure 32. The detectors that compose the arms may be found in Table 3.3.1.

ALFA does not, however, observe elastic protons alone. Contributions from background such as diffractive events and beam halo, discussed at length in Section 5.9, will obfuscate the measurement of elastic protons. Furthermore, ALFA is not a perfect detector and is only so efficient at reconstructing a true proton track due to the limitations of the detector itself. Consequently, selection criteria are applied to the events in order to ensure that only well-defined elastic events with little background may be used for analysis. The techniques for such analysis are discussed henceforth.

5.1.1 Triggers

Events are first selected using the unprescaled triggers sent to Central Trigger Processing. The L1_ALFA_ELAST15 and L1_ALFA_ELAST18 triggers shown in Table 2 are used to obtain the initial dataset. These conditions require only that one of either of the trigger tiles on either side of the arm fired and is this least stringent of the elastic triggers available. This ensures that as many potential elastic candidates as possible are considered while still allowing the trigger to be used without a prescale.

5.1.2 Track Quality

In order to ensure the quality of an event in ALFA, it is required that tracks were reconstructed in all four detectors of either detector arm. This is in order to ensure that the event observed was a pure elastic event, with low potential for accidental co-incidences as a result of trigger inefficiencies.

The distribution of the number of reconstructed tracks of events in the final elastic sample is shown in Figure 33. An ideal elastic event passes through ALFA and only a single track is reconstructed in the detector. In this thesis, the co-ordinates from the most probable reconstructed track was chosen for each detector to reconstruct the positions of the proton.

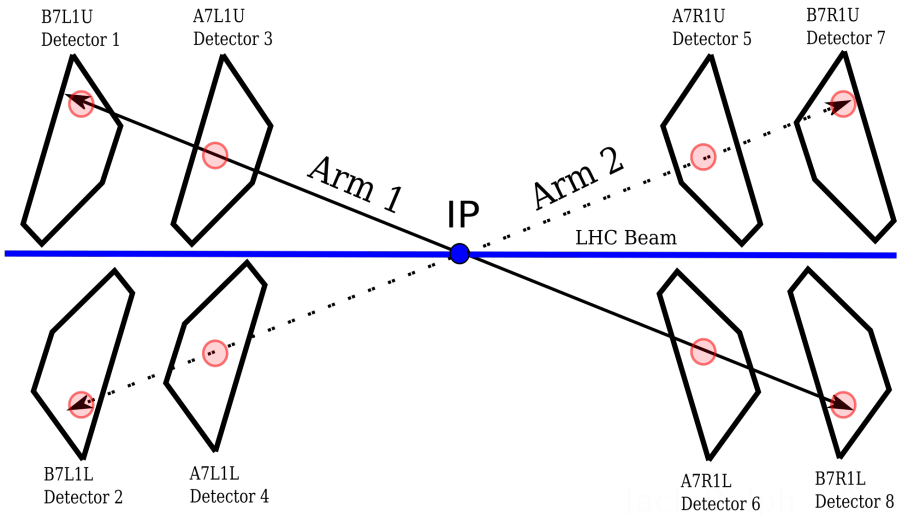

Figure 32: Example of the first aspect of the track cut, which requires that an elastic event was detected and a track reconstructed in each of the detectors that contribute to the arm. The red dots represent an event with a trigger and a reconstructed track. The solid and dashed lines represent the two elastic configurations considered, with respect to reconstructed tracks.

Specifically, background sources such as detector noise and beam halo may cause additional tracks to be reconstructed, such as in the case where two tracks are observed. A special case exists where two protons pass through ALFA and cause four proton tracks to be reconstructed. This is due to the geometry of the detector, specifically that if two particles hit the detector, two signals from the U fibers and V fiber layers respectively will be measured. However, no information is recorded about which proton produced which co-ordinate. This means all the proton co-ordinate combinations are saved and hence why a small proportion of events are observed with four tracks.

This effect contributes to 'fake tracks', which may be observed as a 45° band within the hitmap. This occurs when two protons are detected: one in the elastic scattering region and one near the edge. It may be clearly seen that these bands are strongly correlated with events where the trigger fired in the wrong bunch crossing in the detector, as shown in Figures 34 and 35. This could be caused by, for example, accidental coincidences between beam halo background which touch the edge and true elastics which are detected in the center of the detector. These events are often reconstructed in such a way that the recorded co-ordinate contains one co-ordinate from the edge event and one co-ordinate from the elastic event.

In the case of this experiment, the vast majority of events with more than one track that pass the elastic cuts were true elastics and therefore were non-negligible as part of the event count. However, a cut was placed on events with more than four reconstructed tracks, as events with too great a number of tracks are very likely to be entirely detector noise. This represents a negligible number of events compared to the total elastic sample.

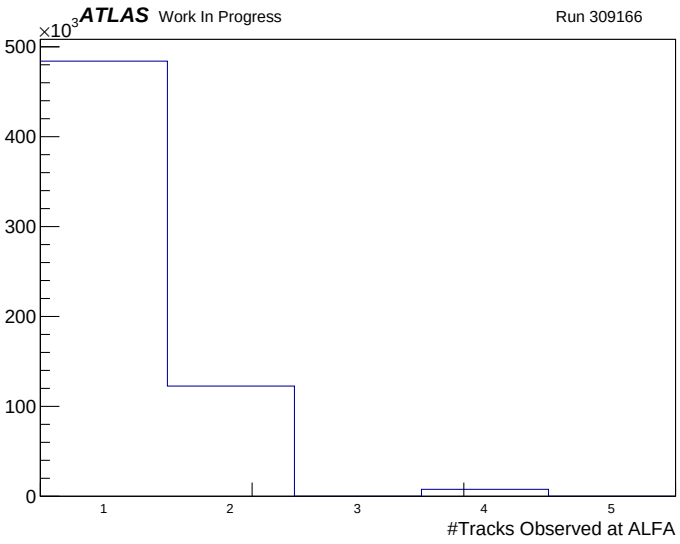

Figure 33: The number of events as a function of the number of reconstructed tracks in ALFA observed for the elastic sample after cuts.

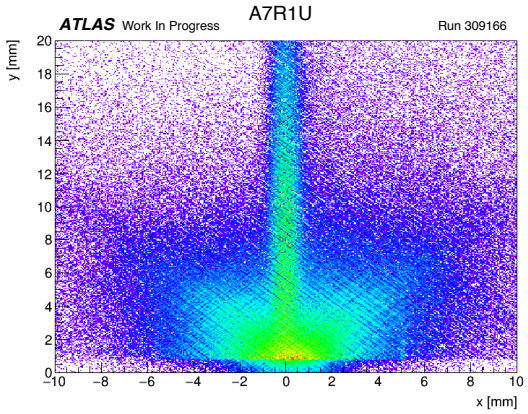

Figure 34: The full hitmap of the A7L1U detector with no elastic cuts.

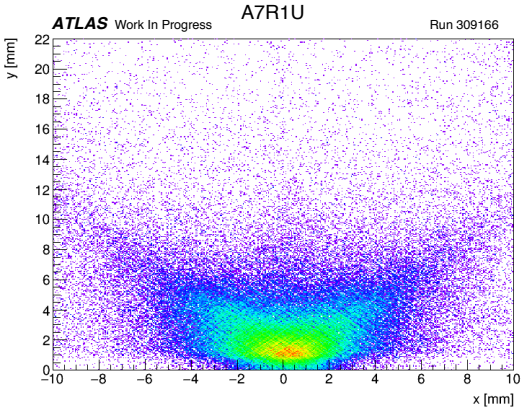

Figure 35: The hitmap of events where the trigger tiles misfired at the the A7L1U detector with no elastic cuts.

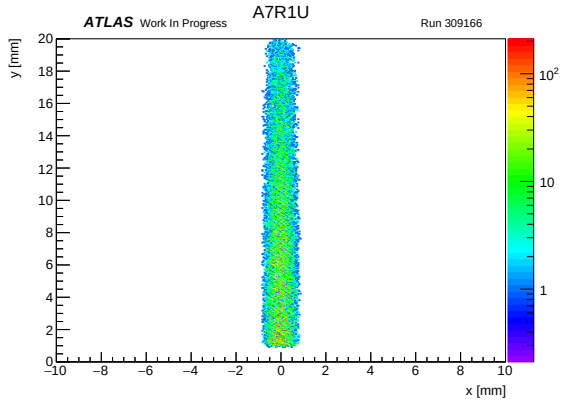

Figure 36: The hitmap of the A7L1U detector containing events with greater than 1 reconstructed track that pass the full elastic criteria.

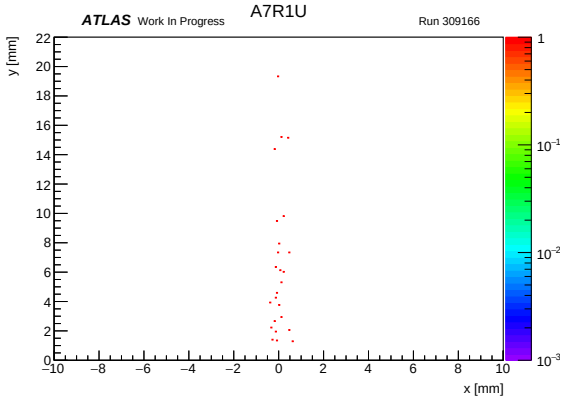

Figure 37: The hitmap of the A7L1U detector containing events with greater than 1 reconstructed track that pass the full elastic criteria with a misfired trigger.

Secondly, the quality of the track is considered. As discussed in Section 3.3.5, the ALFA detectors consist of an array of staggered scintillating fiber layers. A well defined elastic event will have a hit registered in many of these fiber layers. The minimum criteria for a track to be reconstructed

is discussed in Section 3.3.7.

There is a degree of freedom in the cut on the number of fiber layers used in reconstruction, as this varies on an experiment-by-experiment basis due to the varying background contributions, for example. As such, an attempt was made to justify whether a such a cut was necessary in this run. This was achieved by the measurements of trigger and track reconstruction efficiencies as a function of the number of overlapping fibers used.

As shown in Figure 40 and Figure 41, it is clear that the minimal number of overlapping fiber hits experience significantly larger detector inefficiencies than those with more fiber layers used in reconstruction. However, the actual number of these types of events are very small relative to the overall event count. As such, no cut was applied in order to maximize the total possible number of elastics in the sample.

A point to note is that the distribution of the number of fiber layers used in the reconstruction of the U co-ordinate appears greater than that of the V co-ordinate. This could be explained by low fiber efficiency that was observed in the V fibers for Detectors A7L1U and A7L1L, as shown in Figures 97 and 98.

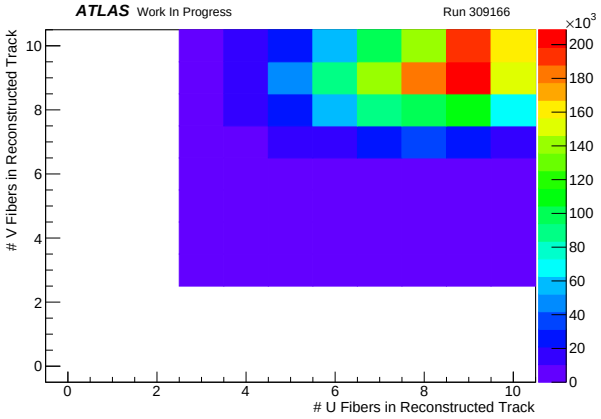

Figure 38: A plot of the distribution of the number of fibers used in track reconstruction in U and V.

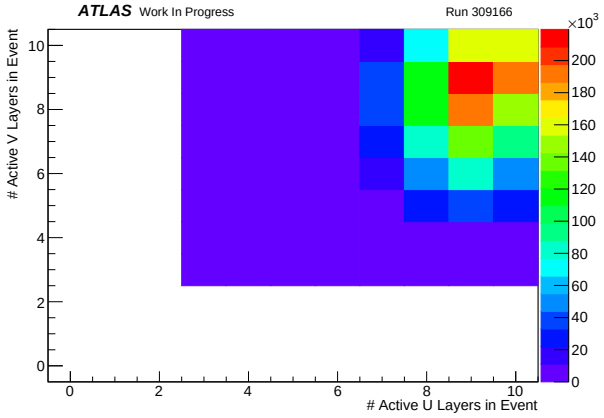

Figure 39: A plot of the distribution of U-V plates with between 0 and 3 fiber hits.

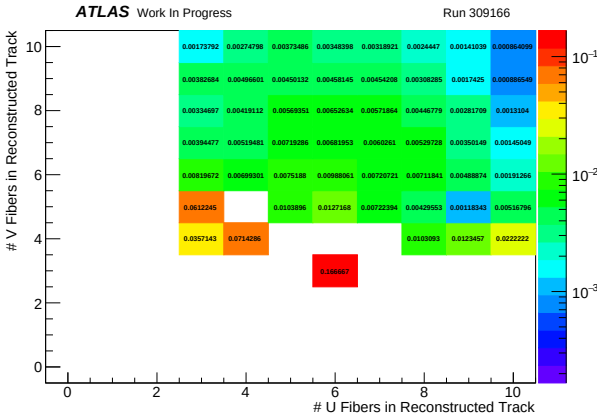

Figure 40: A plot of the trigger inefficiency, the ratio of events that passed the elastic cuts with a trigger recorded in the wrong bunch crossing or not at all as a function of the number of overlapping fiber layers used in reconstruction of U and V.

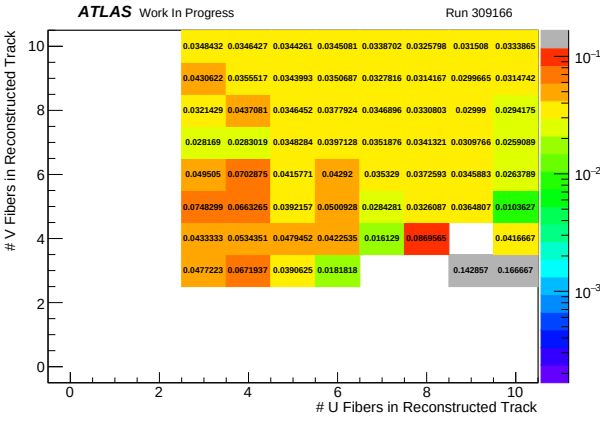

Figure 41: A plot of the proportion of events with an elastic track that was reconstructed in only three of the detectors of an arm to the total number of reconstructed elastic tracks (simplified track reconstruction inefficiency) as a function of the number of overlapping fiber layers used in reconstruction of U and V.

5.1.3 Geometrical Cuts

Various geometric cuts are also imposed upon the data in order to prevent detector effects from interfering with the measurement of elastic protons.

5.1.3.1 Edge Cut

There is a region where trigger tiles and detectors do not fully overlap at the very bottom of the detector, which means that the trigger efficiency of the detector will become non-negligible, as seen in Figure 96. Therefore, protons must be detected within the confines of 90 μm from the bottom of the MD or they are rejected in order to ensure that the trigger and track reconstruction efficiencies are uniform across the whole detector. Notably, the edge cut was reduced to 60 μm for the main fit to data performed in Section 7.2 for both the elastic sample and for the background, as the distribution in the former case poorly described low Mandelstam t values otherwise. This was possible due to remarkably low background levels, discussed in Section 5.9.

5.1.3.2 Beamscreen Cut

At the top of the detector, The LHC Beamscreen is used to shield the collider's superconducting magnets from synchrotron radiation produced by the circulating protons. As the ALFA detectors must move in the order of millimeters from the LHC beam, it is possible for it to detect protons that have interacted with this structure. Hence, the limits on the region from which such protons may be measured are removed in the elastic cuts.

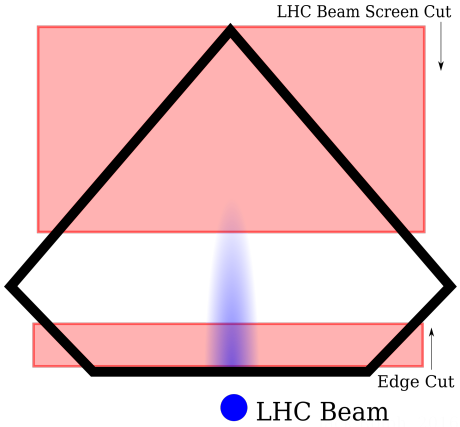

Figure 42: A visual depiction of the effects of the edge and beamscreen cuts. The red regions are removed in the elastic selection process.

5.1.4 Back-to-back Cuts

Finally, protons are expected to scatter *back-to-back*. As such, four co-ordinate cuts are applied in the detector to ensure that events exhibit this characteristic. Except in the case of the cuts on y, the values for these regions are determined through the use of Monte Carlo, discussed in Section 5.6.

With respect to the co-ordinates, the event is required to satisfy that they reside within:

- 3σ of an ellipse fitted to Monte Carlo in the x co-ordinate at the inner station at 237 m and θ_x, the local angle (see Equation 74 in Section 5.8.3), for both the A and C side;
- 3σ of an ellipse fitted to Monte Carlo in the x co-ordinate on the innermost detector on the A side and the x co-ordinate on the innermost detector on the C side (237 m from IP in both cases);

- 3σ of an ellipse fitted to Monte Carlo in the x co-ordinate on the outermost detector on the A side and the x co-ordinate on the outermost detector on the C side (245 m from IP in both cases)
- ± 3 mm of a straight line fit of the y co-ordinate of the C side and the y co-ordinate on the A side, for both the inner and outer detector.

Specifically, the regions chosen were done so in order to best capture the behavior elastic events in the co-ordinate systems chosen due to the fact that elastic protons on either side of the detector should share the same scattering angle, within the confines of the divergence, resolution and other systematic effects.

The parameters for the elliptical cuts are produced as fits to the Monte Carlo simulation of the parameter spaces, which are discussed in Section 5.6. The results of the cuts are shown in Figures 43, 44, 45 and 46.

The overall elastic cut flow for *Run 309166* is shown in Table 3.

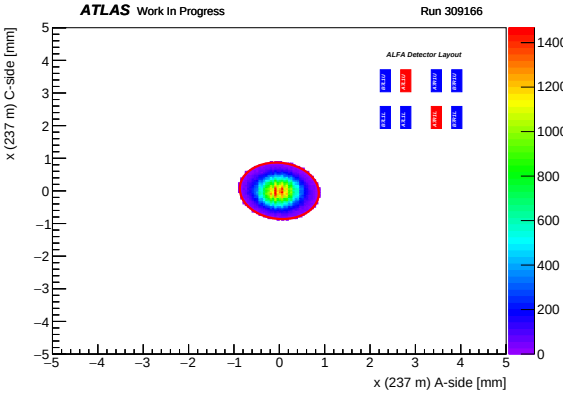

Figure 43: $x_I^A - x_I^C$ cut in data using MC parameters, the limits of which are indicated by the red line.

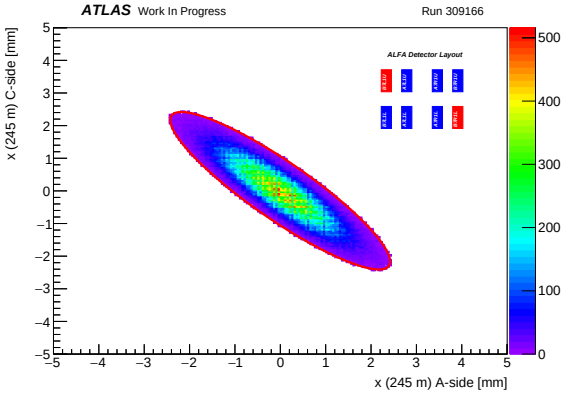

Figure 44: $x_O^A - x_O^C$ cut in data using MC parameters, the limits of which are indicated by the red line.

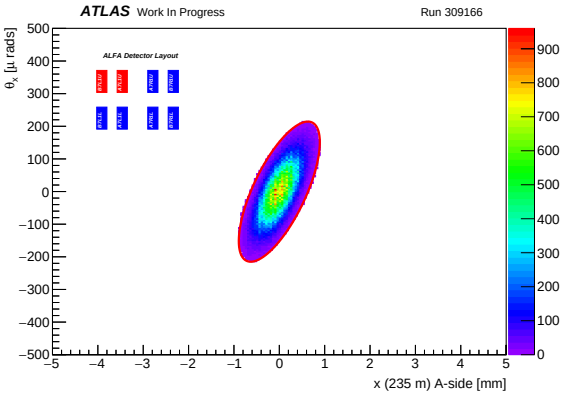

Figure 45: $x_I^A - \theta_{x,O}^A$ cut in data using MC parameters, the limits of which are indicated by the red line.

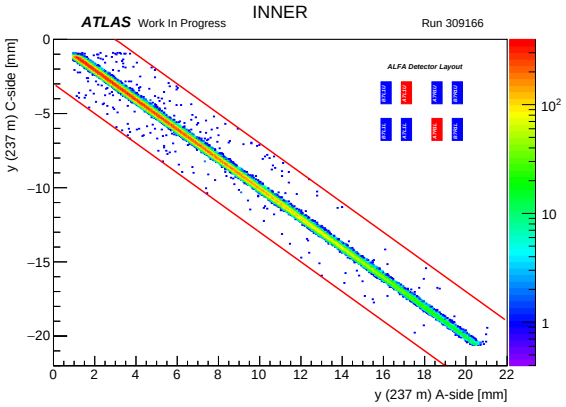

Figure 46: $y_I^A - y_I^C$ cut in data using MC parameters, the limits of which are indicated by the red line.

Cut Applied	All	Arm 1	Arm 2
Triggers & 4 Reconstructed Tracks	624897 ± 0.127%	314078 ± 0.178%	310819 ± 0.179%
+ Track Quality Cut	615650 ± 0.127%	310790 ± 0.179%	304860 ± 0.181%
+ Edge Cut	608509 ± 0.128%	307584 ± 0.18%	300925 ± 0.182%
+ Beamscreen Cut	603193 ± 0.129%	305373 ± 0.181%	297820 ± 0.183%
Back to Back Cuts			
+ $x - \theta_x$ Correlation, A Side	589805 ± 0.13%	298682 ± 0.183%	291123 ± 0.185%
+ $x - \theta_x$ Correlation, C Side	581694 ± 0.131%	294567 ± 0.184%	287127 ± 0.187%
+ x A-C Correlation (245 m)	578729 ± 0.131%	293018 ± 0.185%	285711 ± 0.187%
+ x A-C Correlation (237 m)	578474 ± 0.131%	292877 ± 0.185%	285597 ± 0.187%
+ y A-C Correlation (237 m)	577395 ± 0.132%	292296 ± 0.185%	285099 ± 0.187%
+ y A-C Correlation (245 m)	577304 ± 0.132%	292237 ± 0.185%	285067 ± 0.187%

Table 3: Cut flow for elastics over *Run 309166*.

5.2 Emittances

As mentioned in Section 3.1.1, the emittance describes the size in position-momentum space that the beam occupies and contributes to the minimum Mandelstam t observable in the detector. In order to ensure that as many elastic protons strike ALFA as possible, it is necessary that the emittance is as low as achievably possible in order to minimize the incident angle of the protons. The emittances used in this thesis were:

$$\epsilon_{x,B1} = 2.10 \pm 0.420 \ \mu\text{rads} \cdot \text{mm} \tag{58a}$$

$$\epsilon_{x,B2} = 2.16 \pm 0.432 \ \mu\text{rads} \cdot \text{mm} \tag{58b}$$

$$\epsilon_{y,B1} = 1.04 \pm 0.208 \ \mu\text{rads} \cdot \text{mm} \tag{58c}$$

$$\epsilon_{y,B2} = 0.85 \pm 0.170 \ \mu\text{rads} \cdot \text{mm} \tag{58d}$$

These values were extracted from the ATLAS eLog [22]. Screenshots of the values used are available in Section 9.1. To validate these values, the beamspot size for *Run 309166* in x and y were examined and are shown in Figures 47 and 48.

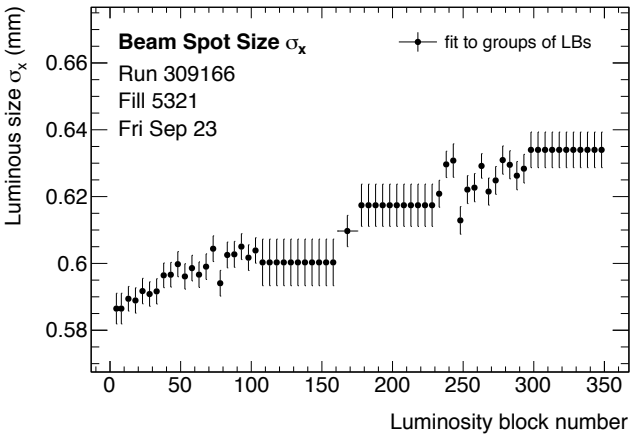

Figure 47: The beamspot size in millimeters for the x co-ordinate of the beam [5].

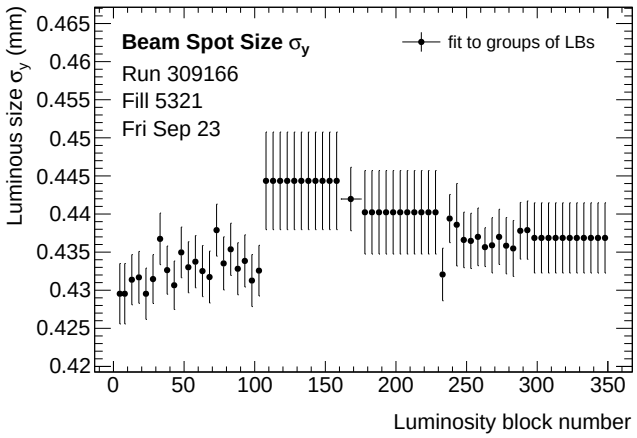

Figure 48: The beamspot size in millimeters for the y co-ordinate of the beam [5].

The equation used to describe the size of the beamspot is given as follows:

$$\sigma_{BS} = \sqrt{\frac{\frac{\beta^*}{\gamma}}{\frac{1}{\epsilon_{B1}} + \frac{1}{\epsilon_{B2}}}} \tag{59}$$

where $\gamma = \frac{E_{beam}}{m_p}$, the Lorentz factor for beam protons.

The values estimated from the graphs suggests a beamspot size of around 0.615 mm for σ_x and 0.44 mm for σ_y on average throughout the course of the run. This corresponds to average emittances of 2.09 μrads $\cdot$ mm and 1.07 μrads $\cdot$ mm respectively. It is a point to note that, while the values for σ_x and σ_y correspond well to the emittances recorded, the value of σ_x appears to have grown in magnitude significantly over the course of the run relative to σ_y. This means that the estimate made for the emittance in this case will be significantly greater. For this reason, the stated values of emittance, which have been consistent with a 10% error in previous analyses [4], have been increased to a 20% to account for this variation in size.

Another consistency check and an important contributing factor to the MC simulation is the beam divergence, or the angular uncertainty of the proton. This may be calculated by considering the three-dimensional transport matrix, which has an additional divergence term D, appended to the value for the scattering angle. As a dispersion term is added to the scattering angle from the interaction point of the beam, one may readily obtain a distribution of the divergence. The convoluted divergence, or the divergence caused by the emittances of the two beams, may be calculated using:

$$(\theta_y^{*A} + D_y^A) + (\theta_y^{*C} + D_y^C) = D_y^A + D_y^C \tag{60}$$

where $\theta^{*A/C}$ refers to the scattering angle reconstructed on the A(C) side of the detector using the local subtraction method, discussed in Section 5.8.2. This expression therefore evaluates to the convoluted sum of the two divergences.

In theory, the convoluted beam divergence is related to the emittance through the relation:

$$D_{conv} = \sqrt{\frac{\epsilon_y^{B1} + \epsilon_y^{B2}}{\gamma\beta^*}} \tag{61}$$

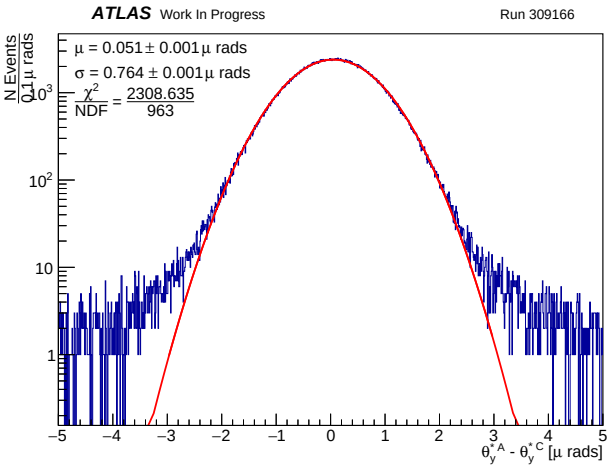

Figure 49: The distribution of the difference in reconstructed θ_y^* in data.

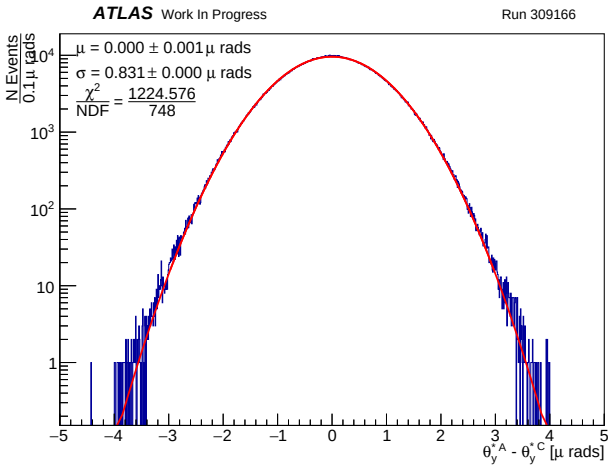

Figure 50: The distribution of the difference in reconstructed θ_y^* produced by Monte Carlo simulation.

It should be noted that, in spite of the agreement with the emittance values with the beamspot, that there is a clear difference between the true divergence and the predicted MC divergence shown in Figures 49 and 50 respectively. The reasons for this are unclear, though it is likely a consequence of either the tails of the distribution in data or overstated resolution.

The evolution divergence was also measured as a function of lumiblock in Figures 51 and 52. This would indicate any time-dependency in the divergence of the beam. However, there is no behavior of note that may be observed in these distribution.

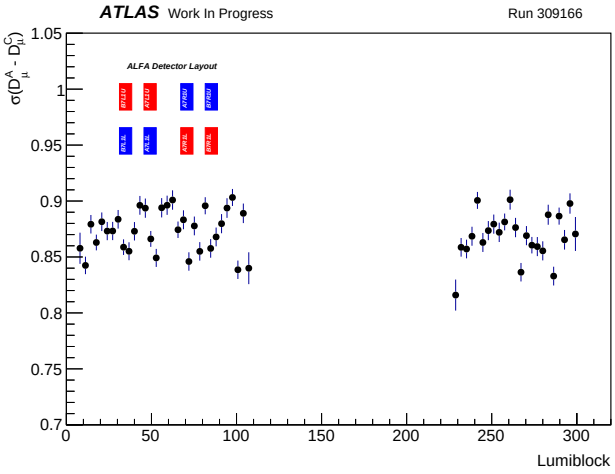

Figure 51: The distribution of the convoluted divergence in data as a function of lumiblock for Arm 1.

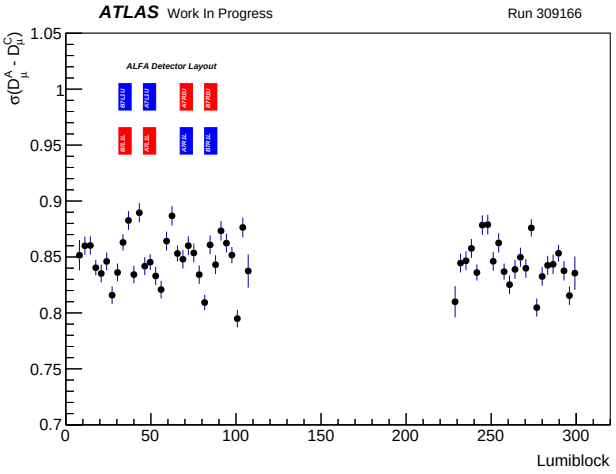

Figure 52: The distribution of the convoluted divergence in data as a function of lumiblock for Arm 2.

5.3 Resolution

The ALFA detectors have a limited resolution. This refers to the fact that the detector is unable to measure where protons were detected exactly. A theoretical estimation of the resolution of one of the fiber may be given by the RMS value of the dimensions of the pixel:

$$x_{RMS} = \sqrt{\frac{\int_{\frac{-d}{2}}^{\frac{d}{2}} (x - x_0)^2}{d}} = \frac{d}{\sqrt{12}} \tag{62a}$$

where d refers to the fiber diameter.

The stacking of the layers has the effect on the resolution such that the pixel size reduces by a factor of ten, since staggering the detector layers significantly increases the probability of a detection by at least one of the fibers. If one of the fiber diameters is 500 μm and the probability of detection increases by a factor of ten as a result of the ten fiber layers, the above yields a theoretical maximum resolution of 14.4 μm. This assumes perfect staggering and fiber efficiency and in reality the resolution is closer to 30 μm [2].

It is possible to measure the resolution of the detector using the data collected at ALFA. Measurement of the resolution may be achieved by performing a theoretical estimation of where a proton will be transported to given a measurement from the inner detectors and comparing this to the value observed in the outer detectors. This is simplest to achieve for the y co-ordinates, where the contribution from the transport matrix with respect to the initial vertex is very small and may thus be neglected:

$$y_I \simeq M^{A/C}_{I,12} \cdot (\theta^*_y + D^{A/C}_y), \qquad y_O \simeq M^{A/C}_{O,12} \cdot (\theta^*_y + D^{A/C}_y) \tag{63a}$$

$$\frac{y_I}{y_O} = \frac{M^{A/C}_{I,12}}{M^{A/C}_{O,12}} \tag{63b}$$

$$\therefore y^{ex}_O \simeq \frac{M^{A/C}_{I,12}}{M^{A/C}_{O,12}} \times y_I \tag{63c}$$

It is expected that the measurement of the difference between the extrapolated and true y values

for the outer detector will be distributed as a Gaussian and that the width of the distribution would represent the error on the measurement of the value of y observed in the outer detectors. This uncertainty is the resolution of the detector in both y and x. We may justify this by observing that the measured co-ordinates are reconstructed from signals in the scintillators, which are rotated to 45° from LHC co-ordinates. Since these co-ordinates are reconstructed from the same point in the detector, one may argue that the results obtained are applicable for the resolution in x as well.

The aforementioned resolution distribution in data and MC is shown in Figures 53 and 54 respectively. While a Gaussian fit describes the majority of the data well, non-Gaussian behavior is observed at large differences in the predicted and observed angle. This is expected, as events with this property are less likely to represent an elastic event. The effect also introduces a bias to the fit result. Furthermore, particles with a large disparity between the predicted and measured y co-ordinate are much more likely to represent background particles, which would have a uniform random distribution between the two, which may also explain the non-Gaussian tails.

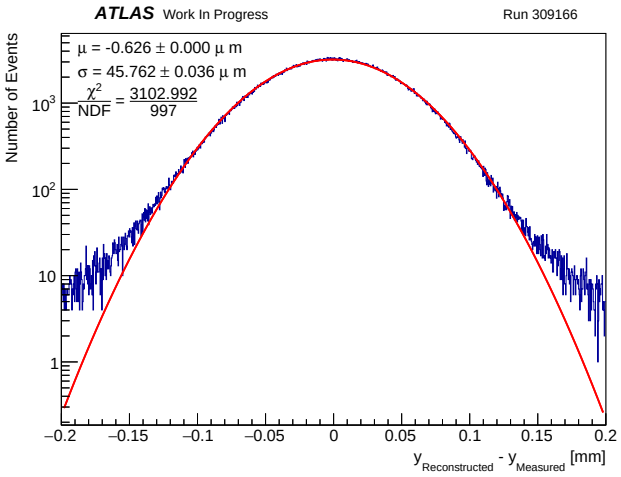

Figure 53: The distribution of the convoluted resolution in data.

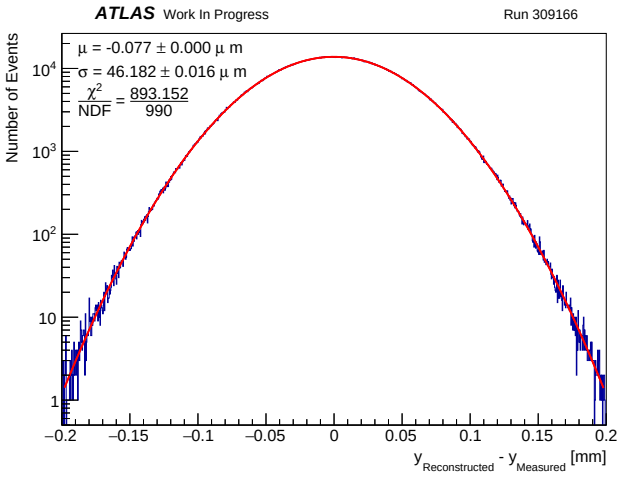

Figure 54: The distribution of the convoluted resolution produced by Monte Carlo simulation.

The measurement includes the resolution of both detectors, since co-ordinates from both inner and outer detectors are used. One may readily see that this convoluted resolution matches with the predicted values. Using the fact that the outer detectors have approximately a further 10% contribution to the uncertainty due to already having passed through one detector [2] and the measured convoluted resolution, $\sigma_{res,M} = 45.762$ μm, one may measure the inner resolution, $\sigma_{res,I}$:

$$\sigma_{res,M} = \sqrt{\sigma^2_{res,I} + \sigma^2_{res,O}} \simeq \sqrt{\sigma^2_{res,I} + 1.1\sigma^2_{res,I}} \tag{64a}$$

$$\therefore \sigma_{res,I} = \frac{\sigma_{res,M}}{\sqrt{2.1}} = 31.5 \ \mu\text{m} \tag{64b}$$

The resolution was observed to increase linearly with the y co-ordinate of the observed proton. This is shown in Figure 55. This effect was more pronounced for the C side than the A side. The reduction in the resolution with distance in y is currently understood to arise from the fact that the fibers further away from the fiber support experience greater fluctuations from the detector design parameters.

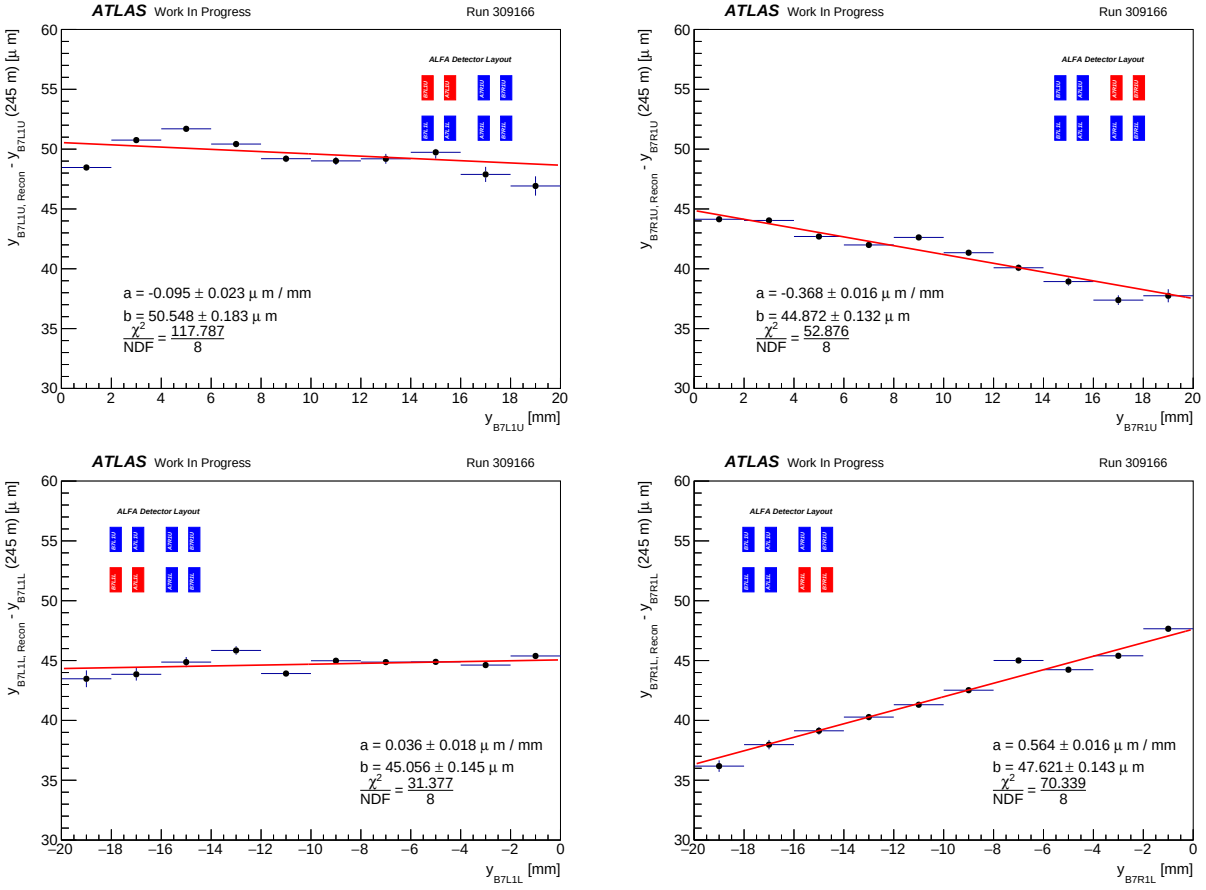

Figure 55: The resolution as a function of y in data.

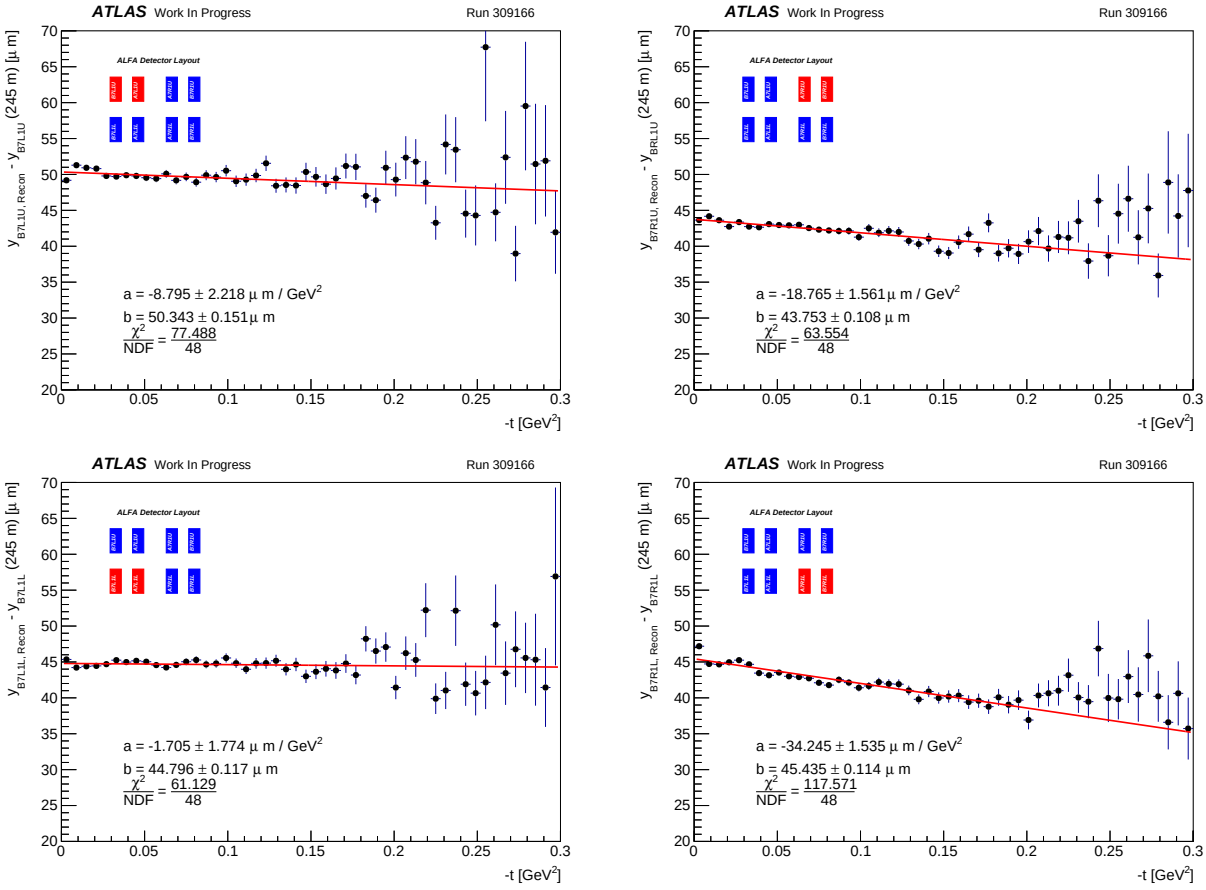

Figure 56: The resolution as a function of Mandelstam t in data.

5.4 Vertical Offset and Distance

The distance between the detector stations are calculated using the methods outlined in Section 3.3.8.

A vertical offset of each detector is also calculated and describes the position of the pots with respect to the beam. This is achieved from the point of view that the protons have azimuthal symmetry with respect to where they are detected. The same number of events are expected to be observed in the lower detector as the upper detector. The technique used to analyze this is known as a *sliding window technique*. This involves taking a set of five-thousand windows, half from the upper detector with the widths and positions taken at random, while the other half are lower detector windows expanded such that the same number of events are observed in both. The y co-ordinates are then entered into a histogram, the mean of which is taken to be the offset. The error is calculated from the difference between this method and a technique known as a Kolmogorov-Smirnov test, whereby the two distributions between the top and bottom detector may be compared [4].

This process produces both the fitted values of the distance and offset, as well as a covariance matrix for the errors between the vertical offsets and distances. The significance of the covariance matrix in this thesis is discussed in Section 6.2.1 and is shown in Table 4.

	D_{S1}	D_{S2}	V_{S3}	D_{S4}	V_{S1}	V_{S2}	V_{S3}	V_{S4}
D_{S1}	1.018e-03	1.068e-03	1.069e-03	1.019e-03	-3.198e-07	-2.833e-07	5.136e-07	5.198e-07
D_{S2}	1.068e-03	1.123e-03	1.122e-03	1.069e-03	1.222e-06	1.506e-06	-1.218e-06	-1.059e-06
D_{S3}	1.069e-03	1.122e-03	1.124e-03	1.070e-03	-1.117e-06	-9.976e-07	1.243e-06	1.273e-06
D_{S4}	1.019e-03	1.069e-03	1.070e-03	1.021e-03	-1.766e-06	-1.757e-06	1.979e-06	2.153e-06
V_{S1}	-3.198e-07	1.222e-06	-1.117e-06	-1.766e-06	2.375e-03	2.494e-03	-2.496e-03	-2.377e-03
V_{S1}	-2.833e-07	1.506e-06	-9.976e-07	-1.757e-06	2.494e-03	2.620e-03	-2.621e-03	-2.497e-03
V_{S1}	5.136e-07	-1.218e-06	1.243e-06	1.979e-06	-2.496e-03	-2.621e-03	2.623e-03	2.498e-03
V_{S1}	5.198e-07	-1.059e-06	1.273e-06	2.153e-06	-2.377e-03	-2.497e-03	2.498e-03	2.380e-03

Table 4: Covariance matrix from the vertical component and distance component fitting process. Units are provided in squared millimeters.

5.5 Effective Optics

The optics used for the experiment, specifically the matrix element components that dictate the transport of elastic protons from the IP to ALFA, is achieved by adjusting the magnet currents in Monte Carlo. This is achieved by identification of constraints to which the transport matrix elements must abide. For example, parallel-to-point optics for the y component of the LHC beam means that the position in y for protons in ALFA are only dependent upon the scattering angle and its associated matrix element (i.e $y \simeq M_{12}\theta_y$). This fact allows measurement of M_{12}^I/M_{12}^O. This is not so for the x component, which has a significant contribution from the vertex element. However, the ratio of positions in x on either side of the detector, which under ideal circumstances ought to be symmetric due to the nature of elastic events, provides insight into the ratio of another matrix element ratio $M_{11}^A/M_{11}^{C,I}$. In this way, a set of constraints on the matrix elements may be obtained, and similar assessments are able to find the ratios of the other matrix elements [27][4].

At the time of writing, this process has not been carried out for the campaign in this thesis and therefore cannot be examined in depth. The matrix elements used have been estimated for the $\beta^* =$ 2.5km campaign. In order to gauge the importance of the optics to the measurement in the interim, a simple technique has been applied whereby the average differences between two Mandelstam t reconstruction methods, the local subtraction method (see Section 5.8.2) and subtraction method (see Section 5.8.1) are compared as shown in Figure 57. The slope represents the ratio $M_{12,x}/M_{22,x}$. As can be seen, the slope is small and therefore any deviation between design and effective optics with respect to this ratio is also small.

It is henceforth assumed that the design optics used are close to the effective optics for this ratio

and in general. This is, however, unlikely to be entirely the case. Therefore, no statement is made in this thesis as to the validity of the optics used.

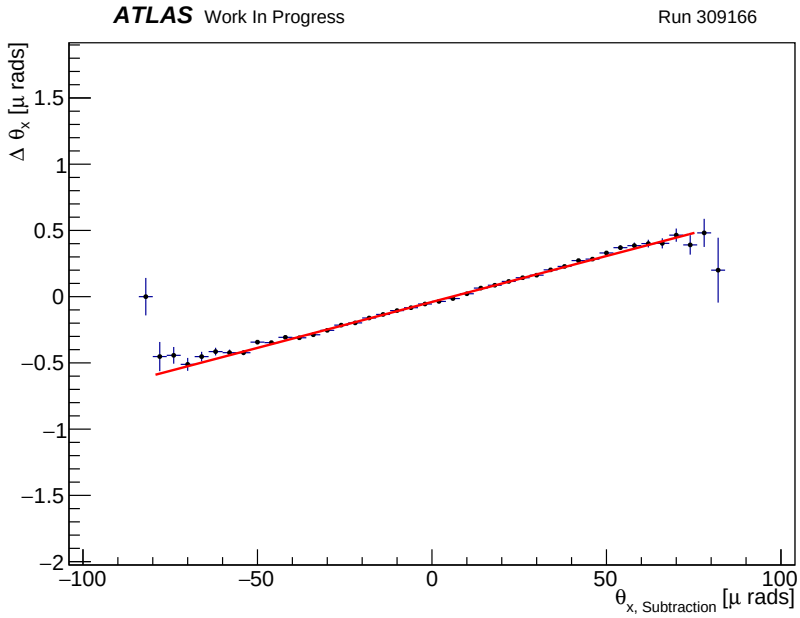

Figure 57: The average difference between the local angle and subtraction methods of angle reconstruction with respect to the subtraction method result. The errors shown are the RMS of the average shown. A 1D polynomial has been plotted to the diagram as an indication of the slope of the relationship.

5.6 Simulation

Using the theoretical distribution outlined in Equation 40c, one can generate a Monte Carlo (MC) simulation of the Mandelstam t spectrum of elastically scattered protons.

A number of points must be taken into consideration. The first point to note is that, while the proton is generated according to the aforementioned t distribution, it is not scattered at exactly the same position or initial divergence angle within the beam. As such, the distribution requires that the proton be generated with an initial vertex and divergence angle from a Gaussian distribution characterized by the emittances.

Secondly, the azimuthal angle at which the proton scatters will be random, as the proton is not boosted in this frame. Using the definition for the Mandelstam t spectrum in Equation 30c, we may see that it may be rewritten in terms of the scattering angle to be:

$$-t = p^2(\theta_x^2 + \theta_y^2) \tag{65}$$

Using that $\theta_C = \theta_C\sqrt{\cos^2\phi + \sin^2\phi}$, we see that:

$$\theta^*_{x_{Max}} = \frac{\sqrt{-t}}{p}\cos\phi + D_x \tag{66a}$$

$$\theta^*_{y_{Max}} = \frac{\sqrt{-t}}{p}\sin\phi + D_y \tag{66b}$$

where ϕ refers to the azimuthal scattering angle from the beam, and D the divergence of the

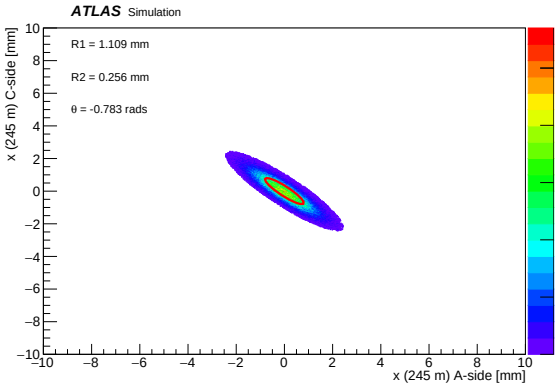

Figure 58: Elastic MC fit result for $x_O^A - x_O^C$ correlation (2×10^7 events).

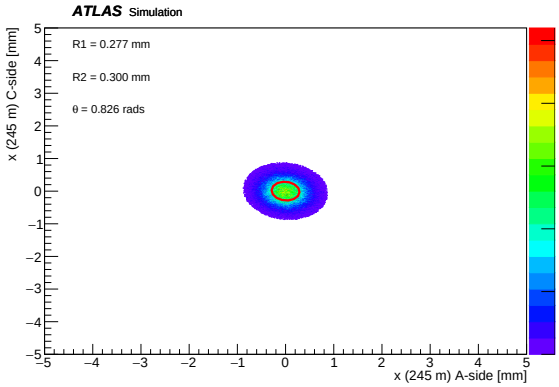

Figure 59: Elastic MC fit result for $x_I^A - x_I^C$ correlation (2×10^7 events).

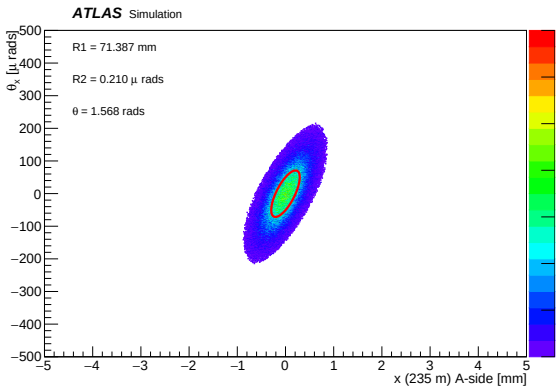

Figure 60: Elastic MC fit result for $x - x_\theta$ correlation (2×10^7 events).

beam, which is given by:

$$D = \sqrt{\frac{\epsilon}{\beta^* \gamma}} \tag{67}$$

where β^* and γ have their usual meanings.

Lastly, the protons must be carried to the ALFA detectors via the transport matrix. All the geometrical and *'back-to-back'* cuts normally used for elastic events are included in the simulation. Any further geometrical cuts performed upon data may be applied to the Monte Carlo, thus allowing the production of a MC that is very similar to that which is observed in data.

Particularly of note is that the edge cut for the elastics is made in the detector co-ordinate system and not the LHC system. This is of particular consequence as the events of interest are observed close to the beam and slight inconsistencies in this region will cause potentially significant repercussions in the measurement of the cross-section, since this region contains most of the low Mandelstam t events in the elastic sample. Consequently, the inverse transformation of the edge in detector co-ordinates to the LHC co-ordinates produced by the MC is achieved using the alignment matrix used for the main elastic sample. Furthermore, any adjustments to vertical offsets and distances are performed in the detector co-ordinate system, which is relevant in the fitting of nuisance parameters discussed in Section 6.2. This is done in order that the edge cut is consistent between the two datasets.

The fits and fit results from MC are shown in Figures 58, 59 and 60.

As may be seen in Figure 61, the acceptance rate of ALFA varies between arms. This is primarily due to the differing alignments, optics and edge conditions for each of the detectors.

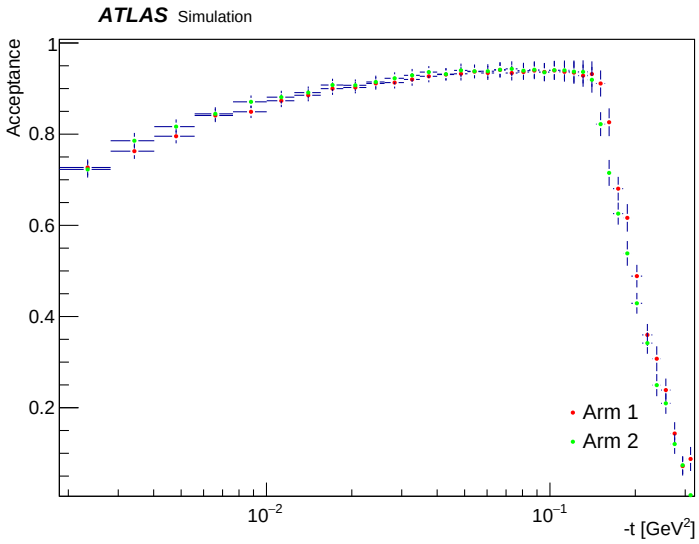

Figure 61: The simulated Mandelstam t-acceptance of the detector using MC of 2×10^7 events.

5.7 Track Reconstruction Efficiency

ALFA does not always reconstruct an elastic track successfully. This is a consequence of a number of factors such as fiber cross-talk, pile-up and the fact that the fibers themselves are not perfectly efficient, for example. This means that some true elastic events are not reconstructed correctly, instead appearing as individual tracks in each detector that composes an arm, or not at all.

The track reconstruction efficiency of a detector arm may be defined as the ratio of the number of events that had a reconstructed track in all four detectors in an arm to the total of all track configurations in which a fragment of an elastic event could have been detected, or missed entirely:

$$\epsilon_{Reco} = \frac{E_4}{E_4 + \sum_C E_3 + \sum_C E_2 + \sum_C E_1 + E_0} \tag{68}$$

where $E_i = N_i - B_i$ refers to the number of elastic events observed N_i, minus background B_i, C refers to the set of permutations of different ways in which such a proton could be observed and the index, i, refers to the topology of detectors in which the elastic event was observed. In actuality, the number of elastic events will be overestimated due to additional background in the sample that cannot be directly removed. This is as a result of there being insufficient information to be able to apply all of the normal elastic cuts. In order to compensate, a factor called an 'Elastic Overestimation Factor' (EOF) may be generated from the cuts available in an MC for a particular detector topology:

$$\epsilon_{Reco} = \frac{E_4}{E_4 + EOF_3 \sum_C E_3 + EOF_2 \sum_C E_2 + EOF_1 \sum_C E_1 + EOF_0 E_0} \tag{69}$$

An estimate of the track reconstruction efficiency was found in this thesis. The EOF values were not examined, as due to the low level of background in the $\beta^* = 2.5$ km campaign the EOFs were considered of little importance with respect to a simple cross-check.

In order to measure the track reconstruction efficiency, the total measured counts for these topologies were measured for events which passed the geometrical acceptance, noise suppression cuts and, if the information was available, the $x - \theta_x$ correlation cuts. This is due to the fact that, for various configurations, the correlation cuts are simply not applicable. Furthermore, cuts that utilize both sides may invalidate the argument set forth in Section 5.7.1 by introducing correlations between the sides of the detector. These values are shown in Table 5.

Track Configuration	Arm 1 w/o trigger	Arm 1 w trigger	Arm 2 w/o trigger	Arm 2 w trigger
1234	291274	291278	280939	280939
123	5367	4732	7996	3795
124	394	379	538	509
134	458	431	1494	427
234	3648	3619	3151	3081
12	22502	22331	31704	30264
34	15281	16478	20802	21911
13	10	6	29	3
14	1	1	2	1
23	83	70	84	39
24	8	6	10	10
1	403	266	1157	259
2	577	480	720	426
3	395	459	753	350
4	131	223	148	120
0	34720	36755	41357	57925

Table 5: The detection topologies of the ALFA experiment for *Run 309166*

5.7.1 Count Estimation using Probability

There are instances of detection permutations that have a single detection on either side of the IP. This is a problem, as it is difficult to isolate elastic events in the case of the E_1 set and impossible for E_0. This is by virtue of the lack of correlation between the two sides of the detector that is normally required for elastic analysis. However, this very fact provides an indirect window to be able to calculate these values from existing information.

A newly developed technique argues that the probability of tracks being reconstructed is independent of the detector side [4]. This makes sense intuitively, as the individual triggers that compose the armlet on either side are independently recorded, with the elastic trigger firing if there is a coincidence. This means that the probabilities of a particular configuration are also independent of side and therefore the joint probability for a process may be factorized between the two sides:

$$E_{abcd} = p_{abcd} \cdot E_{Total} = p_{ab} \cdot p_{cd} \cdot E_{Total} \tag{70}$$

Using this logic, the probabilities of particular instances may be factorized into two components, one for each side of the detector. These may be combined as shown in Section 9.1.2. The results of this method are shown in Table 6. The results can clearly be seen to describe the N_2 topologies, whereas the discrepancies between the estimated and measured N_1 and N_0 topologies are made apparent. The differences are caused by background.

Track Configuration (wt)	Arm 1 Data	Arm 1 Reconstructed	Arm 2 Data	Arm 2 Reconstructed
13	6	7.002	3	5.768
14	1	0.561	1	0.774
23	70	58.793	39	41.619
24	6	4.709	10	5.582
1	266	33.043	259	45.998
2	480	277.453	426	331.899
3	459	267.696	350	295.980
4	223	21.441	120	39.698
0	36755	1263.296	57925	2360.350

Table 6: A comparison of measured counts and their associated reconstructed values for topologies with a trigger firing.

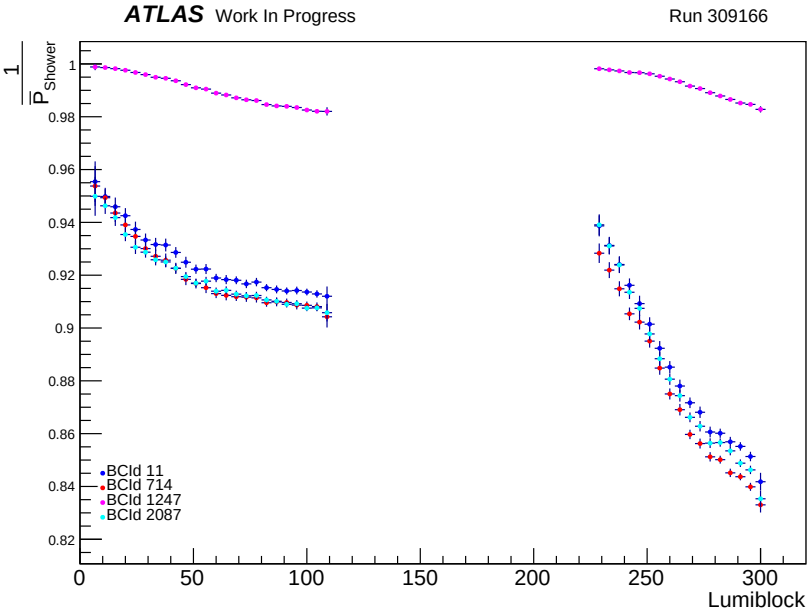

Figure 62: Probability not to have a shower for each paired bunch crossing.

5.7.2 Background Suppression

A primary source of background in this case is upstream showers. These showers will cause a large degree of fiber noise in the detectors. Furthermore, they are very likely to hit both upper and lower detectors on the same side as the arm in question. Therefore, for the sample used to calculate the track reconstruction efficiency, a veto was placed on a track being reconstructed in the corresponding upper (lower) outer detector in the opposite arm of the event of interest. This is because a background event, such as a diffractive or shower event, is the most likely cause of such an observation. Such shower events are then rejected from the track reconstruction efficiency measurement.

It is worthwhile to measure the likelihood of having such a shower and scale the observed topologies by the shower probability in order to obtain the true number of rejected elastic topologies, in order to have a better understanding of the contribution of upstream showers:

$$E_{true} = \frac{E_{ShowerVeto}}{\bar{P}_{Shower}} \tag{71}$$

For the purposes of a simple cross-check, the contribution of the shower probability was not included in the calculation performed in this thesis, since the fact that previous analyses saw little difference between the calculation with and without the shower contribution [4].

The probability for a shower is estimated using the bunch group trigger, which fires randomly throughout the run. Of these random events, those which cause more than 200 fibers to register a hit in the arm are selected, as these are likely to have been upstream showers. The ratio between events which do not have both inner detectors on either side fire given an event and the total is measured in order to obtain the likelihood of an upstream shower not to occur. This allows insight into the contribution of showers to the reconstruction of elastic events.

As shown in Figure 62, it is clear to see the effect of showers increases steadily following scraping, which is due to the re-population of the beam halo. It is interesting to note that in the second part of the run, the probability to have a shower increases much more rapidly than the first half of the run. The reason for the increased development of these showers is unclear. Furthermore, the magnitude of upstream shower events appears to be significant throughout the course of *Run 309166* and worthy of discussion.

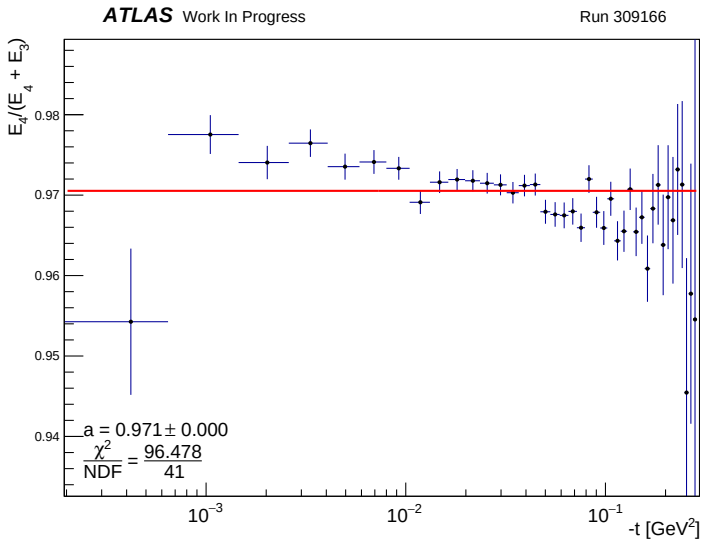

Figure 63: Estimated ϵ_{Reco} as a function of Mandelstam t for Arm 1.

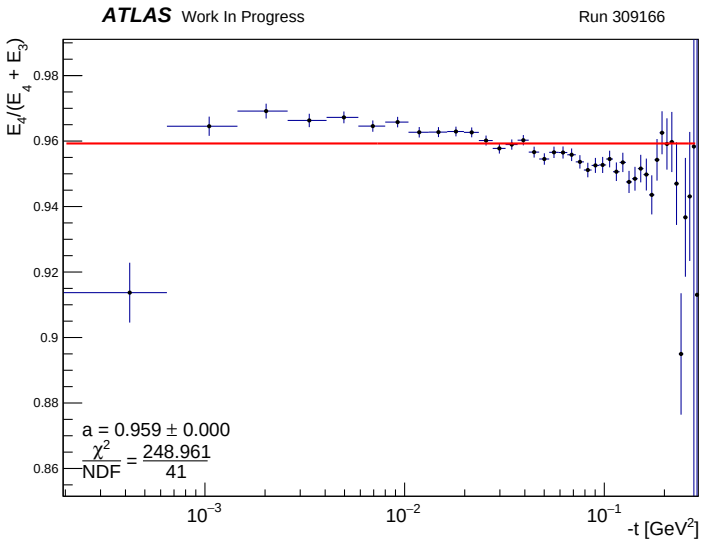

Figure 64: Estimated ϵ_{Reco} as a function of Mandelstam t for Arm 2.

5.7.3 Relationship to Mandelstam t

An important observation to make is whether or not the track reconstruction efficiency is uniform as a function of the geometrical acceptance region and thereby Mandelstam t, especially at the regions of low Mandelstam t where background is largest and results are of most interest. Since the track reconstruction efficiency may be entirely determined using the values for E_4 and E_3, it is sufficient to assess the way that the track reconstruction efficiency is influenced by the geometry of the detector using a simplified track reconstruction efficiency using the ratio of the E_4 to the sum of E_4 and E_3.

As shown in Figure 64, the estimated Mandelstam t is not consistent with a zero-degree polynomial fit. It may thus be argued that the measured track reconstruction efficiency appears to be inconsistent with the hypothesis that the track reconstruction efficiency is independent of the reconstructed t value in this case. This effect is observed independently for both arms. The reason for the reduction in the track reconstruction efficiency with larger Mandelstam t is unclear and has not been observed in prior analyses. It is possible that, in this experiment, poorly functioning fibers in the inner detectors on the A side may have contributed to a worse track reconstruction efficiency in these detectors, influencing the result, as shown in Figures 97 and 98.

5.7.4 Measurement

The track reconstruction efficiency used in this thesis was calculated by a collaborator for both the entire run and specifically *Run 309166*. However, a cross-check was made with the value for the single run in the form of a simplified estimate using the methods defined in this section, albeit not including the additional EOF factors. This was performed to validate the provided measurement. This was possible due to the unparalleled reduction of background that was measured in *Run 309166*.

The resulting values were measured to be within around 0.5% for Arm 1 and around 1% for Arm 2 of the provided values including background contributions, the results of which are shown in Table 7. The differences are most likely due to the absence of the EOFs in this analysis. The systematic errors have been estimated conservatively at 0.2 % in previous analyses [4] and this is carried forth in this thesis.

However, an important observation is that the track reconstruction efficiency varies extensively depending on the time period chosen in the run. This effect is a difference of efficiency by around

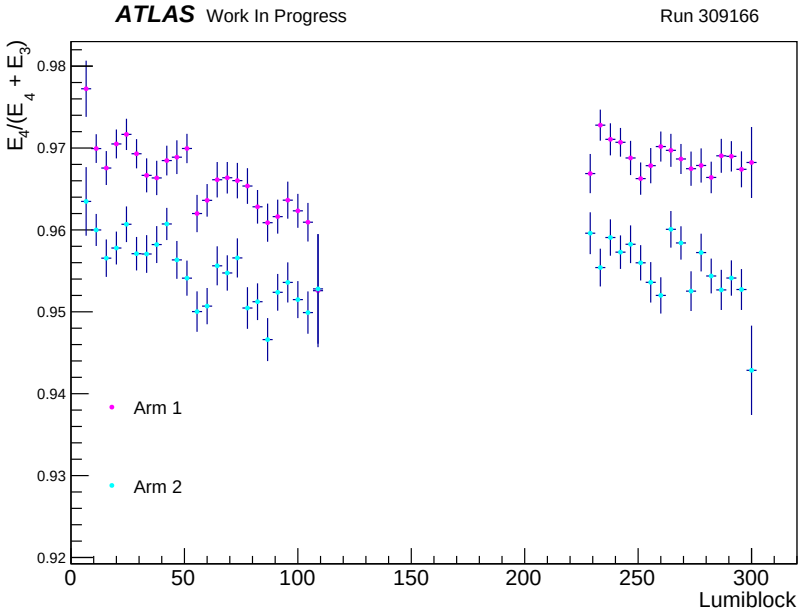

Figure 65: The estimated track reconstruction efficiency as a function of the lumiblock.

2% in Arm 1 and 3% in Arm 2 between periods. This is surprising, as the effect of upstream showers increases in the second part of the run as discussed and shown in Figure 62, and this is the period with the greatest track reconstruction efficiency. It is also surprising that the track reconstruction efficiency varies so much over the course of the run, as this is usually attributed to background. These observations are discussed further in Section 7.3.

ϵ_{Reco}	Arm 1	Arm 2
w trigger & EOF	0.851441 ± 0.02(est syst.)	0.82773 ± 0.02(est syst.)
w trigger	$0.8535 \pm 4.73 \times 10^{-4}$(stat.) ± 0.02(est. syst.)	$0.8164 \pm 4.73 \times 10^{-4}$(stat.) ± 0.02(est. syst.)
w/o trigger	$0.8544 \pm 4.69 \times 10^{-4}$(stat.) ± 0.02(est. syst.)	$0.8019 \pm 4.76 \times 10^{-4}$(stat.) ± 0.02(est. syst.)
$8 < \ell < 107$		
w trigger	$0.843 \pm 6.11 \times 10^{-4}$(stat.) ± 0.02(est. syst.)	$0.805 \pm 6.18 \times 10^{-4}$(stat.) ± 0.02(est. syst.)
w/o trigger	$0.844 \pm 6.11 \times 10^{-4}$(stat.) ± 0.02(est. syst.)	$0.789 \pm 6.09 \times 10^{-4}$(stat.) ± 0.02(est. syst.)
$229 < \ell < 299$		
w trigger	$0.867 \pm 7.24 \times 10^{-4}$(stat.) ± 0.02(est. syst.)	$0.831 \pm 7.42 \times 10^{-4}$(stat.) ± 0.02(est. syst.)
w/o trigger	$0.868 \pm 7.24 \times 10^{-4}$(stat.) ± 0.02(est. syst.)	$0.817 \pm 7.37 \times 10^{-4}$(stat.) ± 0.02(est. syst.)

Table 7: Measured track reconstruction efficiencies. The background with triggers and EOFs was provided by a collaborator, while the other entries were calculated in this thesis to validate the measurement.

5.8 Mandelstam t Reconstruction

There are several techniques by which a reconstruction of Mandelstam t may be performed using measurements of the co-ordinates of elastic protons at ALFA and the transport matrix elements.

5.8.1 Subtraction Method

The subtraction method calculates the scattering angle using the fact that the matrix elements for the u co-ordinate are approximately the same. ($M^A_{O/I,11} \simeq M^C_{O/I,11}$). In this case, the primary effect on resolution is determined by the other matrix element, M_{12}.

$$u^A_{O/I} - u^C_{O/I} = (M^A_{O/I,11} - M^C_{O/I,11})u^* + (M^A_{O/I,12} + M^C_{O/I,12})\theta^*_u \tag{72a}$$

$$(M^A_{O/I,11} - M^C_{O/I,11})u^* \simeq 0 \tag{72b}$$

$$\therefore u^A_{O/I} - u^C_{O/I} = (M^A_{O/I,12} + M^C_{O/I,12})\theta^*_u \tag{72c}$$

$$\therefore \theta^*_u = \frac{u^A_{O/I} - u^C_{O/I}}{M^A_{O/I,12} + M^C_{O/I,12}} \tag{72d}$$

5.8.2 Local Subtraction Method

The local subtraction method allows for the measurement to be made on only one side. The resolution of this method depends primarily on the magnitude of the most significant matrix element used, which in this case is M_{12}.

$$M^{A/C}_{I,11}u^{A/C}_O - M^{A/C}_{I,11}M^{A/C}_{O,11}u^* = (M^{A/C}_{I,11}M^{A/C}_{O,12})\theta^*_u \tag{73a}$$

$$M^{A/C}_{O,11}u^{A/C}_I - M^{A/C}_{I,11}M^{A/C}_{O,11}u^* = (M^{A/C}_{O,11}M^{A/C}_{I,12})\theta^*_u \tag{73b}$$

$$\theta^*_u = \frac{M^{A/C}_{O,11}u^{A/C}_I - M^{A/C}_{I,11}u^{A/C}_O}{(M^{A/C}_{O,11}M^{A/C}_{I,12} - M^{A/C}_{I,11}M^{A/C}_{O,12})} \tag{73c}$$

5.8.3 Local Angle Method

Since the distance between the RPs of an armlet are very small relative to the distance to the IP, we may use the small angle approximation ($\sin\theta \to 0 \simeq \theta$) to obtain the local angle associated with an event:

$$\theta_x \simeq \frac{x_O - x_I}{dz} \tag{74}$$

where x_O and x_I are the positions in the inner and outer detectors in the x co-ordinate and dz is the distance between the detectors. Using the fact that $M^A_{I,21} \simeq M^C_{I,21}$, we may obtain an expression for the scattering angle containing the local angle in a similar way to the subtraction method:

$$\theta^A_{u,I} - \theta^C_{u,I} = (M^A_{I,21} - M^C_{I,21})u^* + (M^A_{I,22} + M^C_{I,22})\theta^*_u \tag{75}$$

$$\theta^*_u = \frac{\theta^A_{u,I} - \theta^C_{u,I}}{M^A_{I,22} + M^C_{I,22}} \tag{76}$$

Also similarly to the subtraction method, the resolution primarily arises from the remaining matrix element term, M_{22}.

5.8.4 Resolution

Of these methods, the subtraction method is superior in terms of resolution. It should be noted, however, that the matrix elements M_{12} for both sides were an order of magnitude larger for the outer detectors than the inner detectors. This implies that the outer detectors give the greatest resolution of Mandelstam t. The subtraction method using the outer detectors for the θ_x^* and outer detectors for θ_y^* is the reconstruction method used henceforth in this thesis. This is of note as normally an average is taken between the θ_y^* values reconstructed using the values from both the inner and outer stations. However, due to unexpected fiber inefficiencies in the A7L1U and A7L1L detectors, discussed in Section 5.11, the outer stations were chosen in order to reduce systematic errors that may have arisen due to this effect.

The RMS difference between the methods and the true Mandelstam t distribution produced in MC are given in Figure 66. The theoretical resolutions of the θ_x^* values for different methods are given by the width of the distribution between the true value and that which has been reconstructed. These are shown in Table 8.

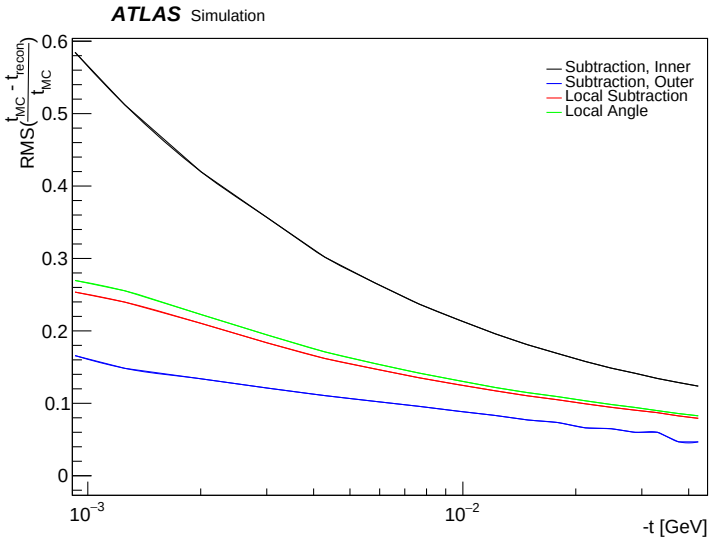

Figure 66: The RMS difference between the various methods of calculating Mandelstam t.

Method	Smearing and Emittance	Resolution Smearing only	Emittance only
Subtraction, Inner	2.30	2.30	2.30
Subtraction, Outer	0.71	0.71	0.69
Local Angle	1.28	1.28	1.27
Local Subtraction	1.20	1.20	1.18

Table 8: Resolutions of the various θ_x reconstruction methods given in μrads.

5.9 Background Estimation

It is paramount that the background contribution to the overall measurement made during the experiment is considered. Background for the ALFA detector for elastic events consists of two main sources: Double Pomeron Exchange (DPE) and Beam Halo (BH).

DPE events refer to those where scattering protons interact via virtual particles known as pomerons. The pomeron is a hypothetical boson defined as a colour singlet with quantum numbers of the vacuum [28]. In this case, protons scatter in a similar manner to elastic scattering but with the addition of jets produced from the fracture of the pomeron ($p + p \rightarrow p + X + p$). This type of event is currently understood in the paradigm of Regge Theory, which is beyond the scope of this thesis. However, DPE is an inelastic proton scattering process and contributes to the overall

proton scattering cross-section. DPE Events may appear very similar to elastic events if they lose only a small amount of energy. This process contributes to the elastic background as, unlike single diffractive and other types of diffractive background, the two protons remain intact following the collision and, assuming the energy loss is sufficiently low, may be mistaken for an elastic event in ALFA.

Events observed due to the beam halo are less well understood from a theoretical standpoint. In fact, little consensus has been reached as to the precise definition of beam halo [29]. A simple, if limited, description is that beam halo protons are those which diverge from the main beam yet still satisfy the conditions to oscillate as part of the bunch. These wayward protons can fire the elastic trigger should there be a coincidental trigger caused by two unrelated beam halo protons.

There currently exist two valid background estimation techniques, both of which make for robust tools for examining the contribution to the elastic data sample. Single track events were used in both cases to lower the contribution of detector noise to the background estimation. These methods are discussed in Sections 5.9.1 and 5.9.2. The absolute count of background events are scaled to data for the method used in this thesis and therefore as many events as possible may be used in the template to improve the quality of the estimate.

5.9.1 Antigolden Background

Antigolden events refer to those events where a pair of protons were observed in both upper stations or both lower stations on each side of the IP. Events with this signature cannot be elastic and thus may be used to estimate the background.

Events for which a specific antigolden trigger fired and where tracks were reconstructed in all of the upper detectors and no tracks were reconstructed in the lower ones, or vice versa, constitute a true antigolden event. If such an event is found, the y co-ordinates of the event detected on the C side are flipped such that the event appears as though it were an elastic. It is then required that such an event pass the elastic criteria discussed in Section 5.1. The proportion of background in this case is yielded by the number of events that are able to pass.

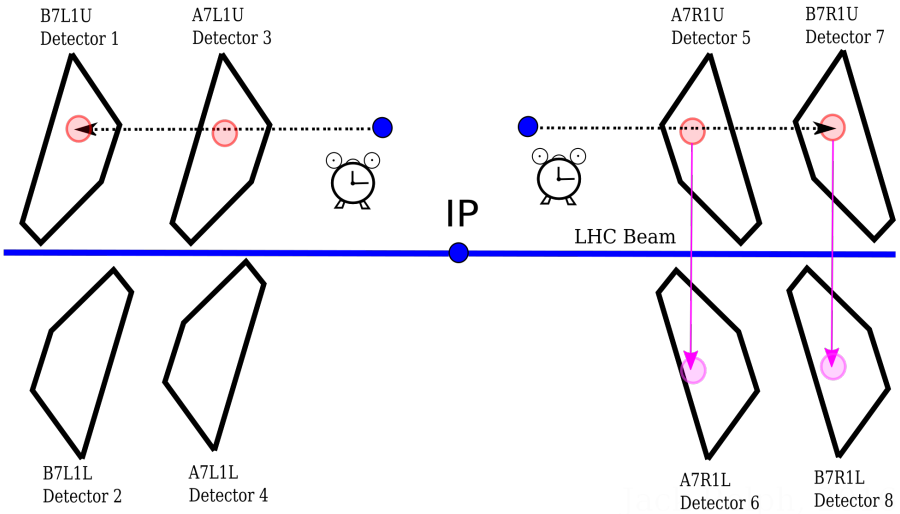

Figure 67: Diagram describing visually the antigolden background. The purple arrows indicate that the event is treated as having been detected at where the arrows point. The clocks indicate the relative difference in time between when the two events were observed.

A caveat of this method is that it requires all the detectors to be the same distance from the beam. This is, however, not so in reality. Since a detector armlet closer to the beam would be able to observe a lower set of t values than could ever be possible at an armlet further from the beam, error is introduced by direct comparison to data using this method. This is because the

t-spectrum would be over or understated where the distances to the beam of the upper pots were not the same as the lower.

An analysis was made of events which triggered in the antigolden channel (L1_ALFA_SYST11 and L1_ALFA_SYST12). This yielded a very low degree of background relative to the number of elastics observed in the experiment. The structure of the plots also suggested a background predominantly consisting of DPE events, exhibiting very small region of beam halo particles. The distribution of background events in this case is unremarkable except for the low magnitude of beam halo background in the sample.

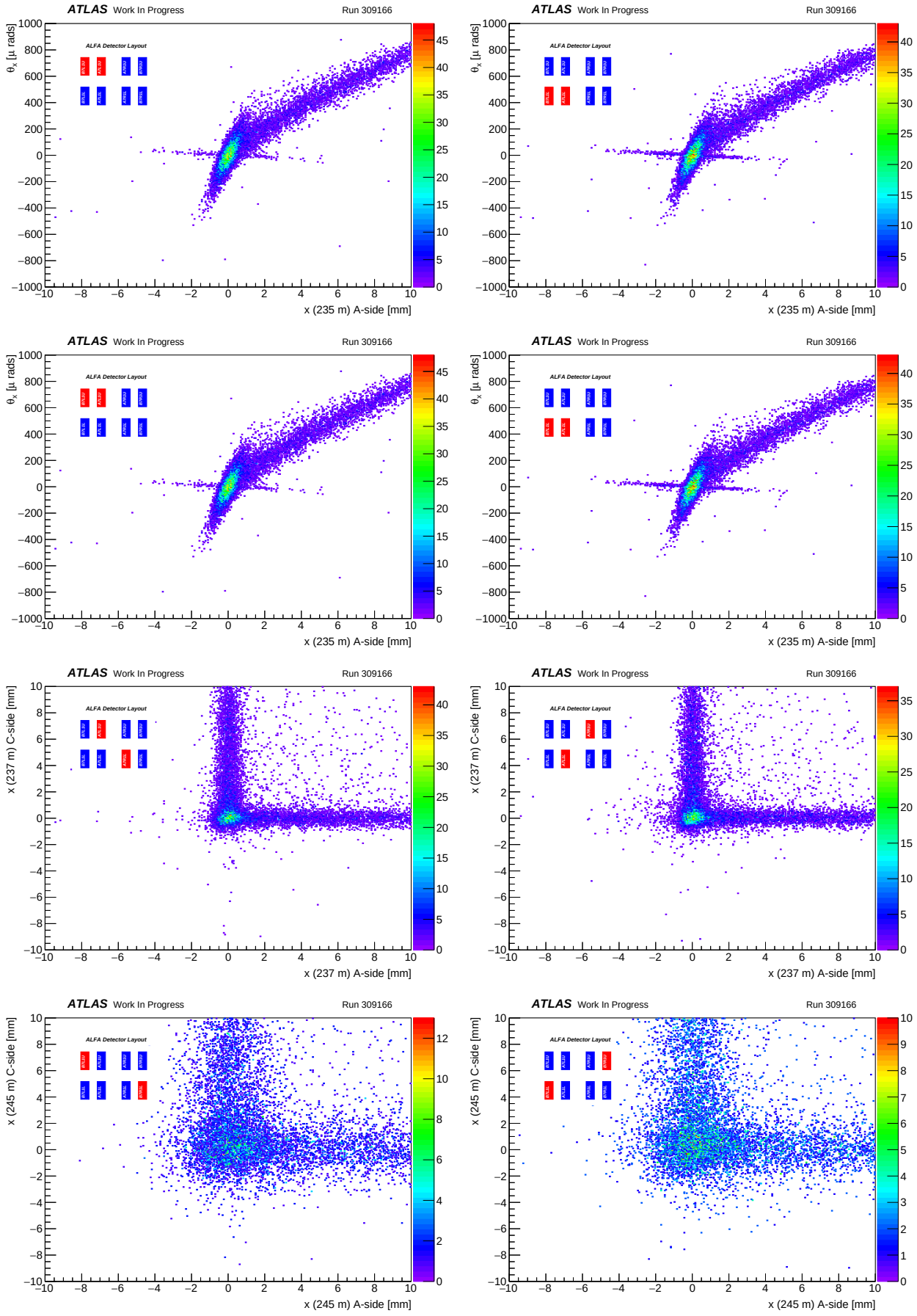

Figure 68: Correlation plots for RUC with all geometric and track quality cuts except back-to-back cuts. Note that the upper and lower C-Side detectors have been swapped around for the antigolden analysis.

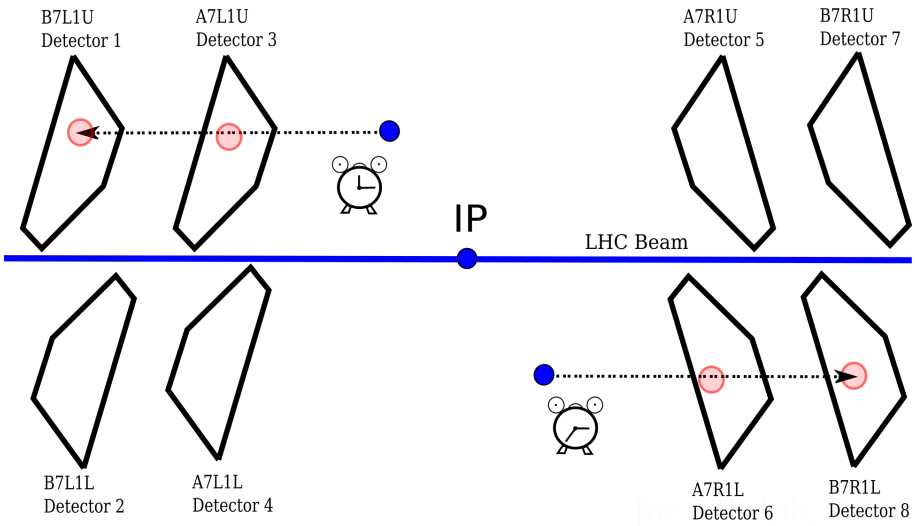

Figure 69: Diagram describing visually the RUC background process. The clocks indicate the relative difference in time between when the two events were observed.

5.9.2 Random Uncorrelated Background

The other currently existing method for estimating background is to combine uncorrelated events that have a tracks reconstructed in both of the two sets of detectors that constitute an arm independently of one another. This is referred to henceforth as a *Random Uncorrelated Coincidence* type event (RUC). An event that has reconstructed tracks in one station is combined with an event with reconstructed tracks in the corresponding station on the other side of the arm. It is a requirement that there is no track in any other detector than these stations. Such events are completely uncorrelated, and therefore combining them will yield an event which has no basis in elastic scattering. As with the antigolden method, if such an event is able to pass the elastic criteria then this event represents a hypothetical background event that would be able to pass the elastic trigger.

The benefit of this method over the former is that it takes into account the positions of the RPs, since all the alignment of the detection in the arm is the same as that which is used for the elastic measurement, thus solving the aforementioned alignment problem. This was the method selected for use in this thesis.

With the expectation of a predominantly diffractive background, events were combined as per the aforementioned RUC background method and compared. Significant and unexpected differences were observed between the antigolden background and the RUC. A surprising and unexpected result of this analysis is that the correlation plots of the RUC sample shown in Figure 70 exhibit unexpected behavior that does not appear in the background for antigolden events. There is a regular banding structure that appears at the tails of the background ellipse at around $x \simeq -5$ mm and $x \simeq 5$ mm for all detectors, which will be referred to henceforth as the *TIE Fighter* structure in reference to the shape of the $x - \theta_x$ correlation plots. This effect has not been previously observed in prior ALFA elastic analyses of background, nor is such an effect observed in the elastic sample. As such, the validity of the RUC method must be examined in order to make further use of the method in background analysis.

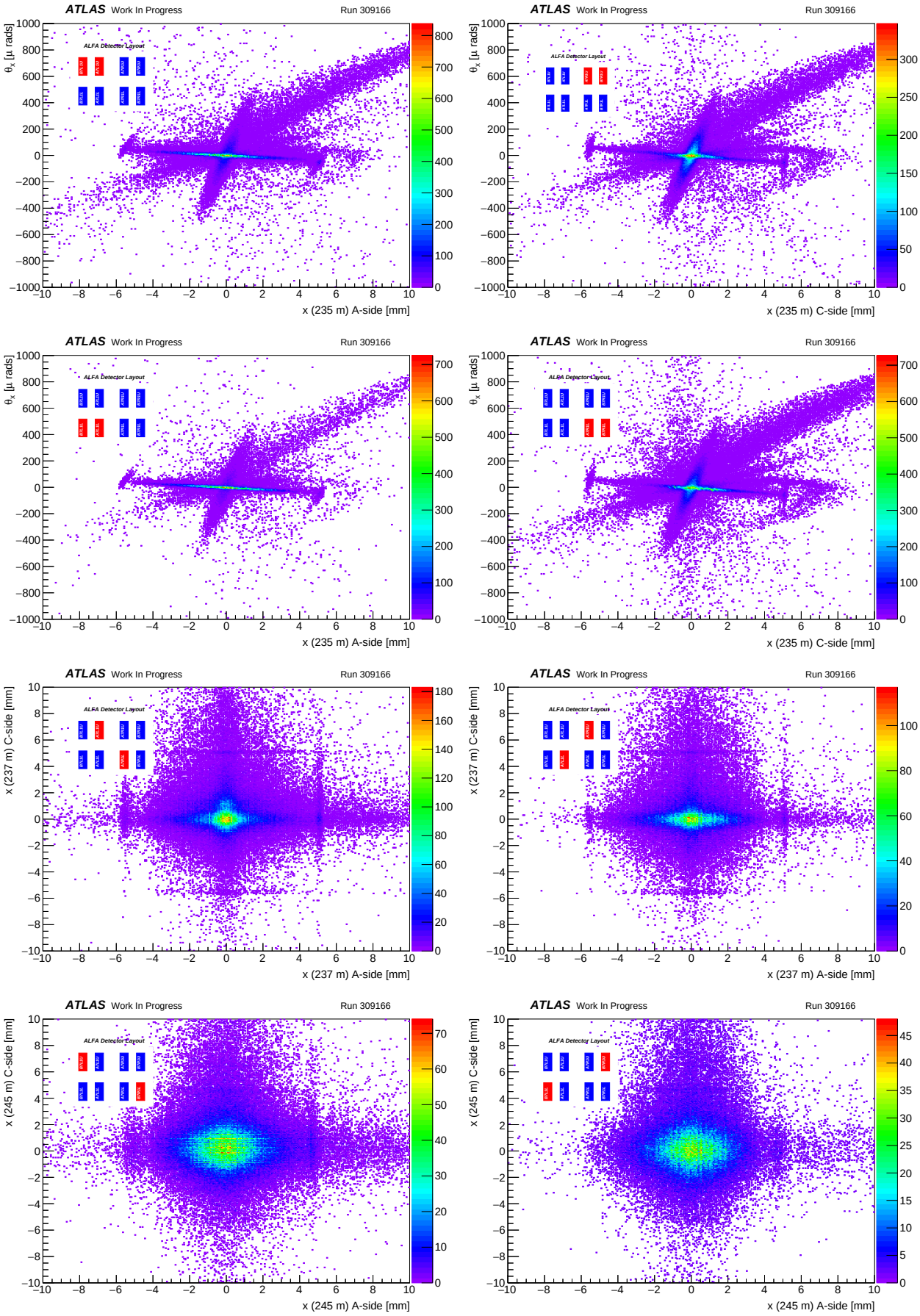

Figure 70: Correlation plots for RUC with all geometric and track quality cuts except back-to-back cuts, with a veto on events which had an MBTS trigger, and no information about whether or not a LUCID trigger fired.

5.9.3 Discussion of RUC Background

The unexpected behavior of the RUC background is worthy of note. The behavior observed was not present during previous analyses. This lends some credence to the hypothesis that, due to the sheer level of reduction of background for this campaign compared to previous analyses, new effects may have become relevant in the background template that were previously obscured by ordinary beam halo background. Due to the presence of this behavior in the background scaling region and the apparent disparity between the RUC and antigolden background, the effect was too important to neglect in analysis. In the following section, an attempt has been made to discuss and analyze the *TIE Fighter* structure in order to discern some insight into its nature.

5.9.3.1 Observations

The first and simplest explanation of this effect are standard fake tracks or fiber mis-mapping. However, the structure is regular and is observed in every armlet independently, meaning that the effect is consistent across the detector and therefore unlikely to be caused by fiber effects. It was noted, however, that a similar effect to the *TIE Fighter* effect is enhanced when the edge cut is removed. A region of the detectors A7R1L and B7R1L exhibit a similar, significantly more prominent structure at $x \simeq 1.5$ mm. This region corresponds to a hot-spot of fiber activity below the detector edge that is cut away during normal analysis. Although this effect is isolated to a single armlet, it could imply the *TIE Fighter* and this effect have similar causes. It is, however, unclear as to why this effect occurred in only one detector while the *TIE Fighter* appears in all detectors.

If the hypothesis that the structure at $x \simeq 1.5$ mm and the *TIE Fighter* describe the same effect is true, it would imply that the behavior observed is asymmetrical with respect to the IP and would therefore suggest that a proton scattering process at the IP is a less probable cause of the effect than interaction with some aspect of the LHC machine, as this is far more likely to cause the asymmetries between independent detectors on either side of the IP in the observed distributions than a scattering process is. Furthermore, it was observed that the *TIE Fighter* effect was more prevalent for the inner stations than the outer stations, which could imply protons scattering into the detector from a regular external structure, such as the collimators or the LHC Beamscreen. This would, however, imply that the structure with which the protons are scattering through is the same for each inner detector of ALFA. Due to the observed position of the effect at the very edges of the main beam halo ellipse in the x co-ordinates of the LHC, the horizontal collimators are the most likely candidate for the cause of the effect, though this would require further analysis beyond the scope of this thesis to qualify.

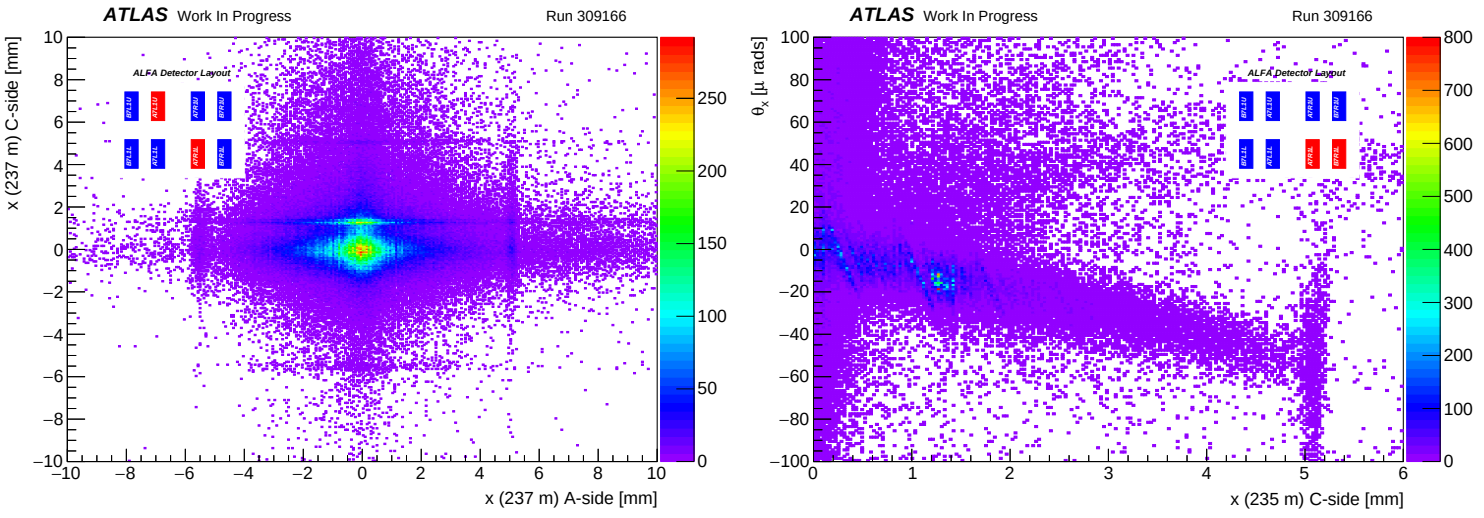

Figure 71: Plots of the inner and station correlation plots with the edge cut removed for Arm 1.

5.9.3.2 Analysis of Diffractive Contribution

In order to examine diffractive-type events and to further examine the effect of the *TIE Fighter* structure in this context, RUC events were selected with triggers in the ATLAS MBTS detector and the LUCID detector, resulting in a further two datasets of RUC being combined. These RUC events were only combined with other RUC events with the relevant trigger having fired for both. For example, the dataset generated for the MBTS trigger vetoed on all events that did not have this trigger. This was to avoid unwanted correlations between diffractive and beam halo background.

The MBTS and LUCID detectors nearly always trigger on diffractive events. The main MBTS trigger used (L1_MBTS_2) required that there was a hit in at least two of the eight detector plates. The correlations of interest for events combined only with an MBTS trigger are shown in Figure 73. The LUCID trigger (L1_LUCID) merely requires that the detector triggered on an event. The correlations of interest for events combined only with an LUCID trigger are shown in Figure 74. The two datasets reflected the features a predominantly diffractive background, as expected. However, the *TIE Fighter* effect remained to varying degrees in both samples in all detectors, though markedly less so for the LUCID trigger.

A further analysis was made of the ratio of these types of events to the entire background dataset as a function of lumiblock. A measurement was made for each armlet of the relative proportion of events in which the MBTS trigger fired or the LUCID trigger fired, or both, following all track quality and geometric cuts except the *back-to-back* cuts. For all detector armlets, the observed proportion of diffractive-like events was consistent with the de-population of halo background following scraping. For this reason, the diffractive background is at maximum immediately after scraping and falls off further into the run as the overall background became more heavily populated with beam halo.

The largest disparity between the proportion of background events with the MBTS and LUCID trigger, shown in Figures 75 and 76 respectively, was observed in Arm 2. In the case of the MBTS trigger, there was approximately a 5% difference between the level observed independently between stations of the arm over the course of *Run 309166*, which reduced more significantly for the lower station than the upper. These facts suggests that Arm 2 experienced the greatest disparity in terms of beam halo background, as the absolute amount of diffractive background does not vary throughout. The disparity in the proportion of background may occur when the beam has a slight crossing angle, which causes more beam halo to be observable in the lower detectors than the upper detectors in this case.

A dataset with a stricter MBTS trigger specific to the side of the IP (L1_MBTS_4_A and L1_MBTS_4_C), which required four plates on the MBTS firing on one side of the IP was used to investigate the *TIE Fighter* further. This dataset was also analyzed as per the above, with the expectation that the diffractive-type events would be observed as having a MBTS trigger on the opposite side of the detector to which the diffractive event was observed. This was true for the majority of events. However, there was a small proportion of the RUC events with a MBTS trigger on the same side as the proton track was reconstructed. This small sample was correlated strongly with the *TIE Fighter*, which is shown in Figure 72. The apparent conclusion from this result is that the behavior associated with the *TIE Fighter* is not a phenomenon necessarily associated with diffractive events in particular.

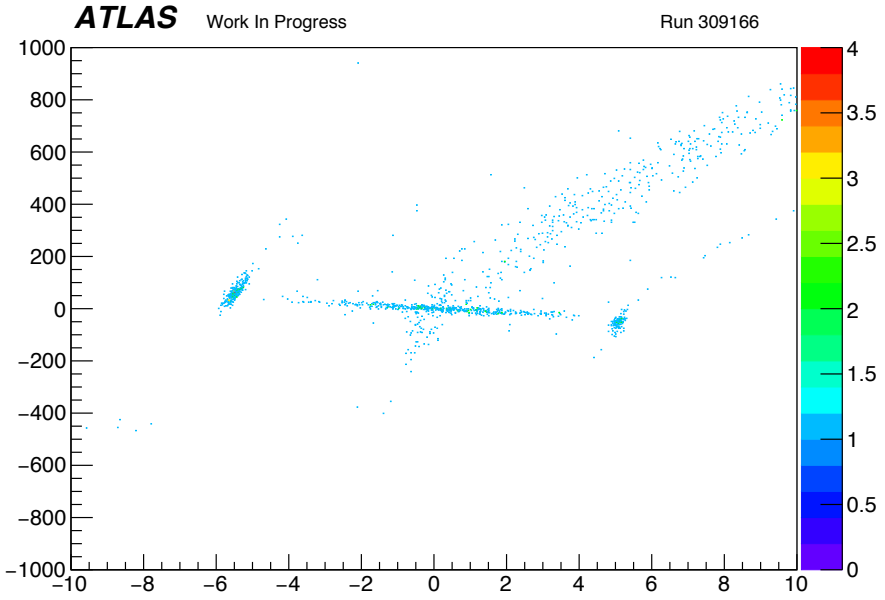

Figure 72: The $x - \theta_x$ correlation plot for events with a MBTS trigger on the same detector side as the event was detected.

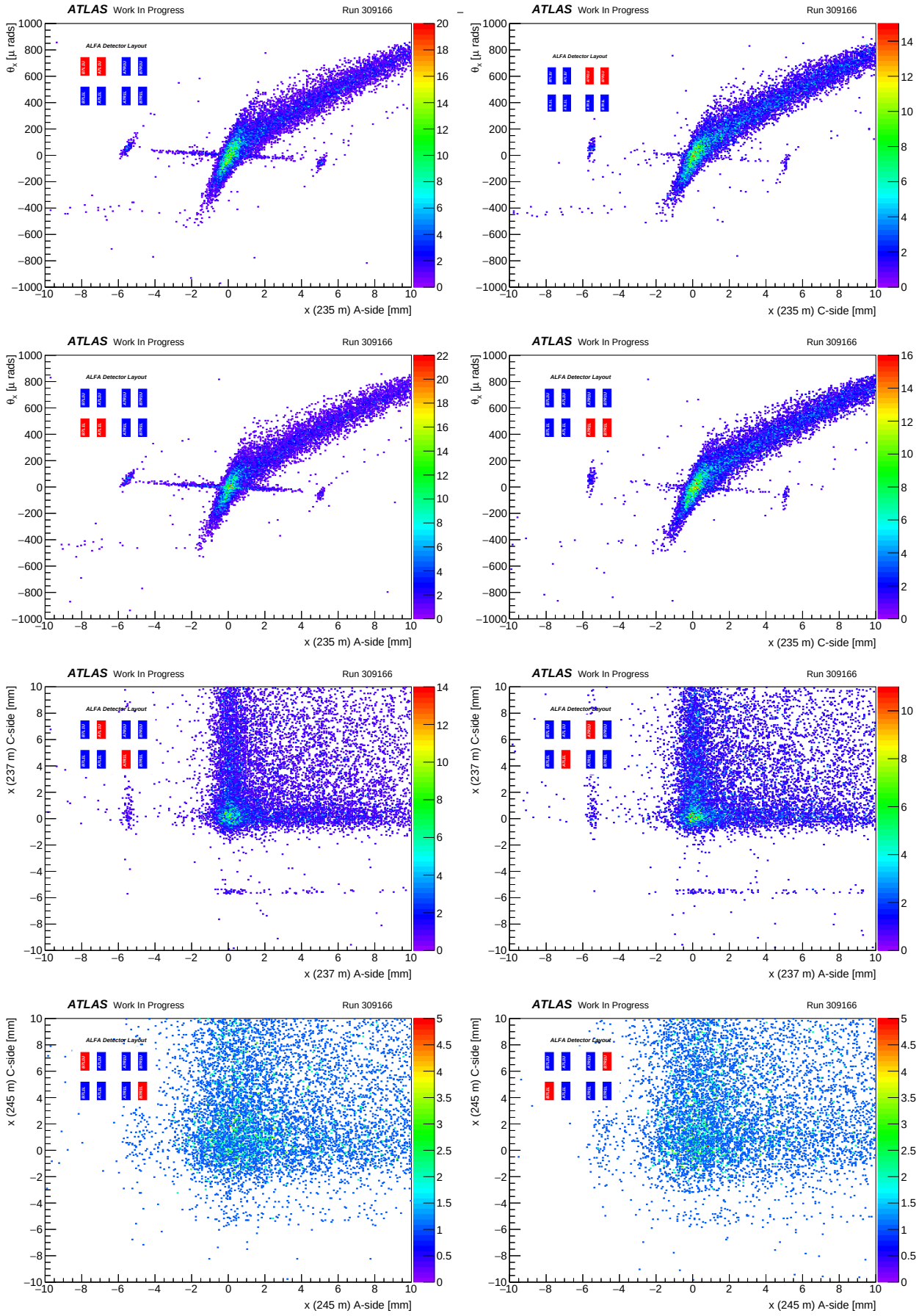

Figure 73: Correlation plots for RUC with all geometric and track quality cuts except back-to-back cuts, with a veto on events which did not have an MBTS trigger, and no information about whether or not a LUCID trigger fired.

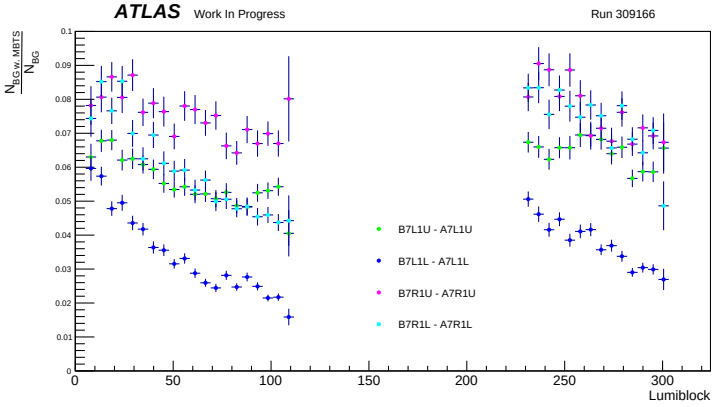

Figure 75: The ratio of background events where the MBTS trigger fired to the total background events for each armlet, following following all track quality and detector geometric cuts.

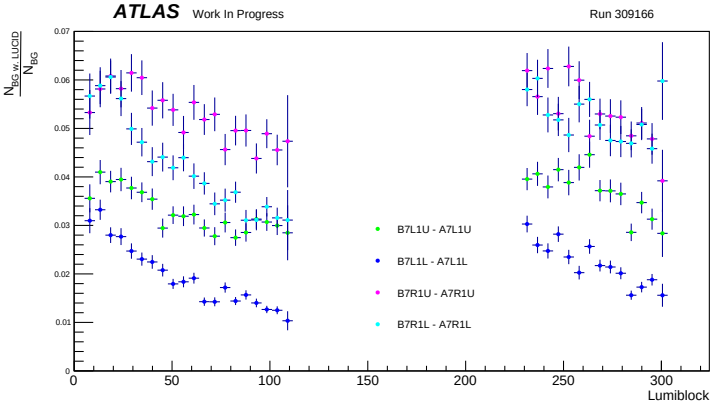

Figure 76: The ratio of background events where the LUCID trigger fired to the total background events for each armlet, following following all track quality and detector geometric cuts.

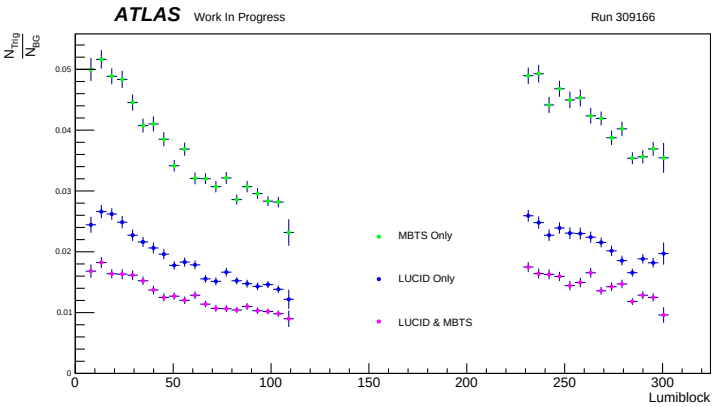

Figure 77: The ratio of background events where the LUCID trigger without the MBTS, the MBTS trigger fired without the LUCID trigger, and both triggers fired simultaneously to the total background events over the entire set of armlets, following following all track quality and detector geometric cuts.

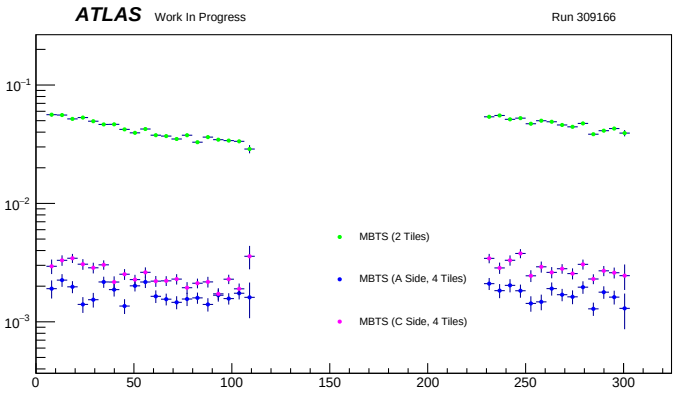

Figure 78: The ratio of background events for the MBTS trigger used in the main analysis and the more stringent MBTS triggers on either side of the detector to the total background events over the entire set of armlets, following following all track quality and detector geometric cuts.

5.9.3.3 RUC in Unpaired Bunches

In light of the analysis of the MBTS and LUCID triggers, a further analysis was performed on unpaired LHC bunch crossings. A further choice was made to not veto on activity in the other side of the detector except for on elastic triggers. This was in order to attempt to mitigate accidental correlations between the armlets as best as possible and to maximize the available data for analysis.

Each bunch crossing the LHC has a specific identification number, known as a BCID. This information exists because ATLAS does not have the computational power to be able to process all trigger signals in the 25 ns time frame between bunch crossings. Consequently, the Level 1 Calorimeter stores information in regards to when data from an event was detected so the problem of triggering in the wrong bunch crossing may be dealt with later. In the case of this example, the bunch crossings used in this sample had only one bunch and did not collide. Consequently, the events observed in ALFA will be composed of entirely beam halo since no scattering should occur.

Due to the low number of events in this dataset, the *TIE Fighter* region was not obviously visible in the correlation plots. As such, the x-distributions of the main dataset and the unpaired dataset were compared. It was observed that unpaired sample exhibited the same properties as the main sample of background. It was observed that the peak at 5 mm was present in three of the four inner detectors, well outside the error on the measured values.

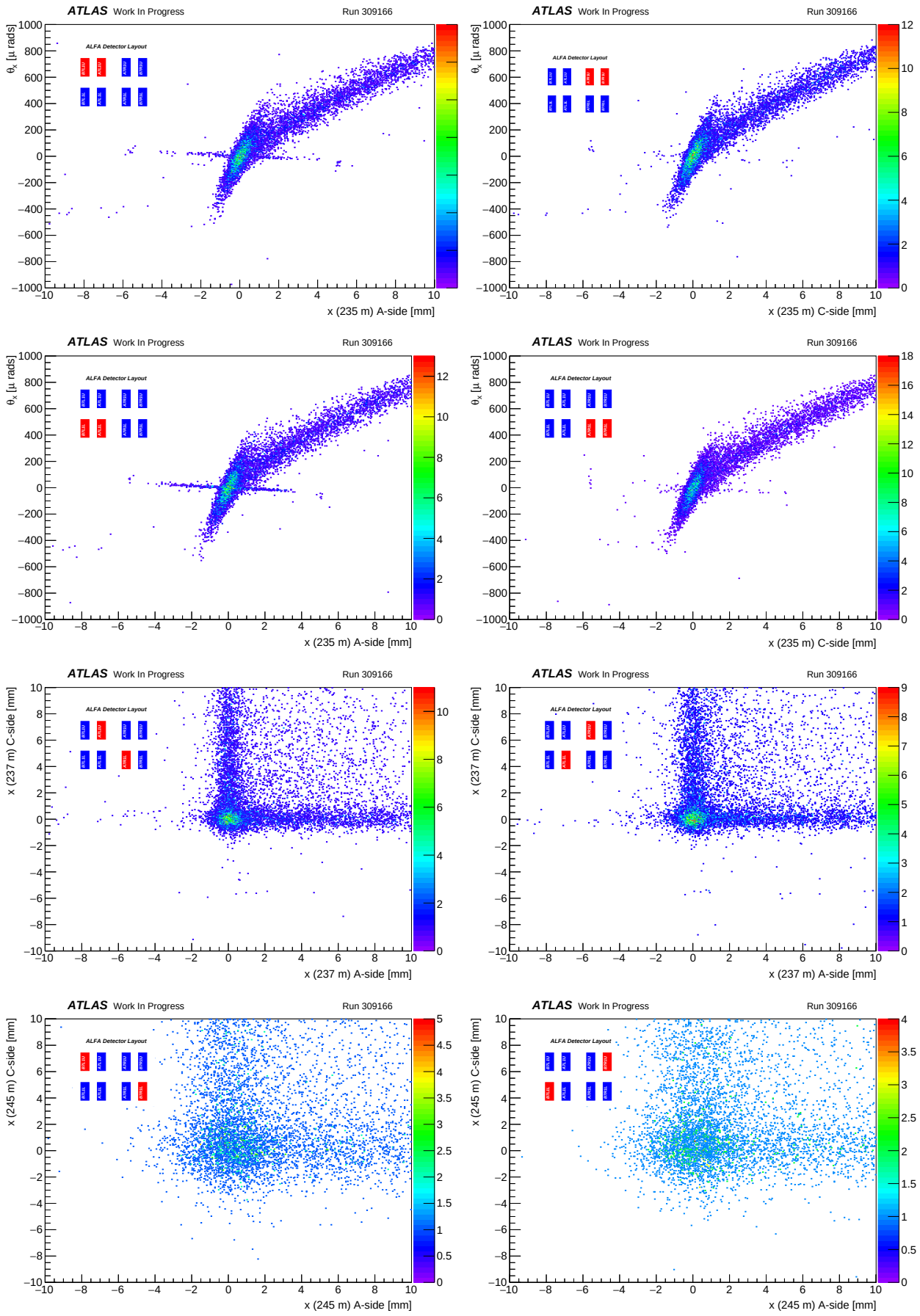

Figure 74: Correlation plots for RUC with a veto on events which did not have a LUCID trigger, and no information about whether or not a MBTS trigger fired.

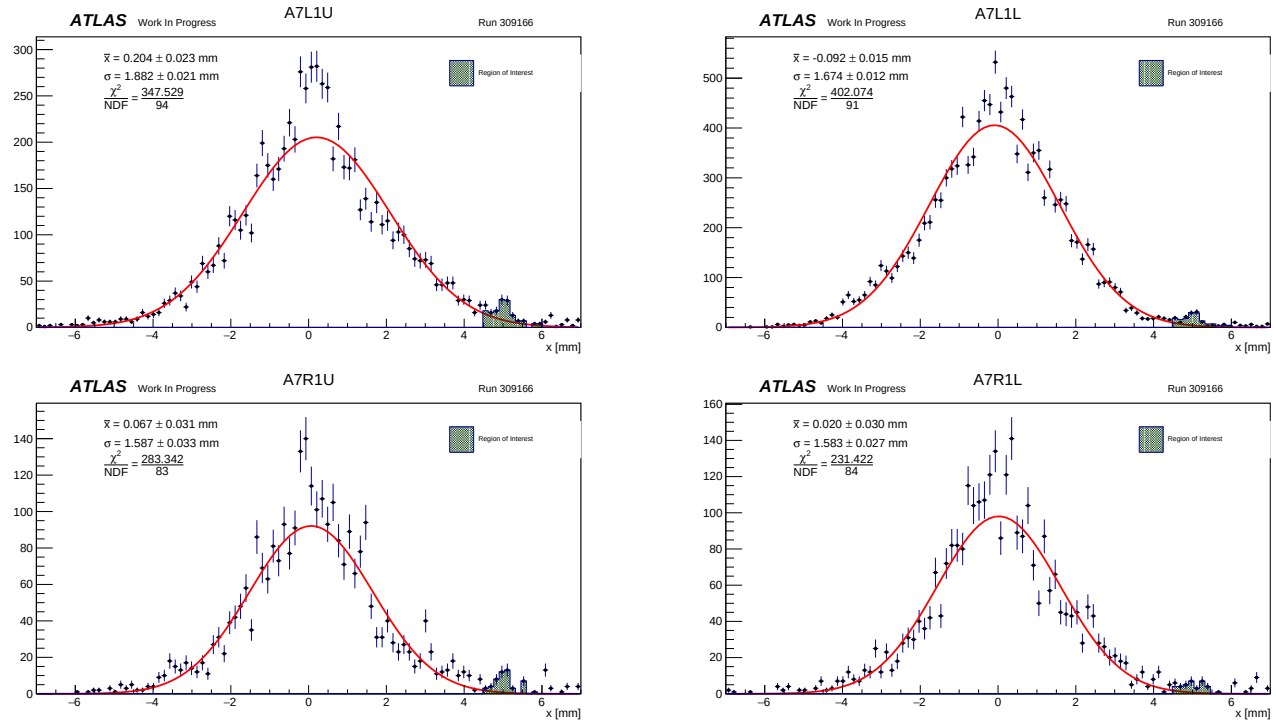

Figure 79: The x-distributions observed for unpaired bunch crossings in the inner detectors.

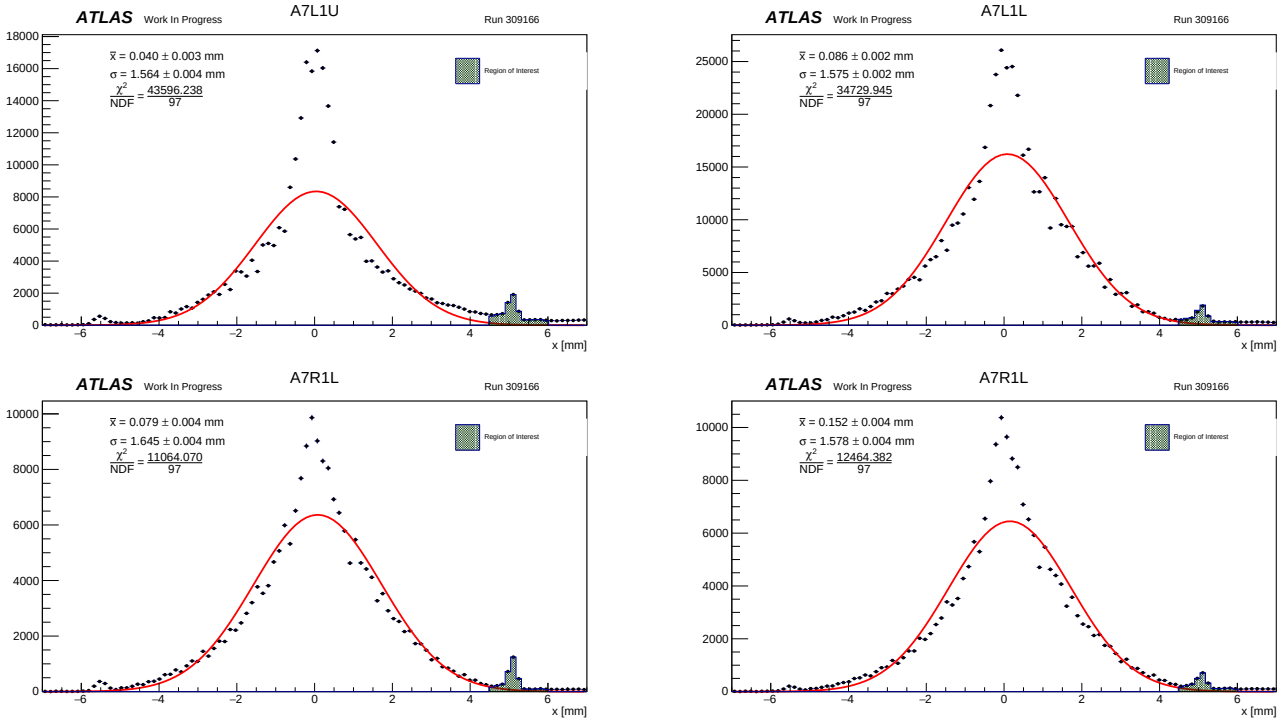

Figure 80: The x-distributions observed for the entire background sample in the inner detectors.

5.9.3.4 Showers

To investigate showers, the proportion of events with a shower trigger, (L1_ALFA_SHOWSYST5) to the total background dataset was found. This trigger fires if any number of the triggers on either side of the detector fire simultaneously. This is shown in Figure 81.

It is of particular note that the B7L1L - A7L1L armlet has a significantly higher percentage

of events with a shower trigger than the other armlets during the first half of the run. This is also in contrast to a different shower measurement performed in the track reconstruction efficiency analysis discussed in Section 5.7.

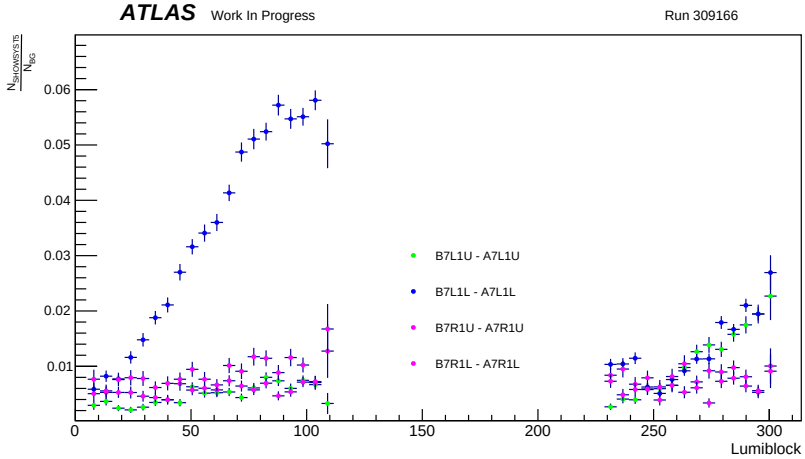

Figure 81: Ratio of RUC events with a shower trigger to the RUC sample.

5.9.3.5 Beam Gas Collisions

It is possible that a beam gas collision would yield an elastic structure with events on the same side of the detector with a small apparent energy difference directly proportional to the square of the scattering angle. The reasons for this are related to reference frame dependencies, and are discussed in Section 9.1.1. Such an event is highly unlikely to be observed, given that the number of molecules per meter cubed in the LHC beam pipe is 5 molecules/m^3 [17]. However, it was deemed that this was a potential avenue of research to discover the source of the *TIE Fighter* structure, since this occurrence was theoretically possible and may help explain the deviations in the scattering angle observed. A stationary hydrogen atom has a proton nucleus, and therefore it is reasonable to consider that such a particle would scatter much like a proton would at the energies of the LHC.

Beam gas scattering events would have a different centre of mass energy to that of the normal protons and would travel in the direction of the incident proton in the lab frame. To examine this structure, it is possible to simply reuse the antigolden background method by performing the elastic analysis on particles observed simultaneously on the same side of the detector, treating those events observed on the lower detectors as if they had been observed on the other side of the detector and then performing the same elastic cuts. This is shown in Figure 82.

The analysis shows that there is indeed an weak structure within the correlation plots distinct from the beam halo, though it is not clear whether or not these events are the described collisions with beam gas without a simulation. Furthermore, the *TIE Fighter* structure does not seem to be more correlated in these plots. No structures of interest could be seen in the x_I or x_O correlation plots, and consequently these were not included.

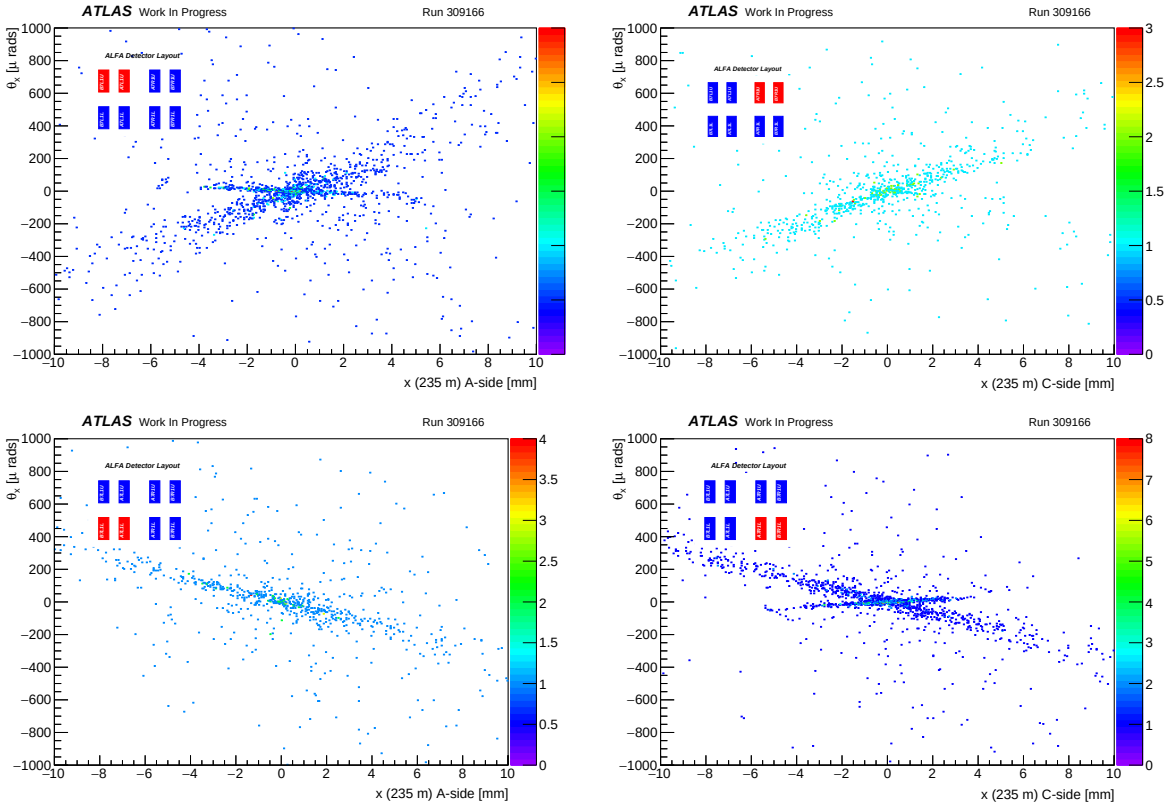

Figure 82: The $x - \theta_x$-distributions observed for same-side elastic candidates with all detector and geometric cuts applied except the back-to-back cuts. Note that the lower detectors have been swapped around for the same-side elastic analysis.

5.9.3.6 Mandelstam t-spectrum Analysis

A measurement of the t spectrum was performed for independent detector stations using the local angle method (see Section 5.8.2). An adjustment was made to the reconstruction of the y scattering angle, as this usually uses the subtraction method. In this case, no correlations were available between the sides of the arm. Therefore, the local angle method was applied for both x and y. The t-spectra of the independent stations were added arm-wise. All detector and geometric cuts were applied, not including back-to-back cuts, and the *TIE Fighter* effect was isolated by a simple cut to isolate events which were observed in the regions $-6 < x < -4.5$ mm and $4.5 < x < 6$ mm in the inner detectors of each station. The result is shown in Figure 83.

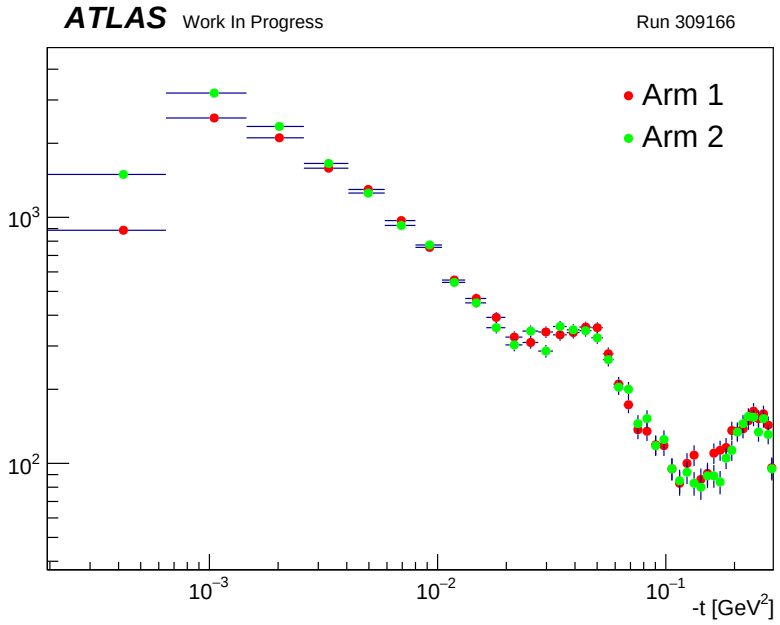

Figure 83: Mandelstam t-spectra of the *TIE Fighter* region for combined independent RUC measurements, with all detector and geometric cuts applied except back to back cuts.

The resulting t-spectrum appears to be consistent with the shape of RUC background, as shown in Figure 91. However, it is notable that there appears to be some form of anomalous peak region around $-t = 4 \times 10^{-2}$ GeV^{-2}, as well as for $-t > 0.1$ GeV^{-2}. The reasons for these observations are currently unknown.

5.9.3.7 Further Comments

This section has demonstrated that the *TIE Fighter* effect had no explanation that could be described using available information. The behavior of the RUC was not understood and did not correspond to what was seen in data, regardless of the associated triggers applied. It is only possible to estimate that, due to the behavior being isolated in events where the MBTS fired on the same side as the event was observed, as well as being observed for unpaired bunches too, that the *TIE Fighter* is likely a beam halo phenomenon. This is surprising as the structure of the *TIE Fighter* wings appear to have similar properties of elastics and a weak diffractive tail.

At present, the most probable cause is scattering from the collimators which are placed on either side of the beam. However, it is impossible to qualify this hypothesis without further investigation. It is hoped that further analyses will shed light on the nature of this effect.

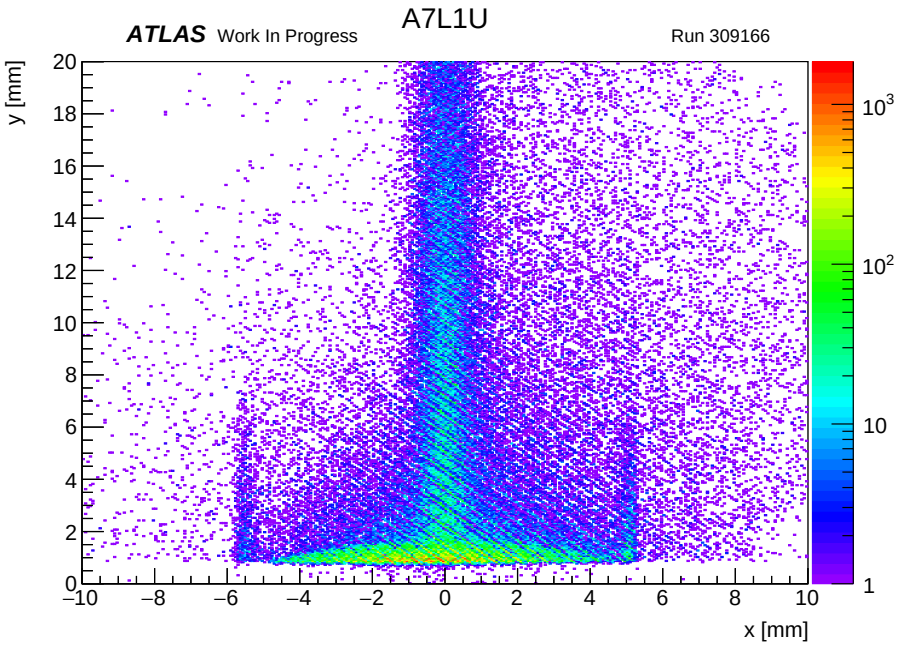

Figure 84: The hitmap of detector A7L1U for RUC background.

5.9.4 Background Scaling

Having produced the background templates for the RUC the relationship between the relative magnitude of events that passed the selection criteria between template and data may be found. The DPE background template shown was produced from a MC provided by a collaborator. These type of events exhibit energy losses and consequently require a more complex simulation of the transport of protons from the IP to ALFA than for elastic events.

Once a background template has been obtained, a region of the relevant co-ordinate spaces for correlation plots where observed protons lie beyond 3σ of the criteria for an elastic event are selected. This is performed for both DPE or RUC background. The contribution to background is then simply taken to be the t-spectrum of events found that pass the detector selection criteria, scaled by the ratio of the events observed in these regions between the background estimate and the actual data. In this way, the estimate may represent the number of events that were actually observed there. The RUC scaling regions are shown in Figures 85, 87 and 89, while the DPE scaling regions are shown in Figures 86, 88 and 90.

In this experiment, the RUC events were scaled according to two regions that were selected where a predominant level of each type of background was observed. These regions were chosen based on previous analyses [4]. It should be noted that a degree of cross-contamination of background was observed between RUC and DPE background, in spite of efforts to use the MBTS or LUCID trigger to remove diffractive contributions. Furthermore, the structure of the beam halo background in this sample is not well understood, and consequently it was impossible to tell as to whether the *TIE Fighter* and the other unknown effects were present in the elastic sample with low statistics or an independent effect only observed in the RUC background templates. However, by virtue of the contribution being observed in unpaired bunch crossings, it may be cautiously assumed that the behavior was present in all potential samples but cut away due to the requirement of simultaneity between triggers on both sides of the detector in the elastic sample.

The t-spectra of the scaled contribution of background with respect to the elastic sample have been included in Figure 91. The aforementioned caveats aside, the scaled background is shown to be in good agreement with the antigolden sample, and was found to be in the order of the part per mille of the signal. At this order, any time dependence of background was considered negligible and was not considered. Overall, the background observed was lower than in any previous elastic analysis at ALFA.

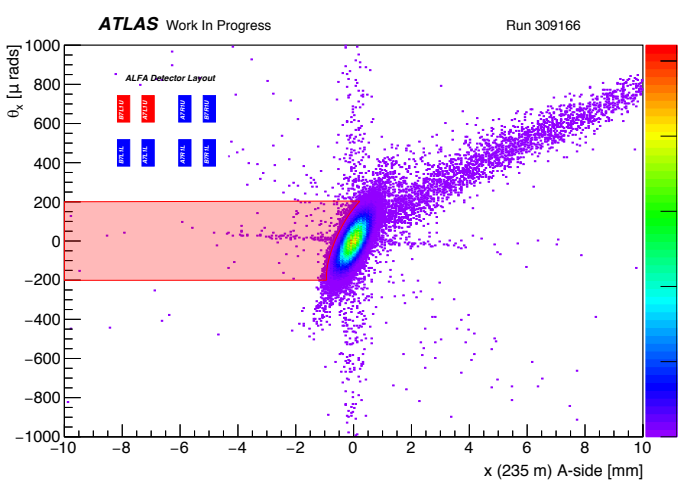

Figure 85: Elastic sample with RUC scaling region overlaid in red.

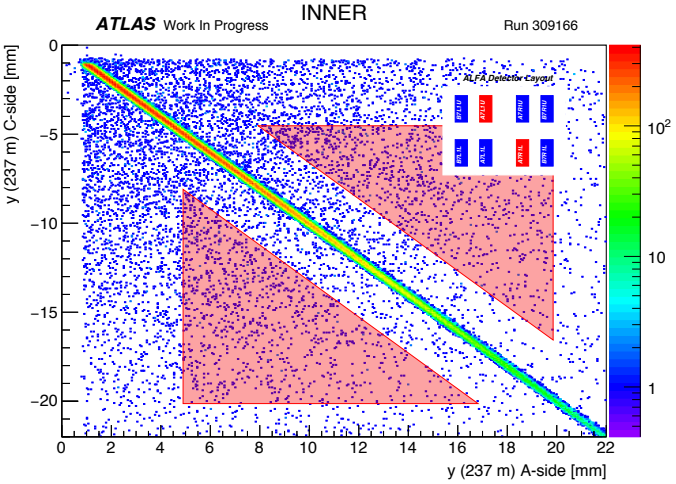

Figure 86: Elastic sample with DPE scaling region overlaid in red.

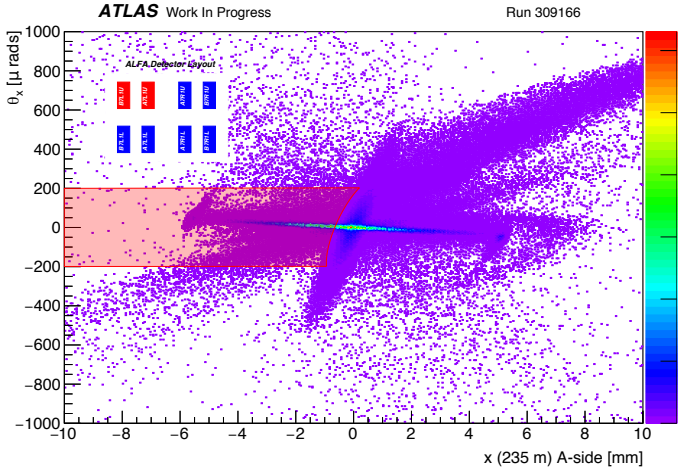

Figure 87: RUC sample with RUC scaling region (w. MBTS veto) overlaid in red.

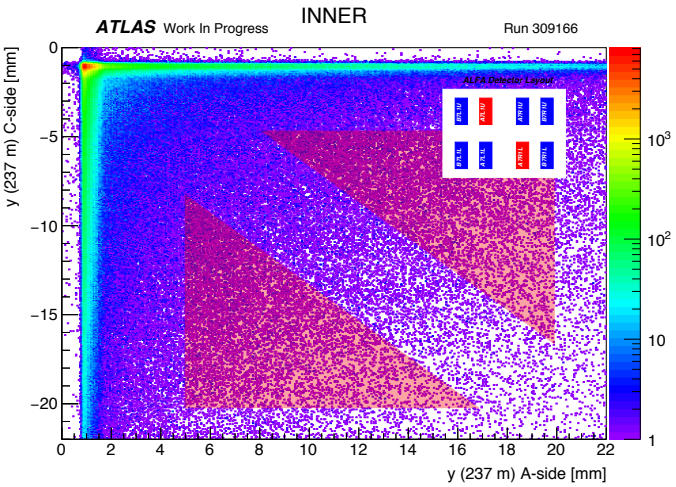

Figure 88: RUC sample with DPE scaling region (w. MBTS veto) overlaid in red.

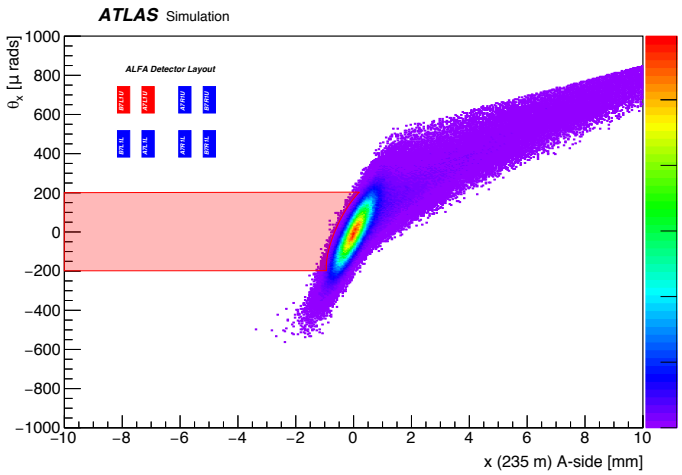

Figure 89: DPE simulation with RUC scaling region overlaid in red.

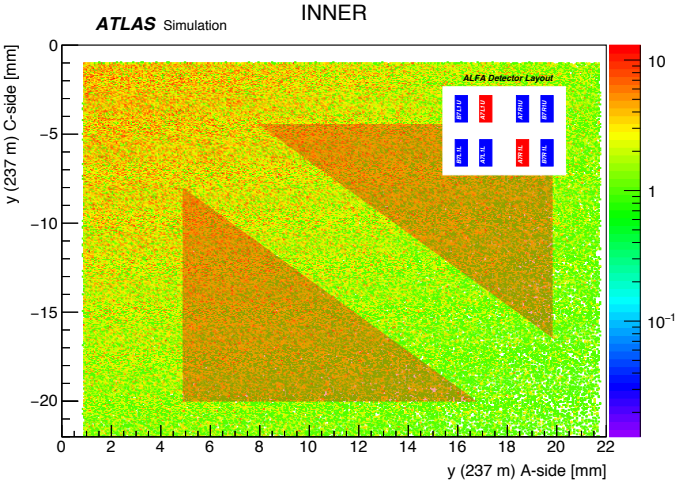

Figure 90: DPE simulation with DPE scaling region overlaid in red.

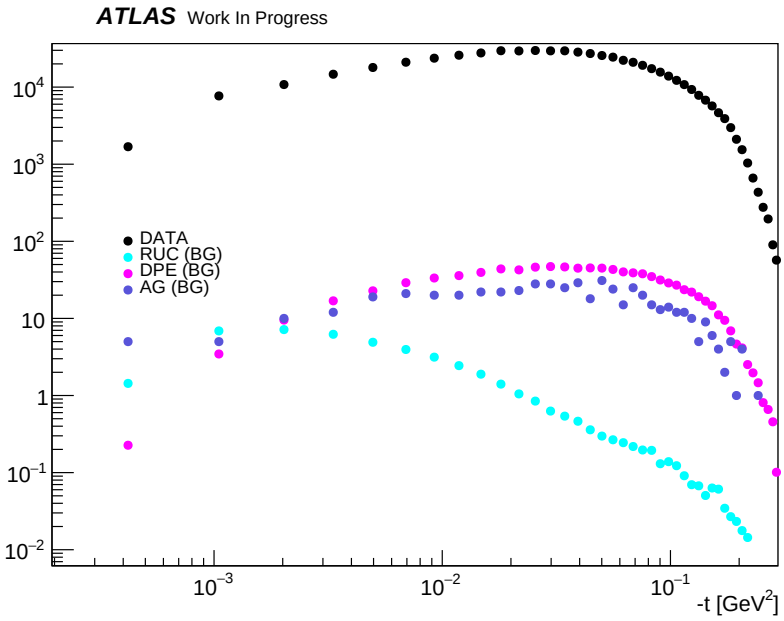

Figure 91: The final scaled RUC and DPE background contributions compared to data. The antigolden sample has been included for reference.

5.10 Trigger Efficiency

The trigger efficiency describes the performance of the trigger in detecting an elastic event. This is an important aspect of the analysis as it is paramount that the triggers recorded from the ALFA detector may be trusted to be valid, or that an an elastic event recorded by the trigger corresponds to an elastic event in reality.

A brief analysis of a sample of the data from *Run 213268* has been included in this thesis. This dataset was chosen as it was necessary to calculate the trigger efficiencies as part of a related $\beta^* = 1$ km analysis. It was included in this thesis as the trigger efficiency is essentially a detector property that is invariant to the run.

The trigger efficiency may also indicate problems with the detector hardware. For example, it is very likely that the electronics of the trigger will suffer radiation damage from the high energy protons of the LHC beam over the course of the detector lifetime, which is likely to reduce the effectiveness of the transmission and processing of signals within the trigger electronics. Hence, the trigger efficiency is an important measurement to argue that the results obtained from each of the detectors are reliable. The trigger efficiency may be measured by comparing the number of events that fulfill the criteria for an elastic event to whether or not a trigger fired in a number of ways.

5.10.1 Wrong Bunch Crossings

The first method is to cross-check the events that pass the elastic cuts with the ALFA trigger bit information, or that the trigger corresponded with the bunch crossing of the concurrent tracked proton in ATLAS. If the event was measured to pass the elastic criteria but not in the correct bunch crossing (BC), then the trigger must be undergoing fluctuations known as *jitter*. There is also a possibility of the trigger completely missing an elastic event, where a trigger tile did not register a hit. Both of these occurrences contribute to reductions in trigger efficiency. In this case, the trigger efficiency measures the number of elastic events that that passed the elastic cuts in the correct bunch crossing compared to the total number that passed the cuts.

The trigger efficiency in this case is given as:

$$\varepsilon = \frac{N_{\text{elastic events with correct triggering}}}{N_{\text{Elastic Events}}} \tag{77}$$

As previously mentioned, there are two trigger tiles that require a simultaneous signal to send a trigger signal to the CTP. It is also useful to measure the disparity between whether both or either triggers fired during an elastic event. When both trigger tiles were recorded as having fired, it is referred to as 'AND' logic, whereas the case that either trigger tile fires is referred to as 'OR' logic.

5.10.2 CTP Triggers

The trigger efficiency of events that were recorded to have a trigger in the CTP may also be examined. As mentioned previously, the loosest trigger, defined by the instance where either one of the two pairs of trigger tiles of the detector fire, is applied. There is an individual trigger for each detector, as well as the elastic triggers shown in Table 2. The efficiency of these may be measured by comparing whether there was a trigger recorded for an event that passes the elastic criteria.

The trigger efficiency in this case is defined as

$$\varepsilon = \frac{N_{\text{elastic events with correct single detector CTP item}}}{N_{\text{Elastic Events}}} \tag{78}$$

5.10.3 Discussion of Trigger Efficiencies

The trigger efficiencies for each detector and the individual elastic trigger are shown in Table 9. Statistical errors were calculated using the error on a binomially distributed observation, while the quoted systematic errors were calculated by finding the difference between the efficiency with all cuts and the efficiencies with one cut removed for each criterion, whereby the differences between the full and partial elastic efficiencies are then added in quadrature.

Several important results may be observed in this analysis. An important point to note in regards to Table 9 is that, while the trigger efficiency of the overall detector remains above 98% overall, the efficiency for Detector B7L1U is significantly lower than for the others in the case of triggers firing in the wrong bunch crossing. This is not so, however, in the case of the CTP trigger items. This suggests there is some problem with this detector.

An examination of the different logics used by the detector in Figure 94 reveals there are significantly more events that passed the criteria yet did not fire at all in the AND logic, where both trigger tiles fired, than the OR logic, where either of the trigger tiles fired, in B7L1U. This implies that there are likely problems with the co-incidences with respect to the trigger tiles in this detector. One may also rule out the contribution of geometrical dependencies using Figure 96. Notably, the trigger efficiency is lower near the detector edge due to the region where the trigger tiles do not overlap with the MD.

The proportion of missing triggers in the elastic sample is shown in Figure 95. The instance where there is a wrong trigger in all of the detectors leads to the event not being passed to the CTP. As may be seen, the fraction lost in the calibration stream is of the order 10^{-5} events, or one in ten thousand events.

Secondly, it was noticed during this analysis that there appears to be a slight but non-negligible decrease in the trigger efficiency of the detector throughout the physics running periods. The trigger efficiencies as a function of lumiblock are shown in Figures 92 and 93. This was only true for the trigger firing in the wrong bunch crossing, as there was no clear relationship in the case of CTP trigger item efficiency. This is likely related to the increasing amount of beam halo, since the decrease appears to be reset between scraping periods. Assuming this is true, this could be understood in the following context: as beam halo increases, the probability that two beam halo

WBC	Efficiency %	± Stat. Efficiency %	± Syst. Efficiency %
Detector Arm			
Arm 1	98.492	0.019	0.022
Arm 2	99.554	0.011	0.005
Detector			
Arm 1			
B7L1U	95.241	0.067	0.082
A7L1U	99.916	0.009	0.004
A7R1L	99.778	0.015	0.005
B7R1L	99.033	0.031	0.012
Arm 2			
B7L1L	99.842	0.013	0.058
A7L1L	99.910	0.010	0.002
A7R1U	99.785	0.015	0.004
B7R1U	98.680	0.038	0.013

(a) Trigger efficiencies measured with respect to trigger jitter.

CTP	Efficiency %	± Stat. Efficiency %	± Syst. Efficiency %
Detector Arm			
Arm 1	99.320	0.013	0.050
Arm 2	99.601	0.010	0.022
Detector			
Arm 1			
B7L1U	99.053	0.030	0.033
A7L1U	99.860	0.016	0.084
A7R1L	99.677	0.018	0.068
B7R1L	98.811	0.113	0.042
Arm 2			
B7L1L	99.583	0.021	0.072
A7L1L	99.811	0.014	0.029
A7R1U	99.689	0.018	0.039
B7R1U	99.324	0.027	0.030

(b) Trigger efficiency measured with respect to missing CTP items.

Trigger Item	Efficiency %	Stat. Error %	Syst. Error %
ELAST 11	97.582	± 0.048%	± 0.021%
ELAST 12	98.656	± 0.038%	± 0.016%
ELAST 13	98.583	± 0.037%	± 0.010%
ELAST 14	98.702	± 0.035%	± 0.016%
ELAST 15	99.719	± 0.017%	± 0.008%
ELAST 16	99.120	± 0.031%	± 0.018%
ELAST 17	99.286	± 0.028%	± 0.005%
ELAST 18	99.750	± 0.016%	± 0.008%

(c) The trigger efficiencies for individual CTP trigger items.

Table 9: The calculated trigger efficiencies for *Run 213268*.

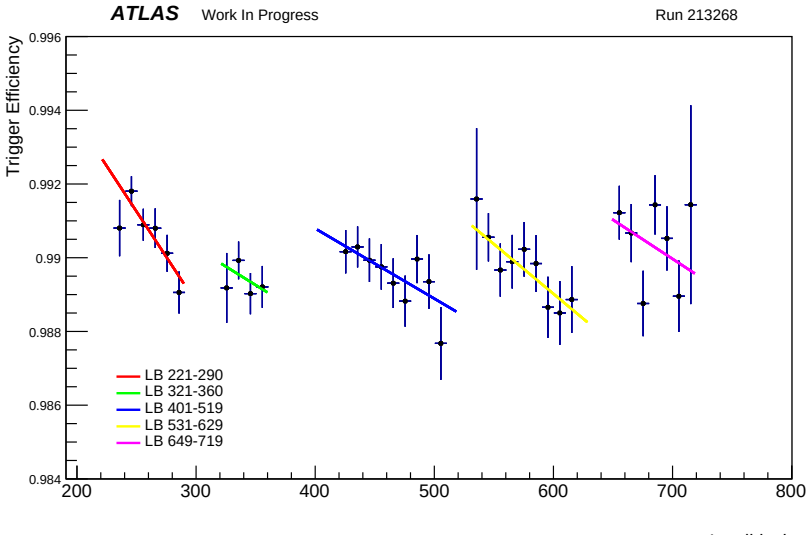

Figure 92: Trigger Efficiency of false CTP triggers w.r.t the lumiblocks taken in this run. Only statistical errors included.

Lumiblock Region	p_0 (%)	p_1(%)	$\frac{\chi^2}{NdF}$
238-290	1.00517 ± 0.004522	-0.000037 ± 0.000018	$\frac{2.9}{3}$
328-361	0.996293 ± 0.010537	-0.000020 ± -0.000031	$\frac{1.3}{2}$
422-508	0.998401 ± 0.004102	-0.000019 ± 0.000009	$\frac{3.9}{7}$
540-621	1.005212 ± 0.006698	-0.000027 ± 0.000012	$\frac{2.2}{6}$
651-715	1.004806 ± 0.013050	-0.000021 ± 0.000019	$\frac{7.7}{4}$

Table 10: Parameters for the fits of the lumiblock regions in Figure 92

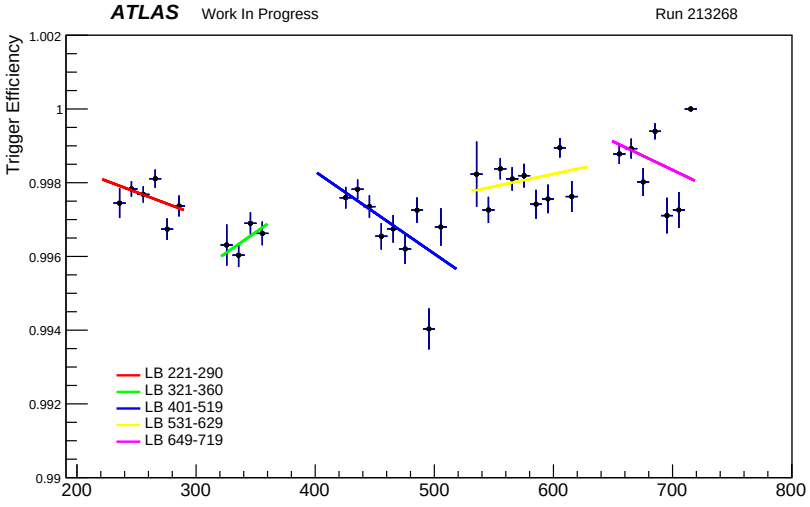

Figure 93: Trigger Efficiency of false CTP triggers w.r.t the lumiblocks taken in this run. Only statistical errors included.

Lumiblock Region	p_0 (%)	p_1(%)	$\frac{\chi^2}{NdF}$
238-290	1.001291 ± 0.002425	-0.000014 ± 0.000009	$\frac{12.3}{3}$
328-360	0.989 ± 0.006148	0.000023 ± 0.000018	$\frac{2.6}{2}$
401-519	1.007225 ± 0.002197	-0.000022 ± 0.000005	$\frac{28.9}{7}$
531-629	0.994151 ± 0.002899	0.000007 ± 0.000005	$\frac{21.6}{6}$
649-719	1.009193 ± 0.005615	-0.000015 ± 0.000008	$\frac{30.86}{4}$

Table 11: Parameters for the fits of the lumiblock regions in Figure 93.

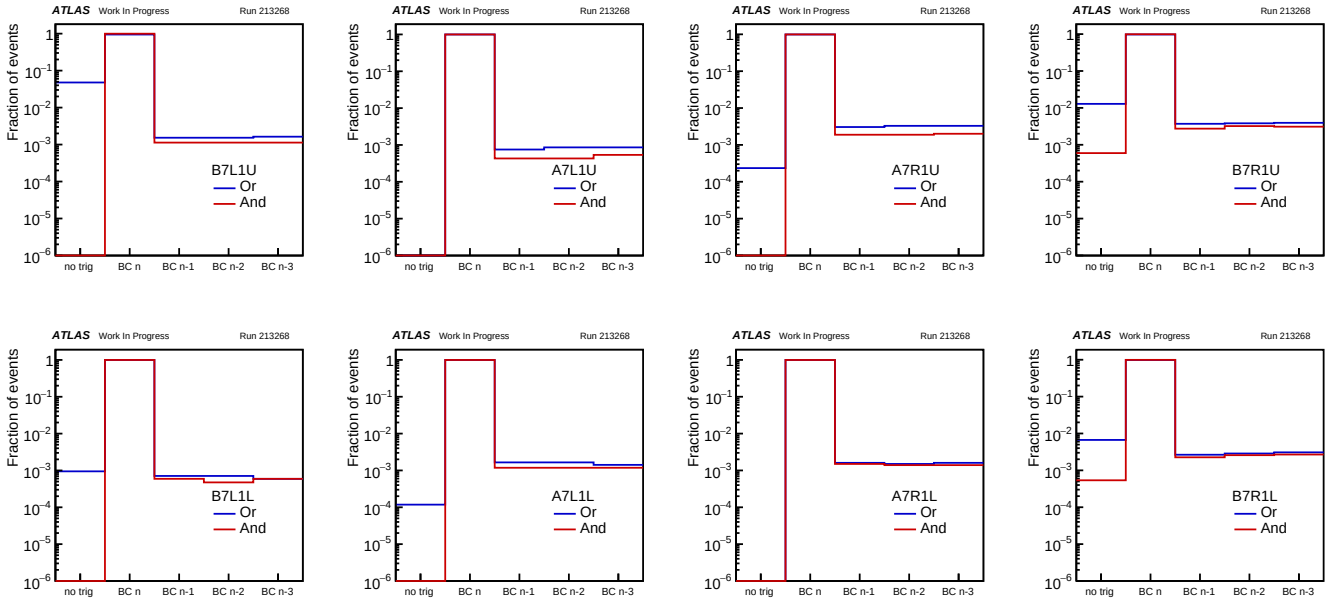

Figure 94: Differences between the types of trigger logic between different recorded bunch crossings.

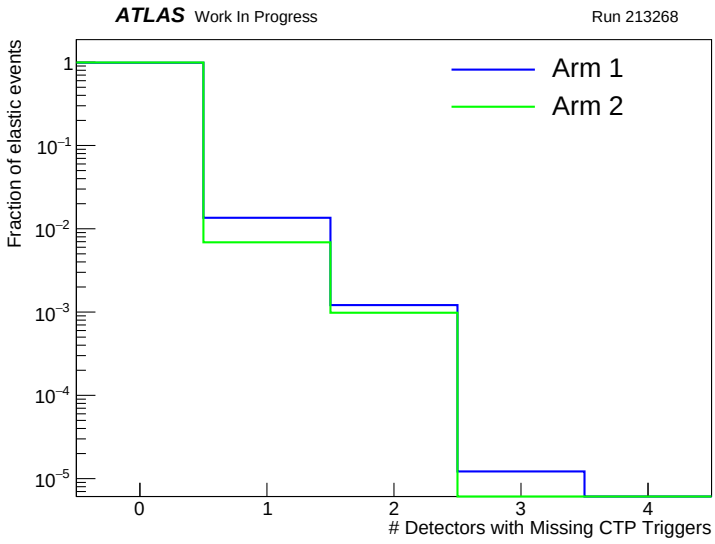

Figure 95: Fraction of events by number of events with missing CTP items in the elastic sample.

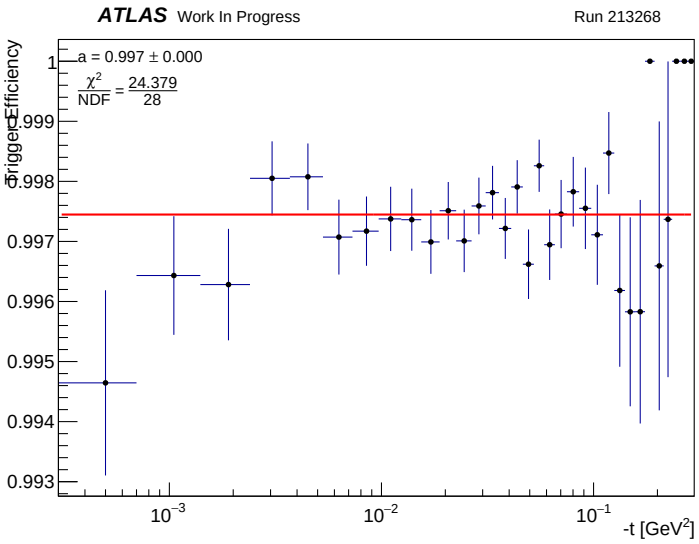

Figure 96: Trigger efficiency across the whole detector as a function of Mandelstam t.

particles trigger the detector increase, since the particles are simply more likely to be uncorrelated as time passes. This theory is in good agreement in what was observed in the case of the track reconstruction efficiencies discussed in Section 5.7.

In conclusion, the trigger efficiency is sufficient for experiments with minor problems in the detector B7L1U. It should be noted that the results provided may have changed in the $\beta^* = 2.5$ km campaign.

5.11 Fiber Efficiency

A brief analysis of the fiber activity was performed as part of this thesis to examine the potential effects of fiber behavior on measurements.

Coincidental fiber activity in each of the layers was measured for the elastic protons. The activity in each of the detectors, measured by a count if the fiber layer in that detector had between 1 and 3 fibers measure a signal during that event, was found. Activity should reflect whether or not a track was reconstructed in the detector: for example, if an event was reconstructed in all of the detectors of Arm 1, activity in the fiber layers of the detectors of Arm 1 should be detected with a rate given by the efficiency of the fiber. At the same time, the activity in the fibers of Arm 2, where a track was not constructed in any of the detectors, should be negligible.

The fiber efficiencies for the active arms are shown in Figures 97 and 98. For most of the detector, there is an average coincidence rate of approximately 90% for the active detector arm during elastic events. However, in detectors A7L1U and A7L1L, a significantly lower coincidence rate is observed for the V fiber layers than for other detectors. This is an unexpected effect, since the U layers in these detectors have approximately the same coincidence rate as those in other detectors. A possible cause for this effect is some form of mis-calibration on the specific fiber PMTs, since this effect primarily occurs for two specific detectors and for the same fiber layers in both. This effect is discussed further in Section 7.3.

Properties of fiber noise were also examined. ATLAS records which fibers which were struck by a proton in each of the U and V layers. As previously mentioned, the position of a proton in one of the ALFA detectors is determined from the mean of the distribution of fiber hits in the detector, under the assumption that the path through the fiber is completely parallel. In reality, there is some negligible angle the proton takes through the detector. In this analysis, it was attempted to quantify and explore this behavior for the ensemble of available elastic data.

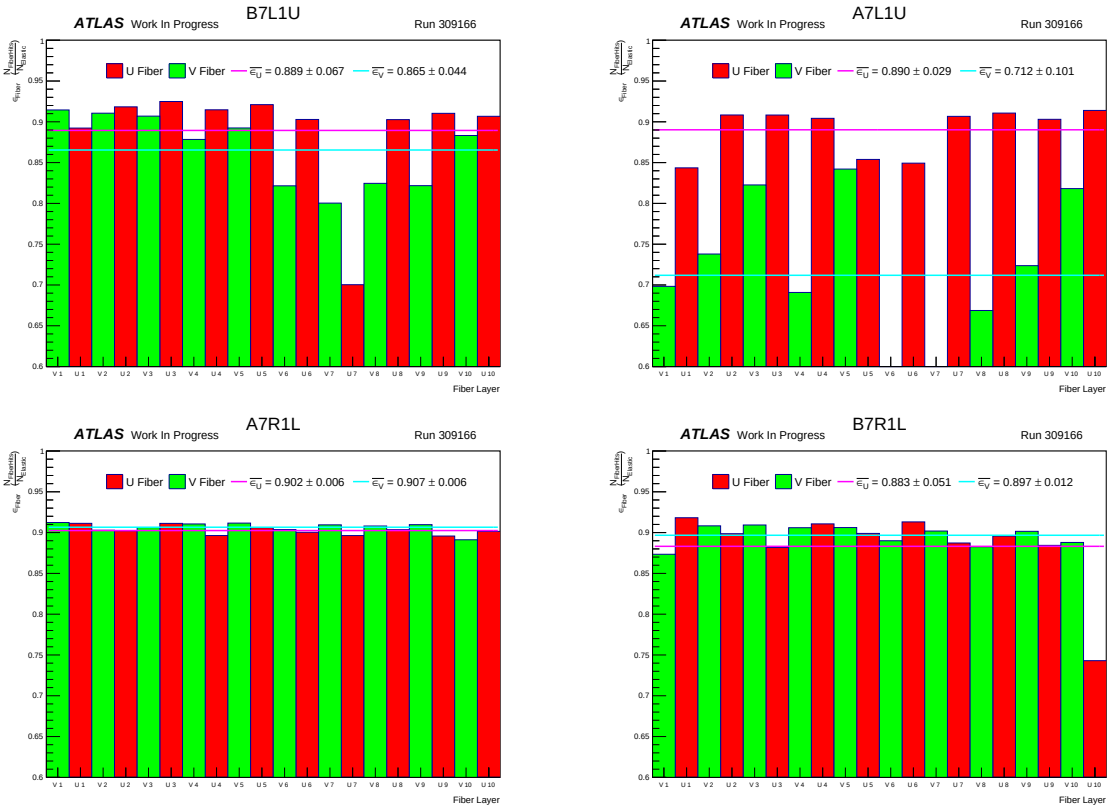

Figure 97: The fiber efficiency for events observed in Arm 1. This is the ratio between the fiber layers which had between 1 and 3 fibers fire during an elastic event and the total elastic events observed in the arm.

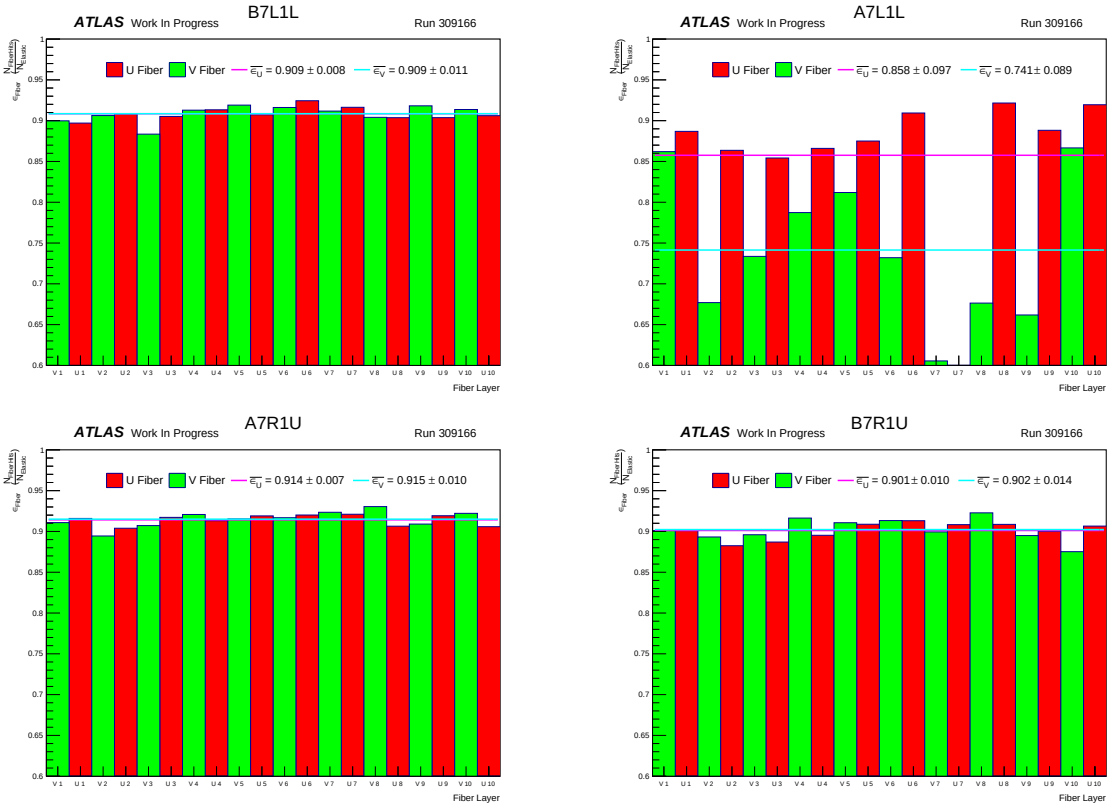

Figure 98: The fiber efficiency for events observed in Arm 2. This is the ratio between the fiber layers which had between 1 and 3 fibers fire during an elastic event and the total elastic events observed in the arm.

In order to so, a plot of the fiber activity versus the layer for each event was made before proceeding to fit a straight line to the result for the U and V layers individually. The slope of this fit provides insight into how the proton's path migrated between fibers as it traversed the U and V layers, while the error on the fit indicates the level of cross-talk and other noise contributing. In summary, one may predict that elastic protons reconstructed with tracks in each detector of an arm ought to exhibit a clear and approximately parallel path of fiber hits through the detector with little cross-talk between fibers.

The observed distributions are shown in Figures 99 and 100. The primary feature to note is that, as predicted and in all U and V fiber layers, the protons exhibit very small angles with little error. Higher values of uncertainty are more probable at larger reconstructed angles.

An observation of note in the is the distributions in the region $-0.2 \leq x < 0.2$ fibers per layer and $0.1 \leq y < 0.2$ fibers per layer. Here, the second largest concentration of events in the distribution may be found, and is approximately symmetric about zero except in the case of of armlets B7L1L - A7L1L and B7R1L - A7R1L for the U fiber layers. Events in this region do not appear to be influenced by the magnitude of the angle, and constitute around one in a thousand events.

Further investigation on an event by event basis revealed that this effect seemed to be correlated with a broader spread of fiber activity in the latter four layers of each detector, which contributed to the error in a way unforeseen by this method of analysis. In order to corroborate this theory, an analysis was performed where the fit was only performed over the first six fiber layers in U and V. The effect was reduced in every case. An example of the result may be found in Figure 101. It should be noted that some events were excluded from the plot due to having insufficient fiber hits to fit a straight line.

Improving the track reconstruction efficiency is always a concern for data analysis, as normal track reconstruction takes into account the entire fiber activity for all the layers. Consequently, including these events may lead to higher uncertainties on the position if the proton and the reconstruction of an elastic track. This effect is notable as it may contribute to the track reconstruction efficiency of the detector.

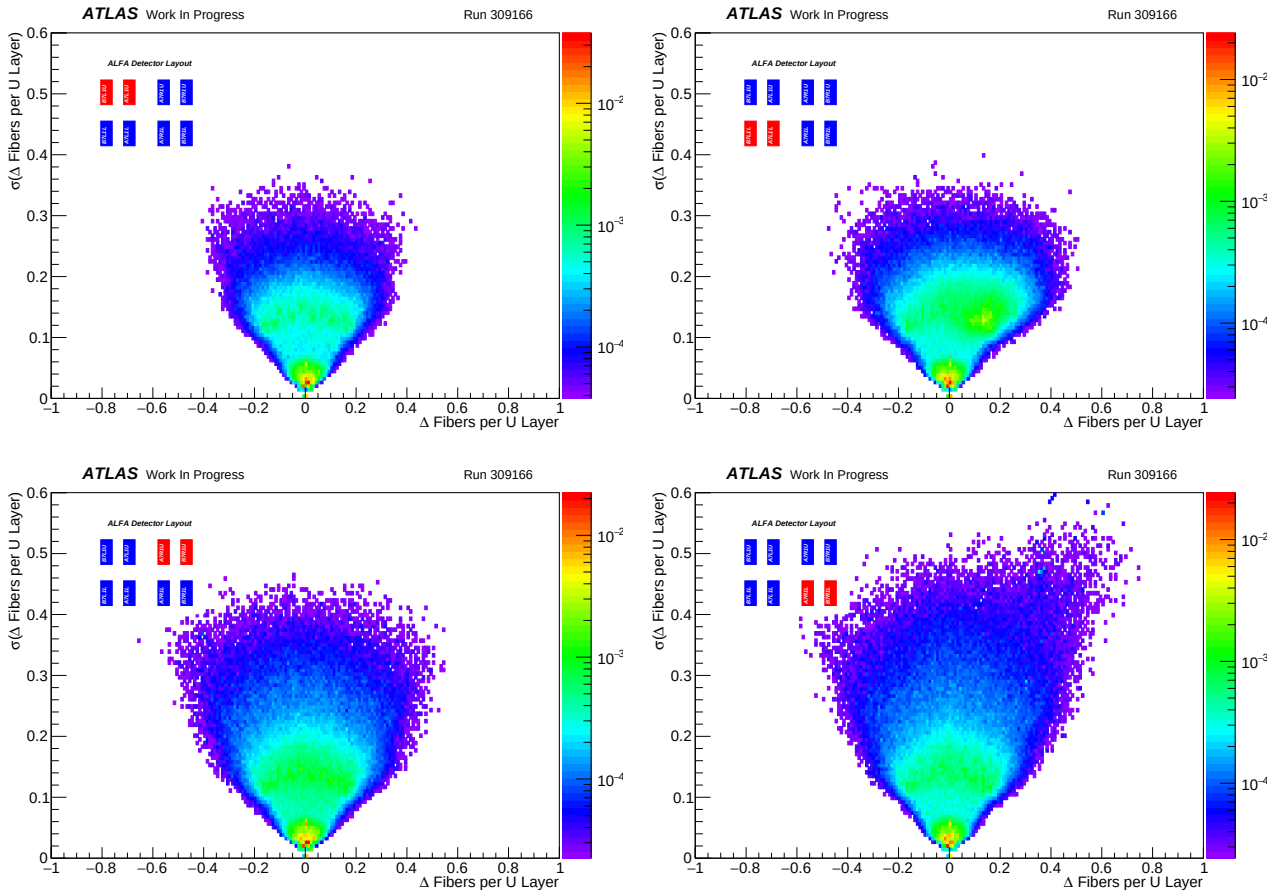

Figure 99: The normalized distribution of the slope (proton angle) and associated errors (noise) on this value for the U Fiber Layers.

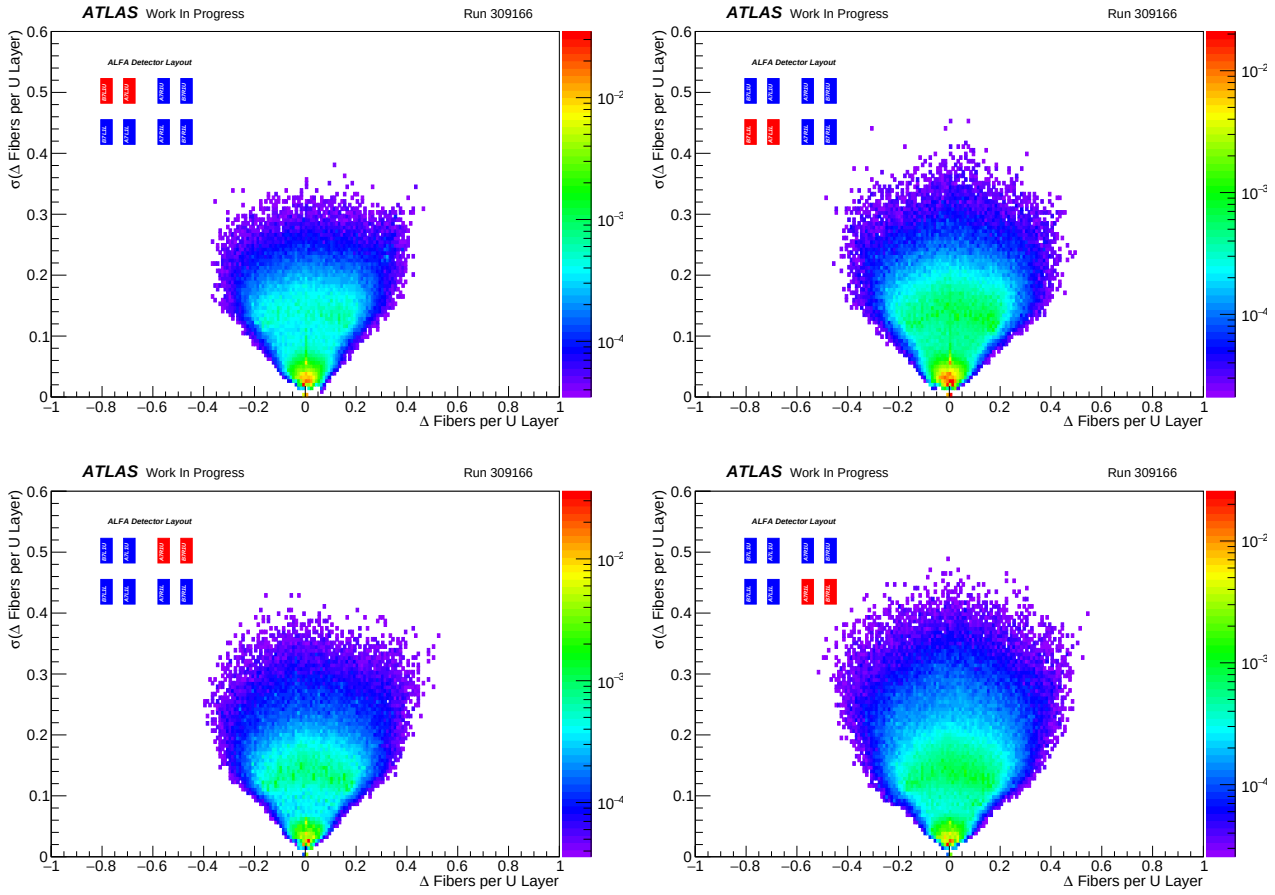

Figure 100: The normalized distribution of the slope (proton angle) and associated errors (noise) on this value for the V Fiber Layers.

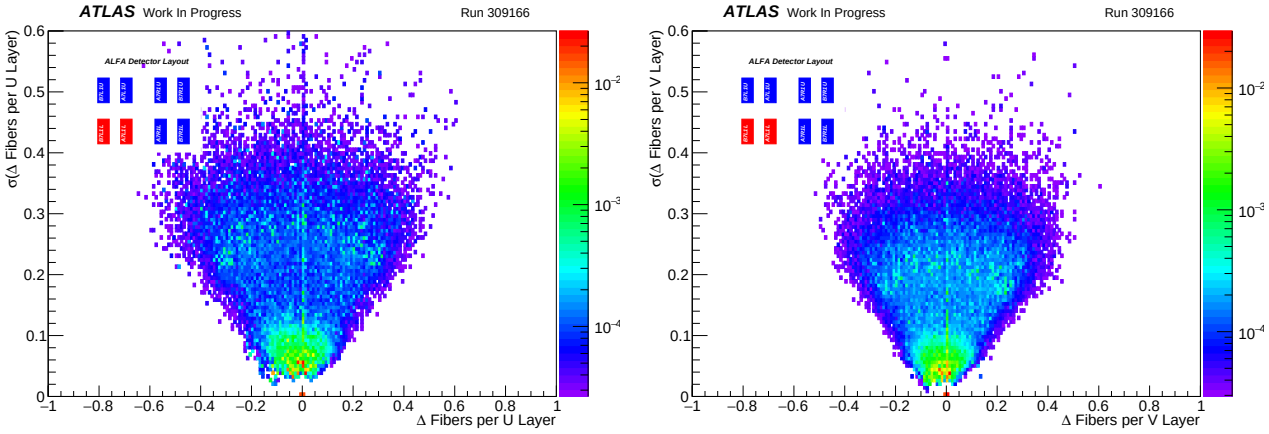

Figure 101: The normalized distribution of the slope (proton angle) and associated errors (noise) on this value for the U Fiber Layers, with a fit range only up to and including the first 6 of the 10 fibers in each layer for armlet B7L1L - A7L1L.

6 Reconstruction of Physics Parameters

The final aspect of the elastic analysis is the reconstruction of the physics parameters of the differential cross section. In this section, the tools to measure the total cross-section, ρ and the parameterization factor, B, using the simulation discussed in Section 5.6 are discussed.

6.1 χ^2 Minimization Method

In this thesis, a recently developed comparison method was applied [4]. This technique involves generating a Monte Carlo simulation of elastically scattered protons at the LHC, transporting these events to ALFA and proceeding to apply all known detector effects to the MC, before using a χ^2 goodness-of-fit test to compare the MC with data. This χ^2 parameter may be minimized with respect to the input physics parameters and contributing nuisance parameters, discussed in Section 6.2, such that the closest available description to data may be found.

The χ^2 function for a set of counts is given to be:

$$\chi^2 = \sum_{i=Arm} \sum_{j=Bin} \frac{(O_{i,j}(t) - E_{i,j}(t))^2}{\sigma^2_{O_{i,j}}(t) + \sigma^2_{E_{i,j}}(t)} + \sum_{k=Pars} \beta_k \tag{79}$$

where $O_{i,j}(t)$ is the measured count of a certain bin, $E_{i,j}(t)$ represents of the Monte Carlo at a certain bin and i and j represent the detector arm and bin respectively. The denominator of this equation represents the errors on the measurement of the bin. Since the measurement is a discrete set of counts, Poisson statistics are used to define the error. This means that, in this case, $\sigma_N = \sqrt{N}$. This method requires a large number of events in the expected count, whereby there would be only be negligible statistical error on this quantity. β refers to penalty terms for the nuisance parameter, k. These are terms used to confine the otherwise free nuisance parameter fits to within the value of the error. In this thesis, The MIGRAD algorithm was chosen to minimize the χ^2 on the measurement [30].

The full χ^2 minimization procedure is described as follows. A single MC sample is generated from the elastic differential cross-section shown in Equation 40c at chosen initial values of the parameters of interest. All cuts and detector criteria are applied to this MC and the distribution of Mandelstam t values is recorded for both detector arms. For each minimization trial, the events from the MC sample are re-weighted bin-wise according to the trial parameters of the minimization program by evaluation of Equation 40c. The MC sample is then normalized to the luminosity and detector efficiencies of the elastic sample in order to obtain the effective event count for this trial to be compared to data sample. The MC sample and data are compared and the minimization procedure continues using the result of the χ^2 from the last trial. The process is repeated until the χ^2 has minimized, yielding parameters of interest that best reflect data.

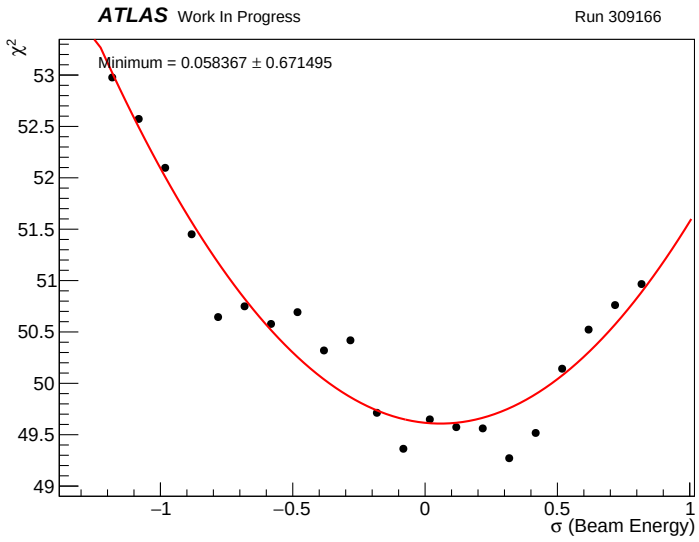

Figure 102: χ^2 plot of scan through the Beam Energy parameter produced with MC containing 2×10^6 events.

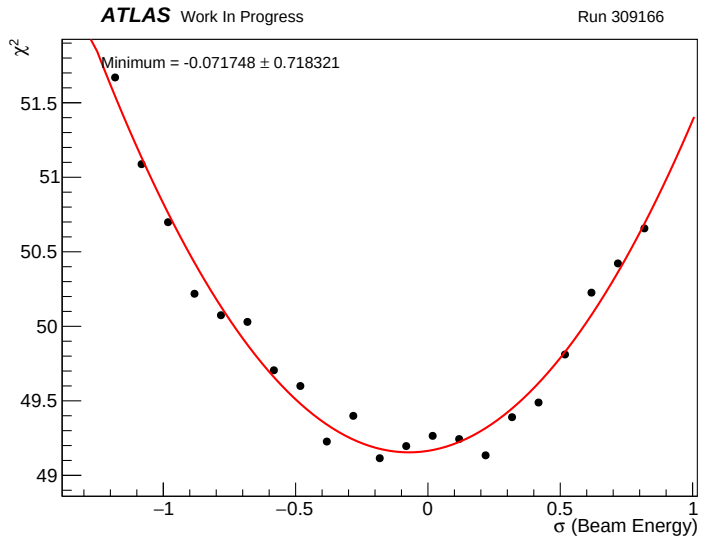

Figure 103: χ^2 plot of scan through the Beam Energy parameter produced with MC containing 2×10^7 events.

6.2 Nuisance Parameter Fitting

Nuisance parameters refer to those parameters that are not the focus of a fit, yet must still be accounted for. The set of nuisance parameters used was dictated by the degrees of freedom within the simulation. The following systematic sources were considered and estimates were made for many of the errors on these variables where a more appropriate one was not available:

- Luminosity:

  The luminosity used in this thesis was calculated using the ATLAS Luminosity Calculator [26]. Using a Good Runs List ($8 < \ell < 107$ and $229 < \ell < 299$, where ℓ is lumiblock) this value was calculated to be 28453.0 mb^{-1}. In previous analyses, the error on the luminosity has been taken to be around 1.5% [4]. This was taken as the error on the luminosity.

- Beam Energy:
  A beam energy of 6.5 TeV (6500 GeV) was taken in order to match the value used in the estimation of the $\beta^* = 2.5$ km optics. According to previous analyses [27], the error on the beam energy is approximately one part per mille, or 0.1 %.

- Beam Emittances:

  The emittances used in this analysis were obtained from the ATLAS eLog [22]. The error on the wire scan measurements have been taken to be approximately 10% in previous analyses [4]. This was increased to 20% due to the significant increase in beamspot size discussed in Section 5.2.

- Detector Alignment:

  As will be proved in this section, the contribution of horizontal and rotational alignments to the error on the cross-section are negligible and the values for the individual vertical alignments may be condensed into two single parameters: a overall distance measurement and an vertical offset. An estimate of an error of 15 μm for the distance and vertical offset was made for both parameters. This was based on the approximate errors on the measurement of the distance by the ODs, which has previously been stated to have an error on the measurement of around 10 μm [3]

- Detector Resolution:
  The error on the detector resolution was taken using the values of the variable resolutions calculated in this thesis, shown in Figure 55. Within this thesis, the statistical error of the overall resolution was observed to be 0.36 μm for data and 0.16 μm for MC. However, it

was decided that, since the differences between the Monte Carlo and data varied outside the statistical uncertainty, to increase the error on the resolution to a conservative 1 μm in order that the two values were closer to being consistent with one another.

- Detector Efficiency (Trigger/Track Reconstruction):
  The systematic error on the track reconstruction efficiency dominates the total convoluted error on the detector efficiency. This value estimated to be 0.2% in accordance with previous analyses [4].

- Background:
  It is unclear as to the magnitude of the error on the background for the reasons discussed in Section 5.9.4. The statistical uncertainty on background was used, though there is likely additional uncertainty on whether the antigolden and RUC backgrounds describe exactly the same phenomena. It should also be noted that, in both cases, the contribution of background to the sample is negligible in any case.

Minimization in the case of nuisance parameters is difficult due to correlations between the various components of the analysis. It is evident in many cases that aspects of the analysis are interrelated in ways that are difficult to determine analytically. A brute force fitting approach is not possible to achieve in a reasonable time period, since *"the technological limitations of Minuit can be seen around a maximum of 15 free parameters at a time"* [31]. Consequently, a method devised in a previous analysis, which balances the measurement with computational difficulty and time constraints [4], was used in order to determine the influence of the nuisance parameters on the χ^2 measurement. This method involved three steps:

- As many parameters as possible that do not require a new simulation, such as the luminosity and detector efficiency that merely scale the proportion of events in the MC, may be minimized directly;

- Upon minimization, all other nuisance parameters are held constant except one. The unfixed variable is scanned over a $\pm 1\sigma$ range and the resulting χ^2 is fitted to a second-degree polynomial. The minimum and error estimate are found from the parameters of the fit. The error on this measurement is taken to be the range over which the χ^2 of the minimum increases by one. For reference, the minimum value of a second-degree polynomial, $y = ax^2 + bx + c$ is $-b/2a$, and the error on this minimum whereby the χ^2 increases by one is $1/\sqrt{a}$.

- The above process continues until none of the nuisance parameters have moved more than 10% of the error in order to ensure the error is consistent. If an individual component satisfies this requirement, it is fixed at its current value.

The nuisance parameter fits performed in this thesis are shown and discussed in Section 7.2 in Table 14.

It should be noted that bin-to-bin migration contributes to the error on the measurement of χ^2 in this method. This effect refers to the fact that, by changing a parameter, events will move between bins and adjusts the shape of the distribution in a way that hinders the minimization procedure due to the fact that derivatives are used to determine consequent trials and further contributes to the statistical uncertainty on the χ^2 measurement.

Several measures have been implemented to reduce this effect. Evidently, one may reduce the effect by reducing the overall proportion of events that lie on the edges of the bin to the overall number within the bin. This is achievable simply by using more statistics. The effect of using more statistics can be seen in Figures 102 and 103, where the variations in the points over the scan can be clearly seen to reduce with more events used. A further method applied ensures that the sizes of the bins are chosen such that at least fifty percent of the reconstructed Mandelstam t values from the transported co-ordinates are within the same bin as the true Mandelstam t values produced directly by the MC. This is achieved by constructing a finely binned histogram to compare these two variables. The bin sizes are found in this manner by iterating through this histogram to find the point at which this condition is satisfied. At this point, at least half of the events lie within the main bin and at most half lie outside. This is in order to capture as many of the events as possible within the appropriate bin. The results of this are shown in Figure 104.

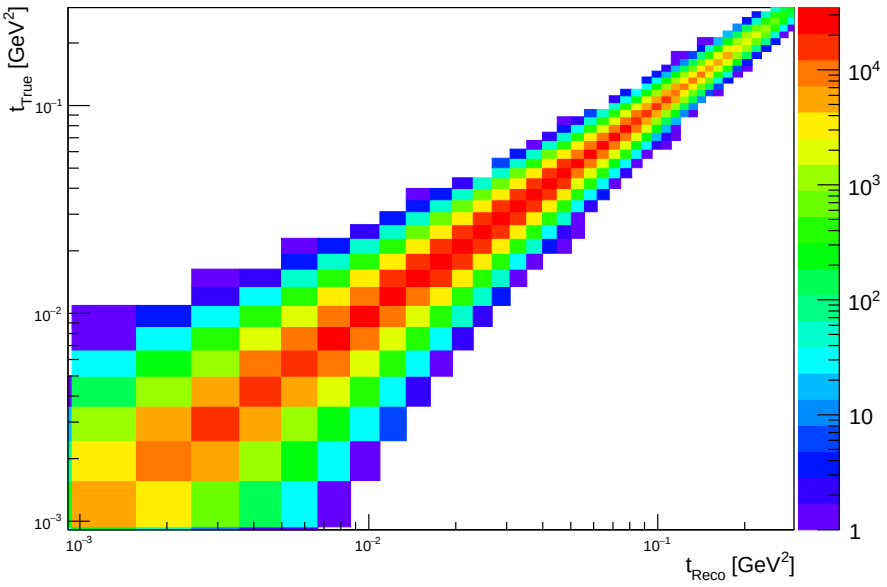

Figure 104: t_{recon} vs. t_{true}, using binning whereby approximately fifty percent of the t_{recon} and t_{true} are found within the same bin.

6.2.1 Optimization

As previously mentioned, there are a great many degrees of freedom within the data such that a direct fit cannot be achieved. To this end, however, many of these degrees of freedom may be removed, either by assessment of the contribution of nuisance parameters to the measured physics parameters or by a principle component analysis of the available covariances. It is possible that there are even more ways to reduce the degrees of freedom and it is hoped that this is achieved in future analyses.

6.2.1.1 Horizontal and Rotational Offset Nuisance Parameters

It was noted that a large proportion of the contributing nuisance parameters, specifically those pertaining to the horizontal and rotational alignment, had a negligible effect upon the measurement of the physics parameters of interest. This observation was examined by randomly assigning the values of these nuisance parameters a value from a Gaussian distribution with a mean of zero and a width of $\pm 1\sigma$ of the error on the horizontal and rotational offsets, which were estimated to be 15 μm and 1 μrads respectively. While holding all other variables constant, the main physics parameters were minimized using these values and the result was recorded.

The results, shown in Figure 105, imply that the distribution of values about the mean of the cross-section is significantly smaller than the statistical uncertainty of the cross-section results shown in Table 13. This suggests that these nuisance parameters may be removed as they contribute degrees of freedom which cannot be resolved from the statistical uncertainty on the measurement. In doing so, the sixteen free parameters pertaining to the horizontal and rotational alignment of the detector may be removed.

This effect may be intuitively understood to arise from the following observations. Horizontal misalignment of the detector causes negligible losses of elastic events since the elastic region is well confined within the horizontal range of the detector. Rotational misalignment is intrinsically slight and increases in relevance the further the event is observed from the axis of rotation. Since elastic events lose no momentum and scatter without energy loss, they are observed to be concentrated about central region of the detector and therefore the vast majority of the data sample remains unaffected by small rotations.

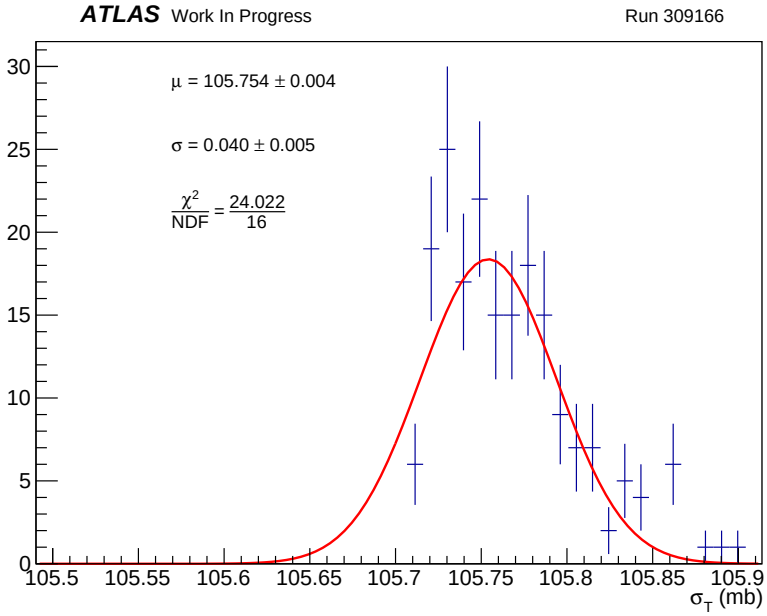

Figure 105: Distribution of fitted σ_T parameters from 200 simulations with randomly assigned horizontal and rotational alignments in the range $\pm 1\sigma$.

6.2.1.2 Vertical Offset Nuisance Parameters

As discussed in Section 5.4, the vertical alignment between detectors consists of a multivariate fit which produces both the vertical offsets and the covariance matrix shown in Table 4. This information is useful as it allows for Principle Component Analysis (PCA). PCA is a process by which the the underlying structure of a multivariate dataset may be found. The parameter space of the covariance matrix of a dataset may be decomposed in such a way that the principle components may be found. Each principle component is a vector which describes the transformation of the covariance matrix to a basis where there is most variation in data. Principle components may be found by calculating the eigenvalues and eigenvectors of the aforementioned covariance matrix. The eigenvalues observed express the magnitude of the principle component and therefore the level of variation, while the eigenvectors describe the variables that vary the most relative to one another.

A PCA was performed on the vertical alignment covariance matrix. The results are shown in Figures 106, 107 and 108. Figure 106 shows that, of the eigenvalues, only two are significant. The corresponding eigenvectors are shown in Figures 107 and 108.

It is clear that the eigenvector shown in Figure 107 only points in the direction of the vertical offsets for all four stations, while that shown in Figure 108 only points in the direction of the distances. This result may be interpreted to mean that the eight free parameters may be condensed into two: an overall distance and an overall vertical offset. This process has removed six unnecessary degrees of freedom from the fit.

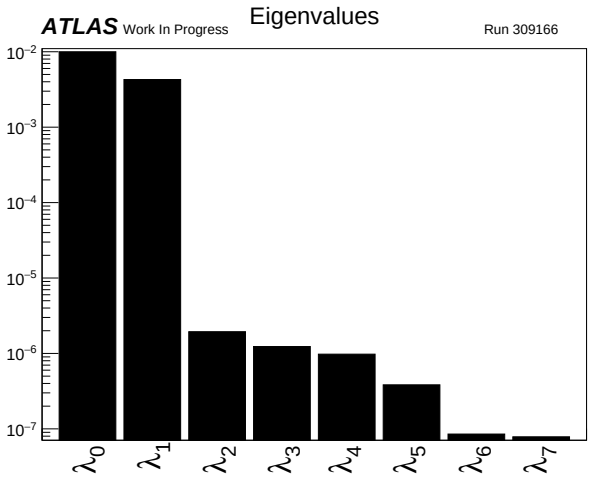

Figure 106: Eigenvalues of vertical alignment covariance matrix. PCA eigenvalues indicate the magnitude of the eigenvector and hence its significance.

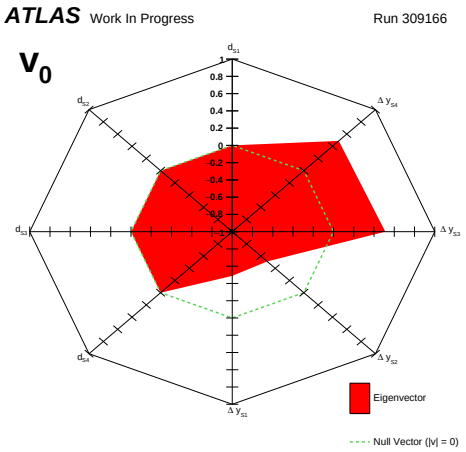

Figure 107: The most significant eigenvector of the vertical alignment covariance matrix. The direction in the parameter space of the PCA is given by the distance of the vector components from the null vector shown.

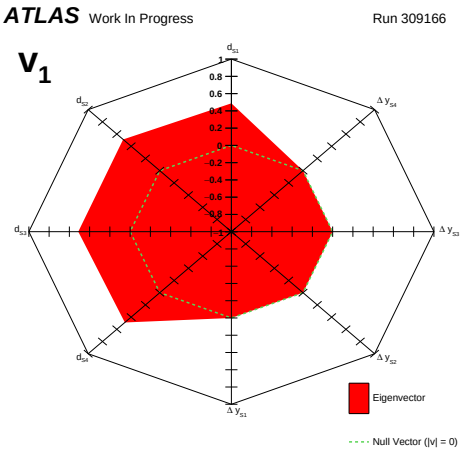

Figure 108: The second-most significant eigenvector of the vertical alignment covariance matrix. The direction in the parameter space of the PCA is given by the distance of the vector components from the null vector shown.

7 Results

In this section, the results of the analysis are discussed.

7.1 Errors

7.1.1 Random Distribution Method

A true measurement of the full systematic error is impossible at time of writing, due to the fact that many of the errors on the nuisance parameters used in this thesis are estimates themselves. Furthermore, a true systematic analysis requires a full fit of all the nuisance parameters, which was unfeasable given limited computation and time restraints. As such, a simplistic analysis was devised such that the composition of the systematic errors and their approximate magnitude may be determined, assuming that the errors chosen were similar to the true errors. An ensemble of 200 simulations of the minimization process for the main observables is performed for random choices from a Gaussian distribution for a related subset of the nuisance parameters, with an error corresponding to the errors discussed in Section 6.2. The other nuisance parameters are held at the fitted values calculated in this thesis. A Gaussian was fitted to the output distribution and the σ value is taken to be the error for the specific parameter or group of parameters. The total systematic error was then calculated by adding the individual components in quadrature.

Nuisance Parameter	$d\sigma_T$(mb)	$d\rho$	dB(GeV^{-2})
Luminosity	0.875	4.16×10^{-3}	7.92×10^{-3}
Beam Energy	0.101	4.38×10^{-4}	4.34×10^{-2}
Efficiencies	0.769	3.97×10^{-3}	9.40×10^{-2}
Background	0.345	1.23×10^{-2}	2.80×10^{-2}
Emittances	0.807	4.89×10^{-3}	6.74×10^{-2}
Alignment	6.04×10^{-2}	5.41×10^{-3}	9.85×10^{-3}
Resolution	3.75×10^{-2}	1.09×10^{-3}	3.10×10^{-3}
Total	1.46	0.016	0.12

Table 12: Systematics calculated for the observables using the random simulation method.

This method does not allow for the subtle interplay between the nuisance parameters to become apparent. However, the contributions are similar in relative magnitude and produce overall values for the systematics that agree approximately with those calculated for previous analyses. With respect to the cross-section, the luminosity, detector efficiencies and emittances contribute most significantly to the systematic error, while the remaining components have little to no effect. These components are also much larger than the statistical error on the value, as the cross-section influences all the bins of the measured distribution and consequently may be measured with much higher precision. For the ρ parameter, the background scaling provided the greatest contribution to error, which is likely due to the due to the bins in the CNI region of the t-spectrum where the effect of ρ may be observed most strongly being more heavily influenced by background. The B parameter is very insensitive to the various nuisance parameters as the B term dominates the structure of the large Mandelstam t, where nuisance parameters have least effect.

7.1.2 Offset Method

A superior method to calculate the overall systematics is the *offset method*. This involves minimizing on the distribution with respect to each of the individual parameters with a nuisance parameter of zero and the extrema, $\pm 1\sigma$. The t-spectrum of the fitted MC is recorded in each case. Then, the difference between the two extreme spectra and the normal spectra, δ_+(i, j) and δ_-(i, j), is found:

$$\delta_{\pm}(i,j) = \frac{dN_{\pm}(i,j)}{dt} - \frac{dN_{nominal}(i,j)}{dt} \tag{80}$$

where i refers to a specific bin and j refers to a specific parameter. While this will result in a distinct positive and negative error, the average value of these spectra is taken to approximate the total error in either direction.

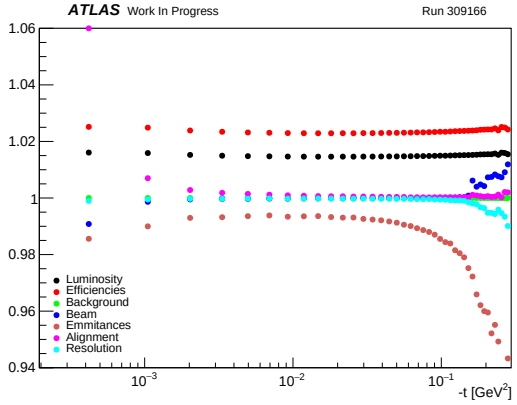

Figure 109: Average factor by which different nuisance parameters change given a $\pm 1\sigma$ variation in the errors for Arm 1.

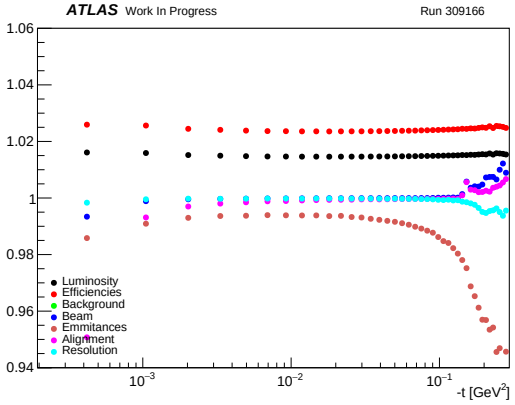

Figure 110: Average factor by which different nuisance parameters change given a $\pm 1\sigma$ variation in the errors for Arm 2.

This difference provides a percentage change as a function of Mandelstam t from the ordinary MC for each contributing parameter. Since this change represents the total difference scaled to 1σ, the individual spectra are scaled to the nuisance parameter for that contributing component, since this is the value to which the error contributes to the fit. The percentage change is then convoluted to form an overall scaling factor for each bin:

$$\delta_{T,Arm}(\mathrm{i}) = \prod_{j=0}^{N_{\mathrm{par}}} \beta_j \delta_{Arm}(i,j) \tag{81}$$

where j refers to the index of the nuisance parameter in question. The factors are then applied for each bin of each arm individually. Since information about the breadth of the nuisance parameters have been included in the fit, the nuisance parameters may vary more widely than previously. The nuisance parameter fits are applied and the systematic errors on the parameters of interest are taken to be the fitting error obtained on these values when the nuisance parameters have minimized.

This method allows for the interplay of the variables to be included in the error, and so this is the technique used in this thesis. The errors calculated in this Section are shown in Table 13.

7.2 Fits

The results of the fitting process and nuisance parameters are shown henceforth. The region $3 \times 10^{-4} < -t < 1 \times 10^{-1}$ GeV^2 was chosen to cover the region of the differential cross-section that is most well described by theory. This region also covers all of the CNI and Coulomb regions allowed by the acceptance of the detector. The MC used 2×10^7 events, around four times the number of events in data. For a stability check, the two time periods of the run used were fitted separately. The fit in these cases were performed using the estimates for the track reconstruction efficiencies for each period, shown in Table 7 and background scaled to the magnitudes observed in the each period in the data sample. Nuisance parameter fits are shown in Table 14. A full scan of χ^2 was also performed through the parameter spaces are shown in Figures 117, 119 and 121. The

projections of the scan are shown in Figures 118, 120 and 122. A incremental scan representative of the full error on the measurement in the parameter space is shown in Figure 123.

Both Arms Fitted	σ_T(mb)	ρ	$B(\mathrm{GeV}^{-2})$	χ^2_{Arm1}/NDF	χ^2_{Arm2}/NDF
Full	105.716	0.119	20.671	29.5/26	41.7/26
± *Statistical*	±0.129	±0.009	±0.062		
± *Systematic*	±1.295	±0.038	±0.066		
$9 < \ell <$107	105.900	0.132	20.673	23.0/26	34.7/26
± *Statistical*	±0.169	±0.012	±0.080		
± *Systematic*	±1.434	±0.059	±0.086		
$229 < \ell <$299	105.280	0.167	20.667	28.4/26	26.3/26
± *Statistical*	±0.222	±0.015	±0.098		
± *Systematic*	±2.007	±0.080	±0.106		
Both Arms Fitted, Background NI					
Full	105.796	0.119	20.663	29.5/26	41.8/26
± *Statistical*	±0.129	±0.009	±0.062		
$9 < \ell <$107	105.993	0.131	20.664	22.1/26	34.4/26
± *Statistical*	±0.169	±0.012	±0.079		
$229 < \ell <$299	105.372	0.166	20.658	28.5/26	26.4/26
± *Statistical*	±0.222	±0.015	±0.098		
Arm 1 Only					
Full	105.519	0.110	20.540	27.2/26	–
± *Statistical*	±0.181	±0.014	±0.087		
$9 < \ell <$107	105.814	0.126	20.611	21.9/26	–
± *Statistical*	±0.236	±0.018	±0.112		
$229 < \ell <$299	105.039	0.151	20.456	26.1/26	–
± *Statistical*	±0.301	±0.022	±0.138		
Arm 2 Only					
Full	105.916	0.128	20.805	–	39.4/26
± *Statistical*	±0.185	±0.013	±0.088		
$9 < \ell <$107	105.989	0.136	20.735	–	34.2/26
± *Statistical*	±0.242	±0.017	±0.113		
$229 < \ell <$299	105.520	0.182	20.883	–	23.9/26
± *Statistical*	±0.328	±0.021	±0.140		

Table 13: The results of the fitting process for different lumiblock regions. The fitting procedure was performed over the region $3 \times 10^{-4} < -t < 1 \times 10^{-1}$ GeV^2 .

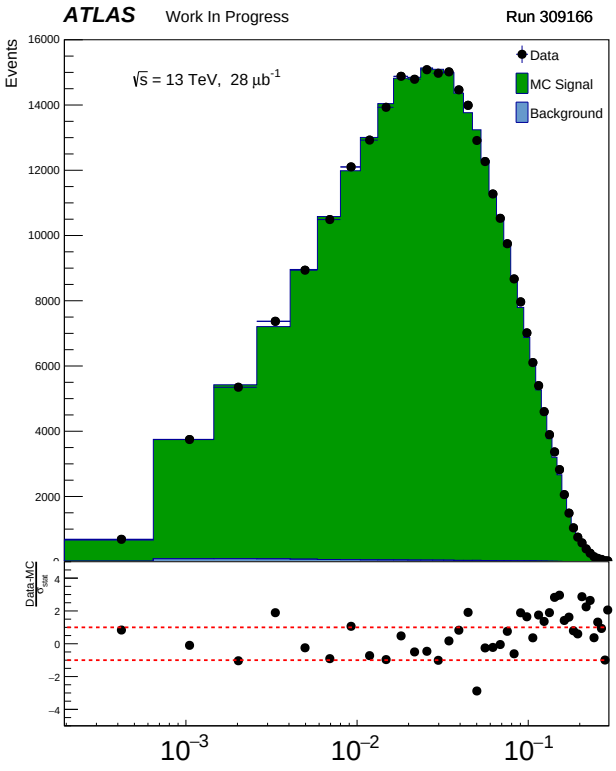

Figure 111: Fit to data over all available data for Arm 1.

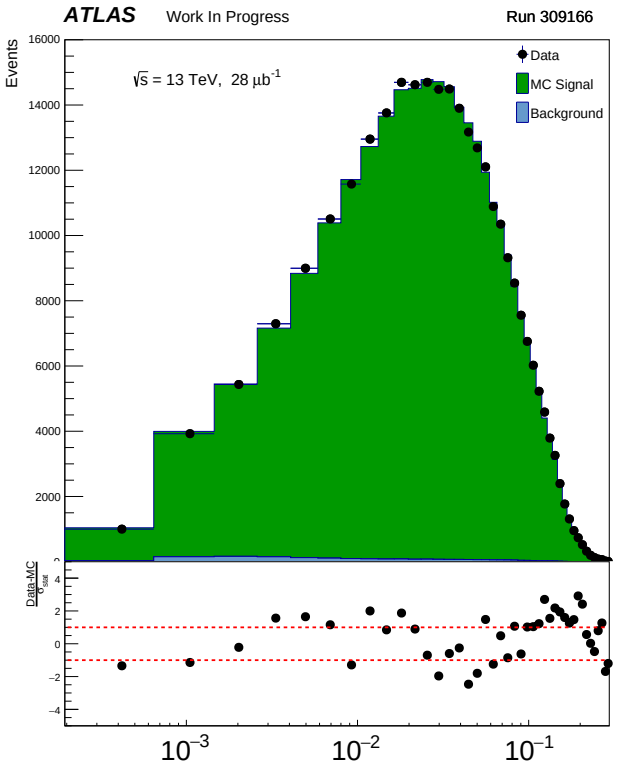

Figure 112: Fit to data over all available data for Arm 2.

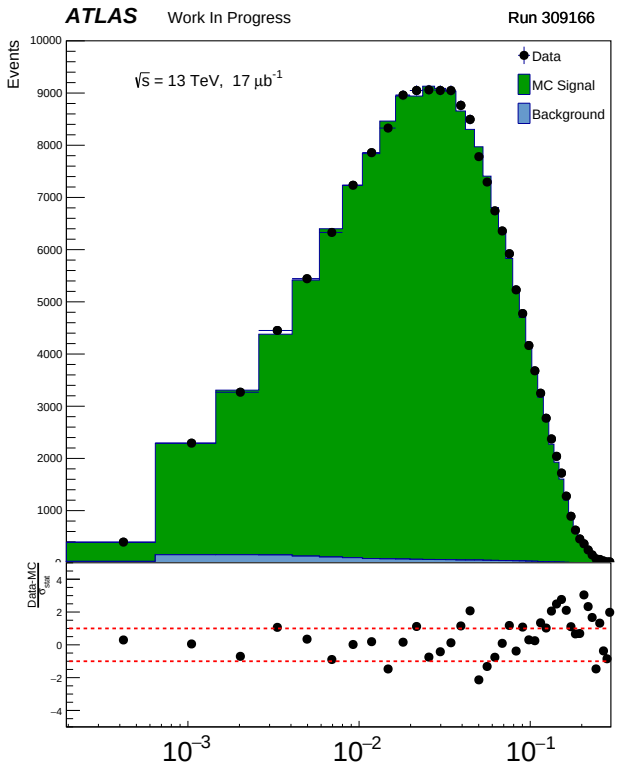

Figure 113: Fit to data of lumiblock region $9 < \ell < 108$ for Arm 1.

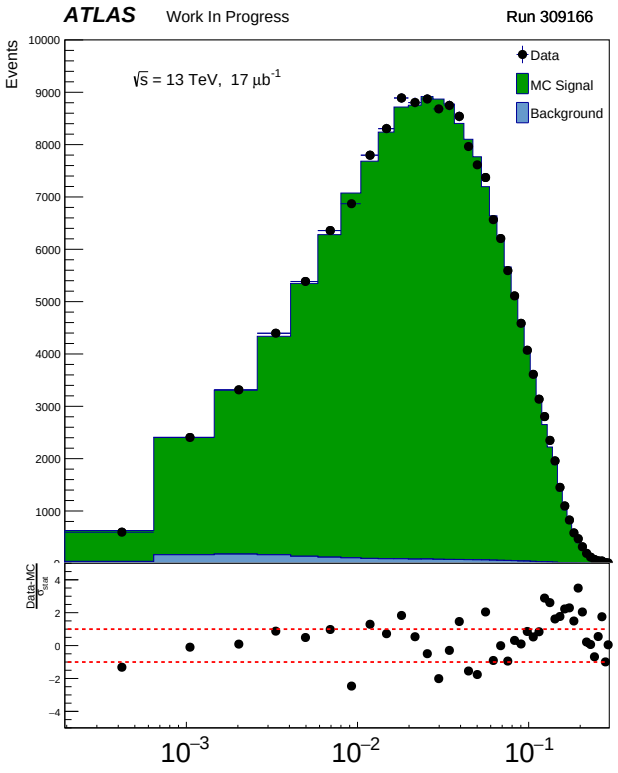

Figure 114: Fit to data of lumiblock region $9 < \ell < 108$ for Arm 2.

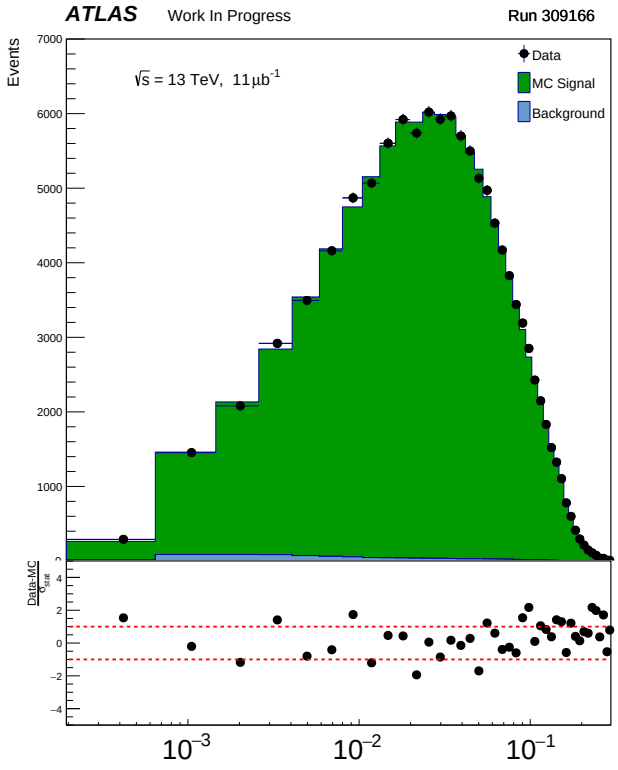

Figure 115: Fit to data of lumiblock region $229 < \ell < 299$ for Arm 1.

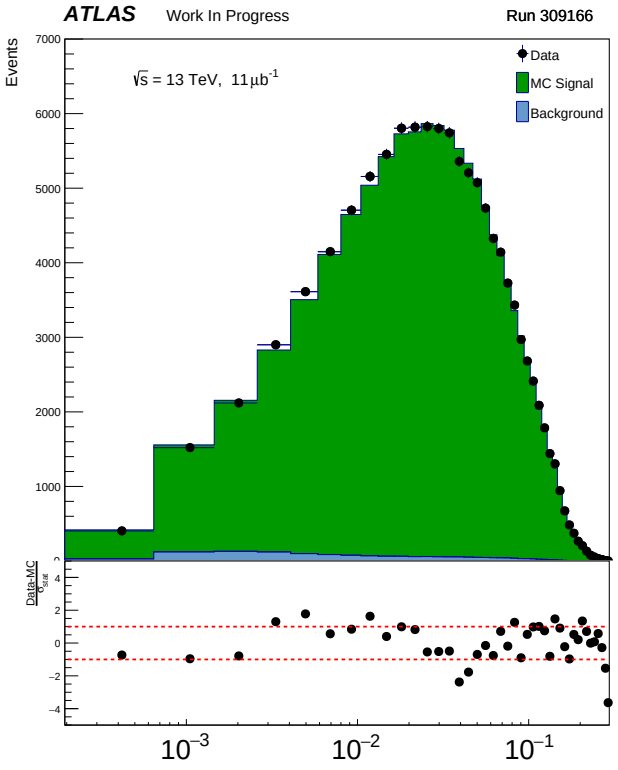

Figure 116: Fit to data of lumiblock region $229 < \ell < 299$ for Arm 2.

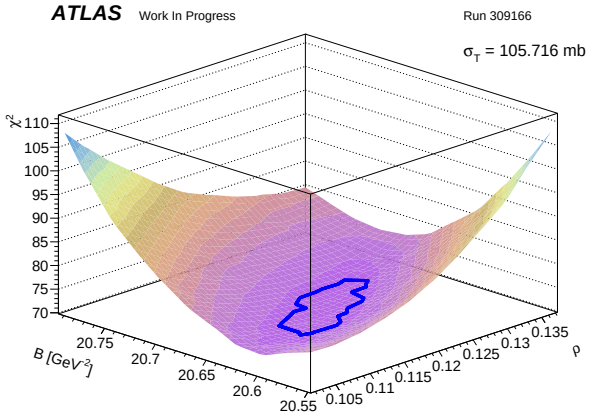

Figure 117: χ^2 scan through $\pm 2\sigma$ (stat.) with fixed value of σ_T. The blue line represents the bounds on the error of the minimum, $\Delta\chi^2 = 1$.

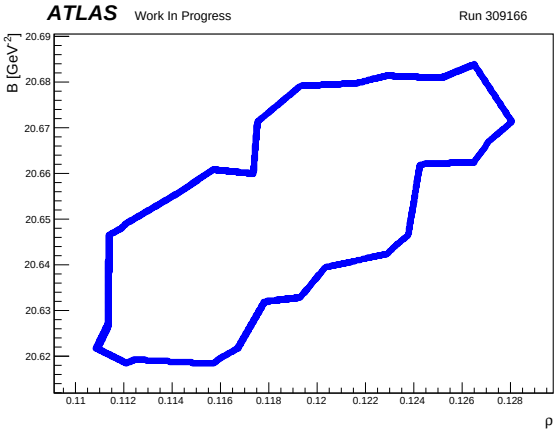

Figure 118: Projection of slice of Figure 117. The blue line represents the bounds on the error of the minimum, $\Delta\chi^2 = 1$.

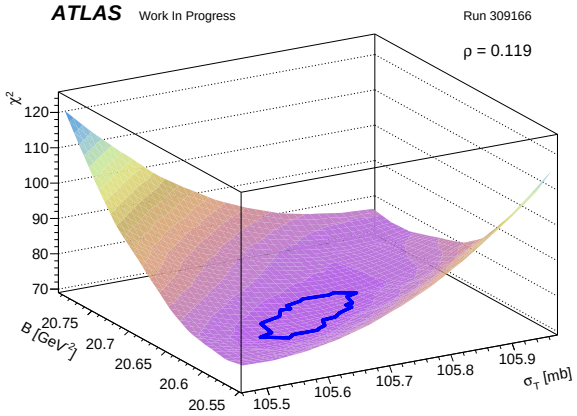

Figure 119: χ^2 scan through $\pm 2\sigma$ (stat.) with fixed value of ρ. The blue line represents the bounds on the error of the minimum, $\Delta\chi^2 = 1$.

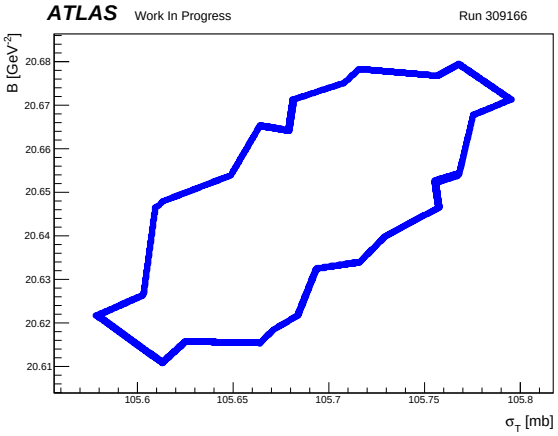

Figure 120: Projection of slice of Figure 119. The blue line represents the bounds on the error of the minimum, $\Delta\chi^2 = 1$.

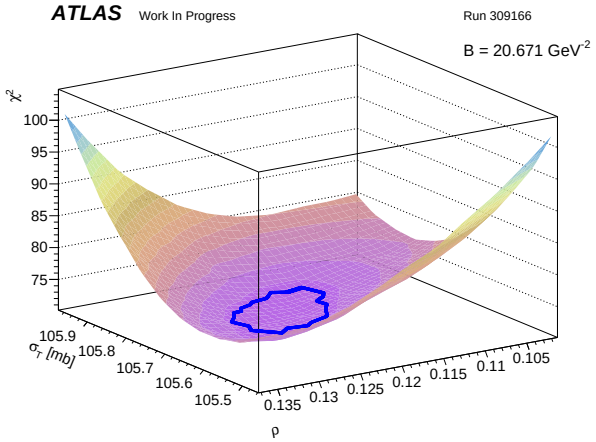

Figure 121: χ^2 scan through $\pm 2\sigma$ (stat.) with fixed value of B. The blue line represents the bounds on the error of the minimum, $\Delta\chi^2 = 1$.

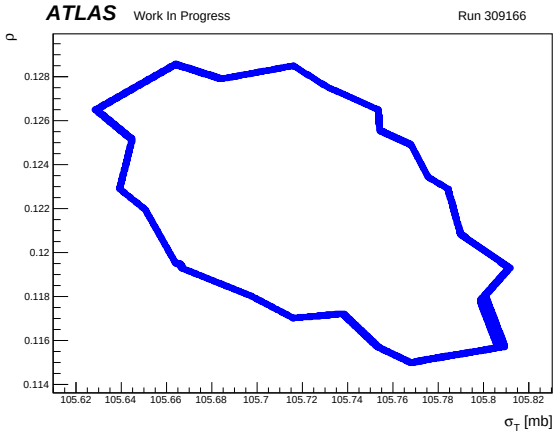

Figure 122: Projection of slice of Figure 121. The blue line represents the bounds on the error of the minimum, $\Delta\chi^2 = 1$.

Parameter	Full		$9 < \ell < 107$		$229 < \ell < 299$	
	Value (σ)	Uncertainty ($d\sigma$)	Value (σ)	Uncertainty ($d\sigma$)	Value (σ)	Uncertainty ($d\sigma$)
Luminosity	-0.600	0.975	-0.276	0.986	-0.194	0.992
Convoluted Efficiency (Arm 1)	-0.351	0.702	-0.479	0.716	-0.266	0.730
Convoluted Efficiency (Arm 2)	-0.609	0.681	0.040	0.687	-0.034	0.696
Background Scaling (Arm 1)	0.464	0.471	0.549	0.434	0.302	0.386
Background Scaling (Arm 2)	1.016	0.779	0.939	0.728	0.683	0.650
Beam Energy	-0.036	0.842	0.350	0.783	-0.204	0.933
Emittance X (Beam 1)	-0.079	0.317	-0.005	0.410	-0.066	0.473
Emittance X (Beam 2)	0.022	0.335	0.050	0.417	-0.009	0.491
Emittance Y (Beam 1)	0.053	0.854	1.421	0.933	-0.811	1.011
Emittance Y (Beam 2)	3.143	0.845	4.605	0.894	-0.251	1.084
Vertical Offset	-0.583	0.589	-0.035	0.688	-0.281	0.684
Distance	-0.024	0.991	-0.091	0.998	0.208	1.000
Resolution (B7L1U - A7L1U)	–0.054	0.986	0.164	0.984	-0.130	1.004
Resolution (B7L1L - A7L1L)	0.154	0.928	0.184	0.943	-0.033	0.990
Resolution (B7R1U - A7R1U)	0.803	1.035	0.520	0.998	0.062	1.010
Resolution (B7R1L - A7R1L)	-0.106	1.034	-0.015	0.972	-0.150	1.062

Table 14: Nuisance parameter fits for each individual luminosity region.

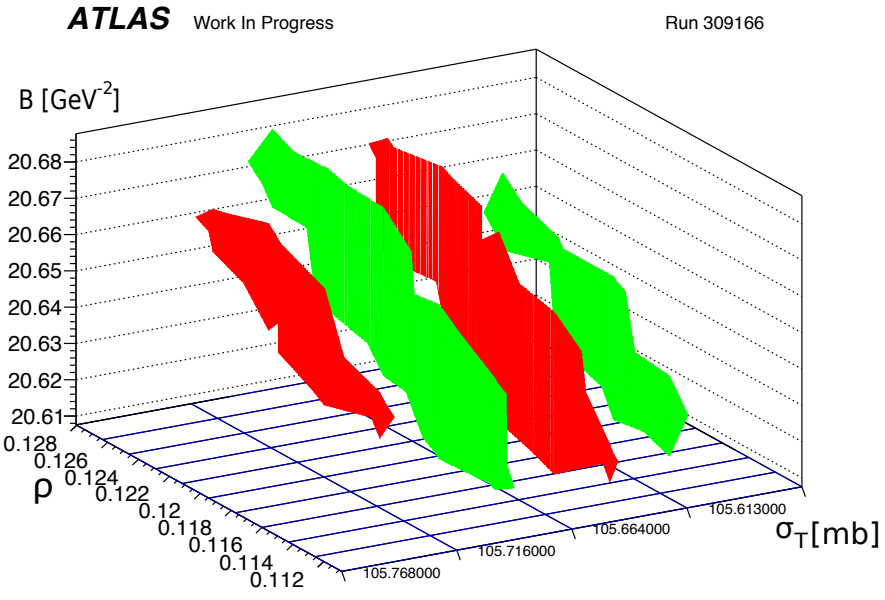

Figure 123: Solutions for $\Delta\chi^2 = 1$ from the true minimum for multiple steps in σ_T. This may be interpreted as a limited estimation of the full error on the χ^2 in the parameter space of σ_T, ρ and B.

7.3 Discussion of Results

7.3.1 Observations

The results of the fitting process shown in Table 13 were poor in the case of the total dataset as indicated by the χ^2 result. To investigate this behavior, it was then decided to isolate different luminosity regions of the run and fit these regions separately, since this should produce a consistent result. A number of observations are discussed henceforth.

The different periods yield very different cross-section and ρ values while maintaining approximately the same overall B value. This could begin to explain the nature of the poor overall fit, as these disparities may have introduced fit tension, whereby the fit minimizes between two or more optima of data subsets and is consequently results in a worse fit than if the fit had been performed on either subset alone. This is particularly important in the case of the ρ parameter, which is sensitive to only a small number of bins. It should be noted, however, that the parameters of interest are consistent within the errors quoted.

The tails outside the fitting region in $8 < \ell < 107$ appear to poorly describe the behavior of the large Mandelstam t values, but this is not the case for the period $229 < \ell < 299$.

The fits using only single arms reveal that the $8 < \ell < 107$ period produces much more consistent values of the cross-section and ρ than the period $229 < \ell < 299$. However, it should again be noted that the values are consistent within quoted errors.

By far the largest contribution to the poor χ^2 fit appears to be the fit to Arm 2 for the period $8 < \ell < 107$. It is clear from Figure 114 that differences may be observed over the entire fitting range. Furthermore, the χ^2 may be seen to be lower in Arm 1 for the period $8 < \ell < 107$ and lower in Arm 2 for the period $229 < \ell < 299$.

The systematic errors are significantly greater for the measurement of $229 < \ell < 299$ than for $8 < \ell < 107$ and the overall fit. This is likely due to having significantly fewer events in the sample. Particularly of note is the large systematic on ρ in all cases, which indicates a high sensitivity of the measurement with respect to the nuisance parameters.

The nuisance parameter fits shown in Table 14 show that the fit for the emittances in the LHC y co-ordinates minimize drastically far from the expected value for the $9 < \ell < 107$ period and the overall fit, but is well within expectations for the period $229 < \ell < 299$.

The inclusion of the scaled background contribution has been shown in Table 13 to be negligible with respect to the fit quality and the parameter values.

It is notable that the scans through the parameter spaces shown in Figures 117, 119 and 121 exhibits a degree of interdependency between the minimized values of B, ρ and σ_T. This suggests that the minimization procedure, in fact, yields a point within the bounds of a volume in the space spanned by the parameters of interest. An estimation of the shape of this volume, projected in slices, is shown in Figure 123.

7.3.2 Commentary

It is, at present, unclear as to why the MC fitting method fails to describe data well. Various attempts were made to try and further understand the observations made.

Differences between arms over time were examined by determining the ratio between the events observed in the arms as a function of the lumiblock. This was performed in order to observe whether or not the the behavior of the number of elastic events in each arm was time dependent. A positive and negative slope was observed in the first and second lumiblock period respectively. Given the parameters predicted by the fit, as shown in Figure 124, the respective probabilities that the $9 < \ell < 107$ period has a positive slope and the $229 < \ell < 299$ period has a negative slope

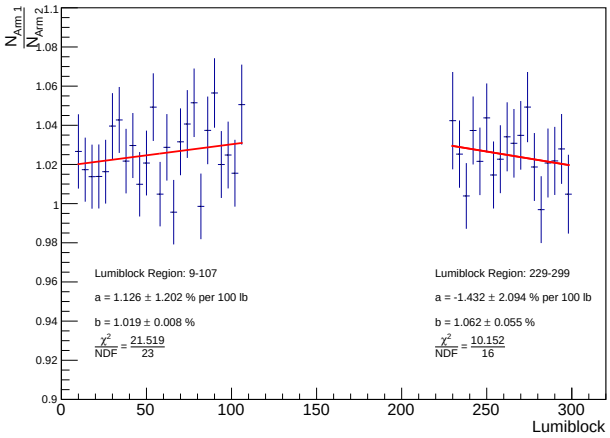

Figure 124: Ratio of number of elastic events in each detector arm as function of lumiblock.

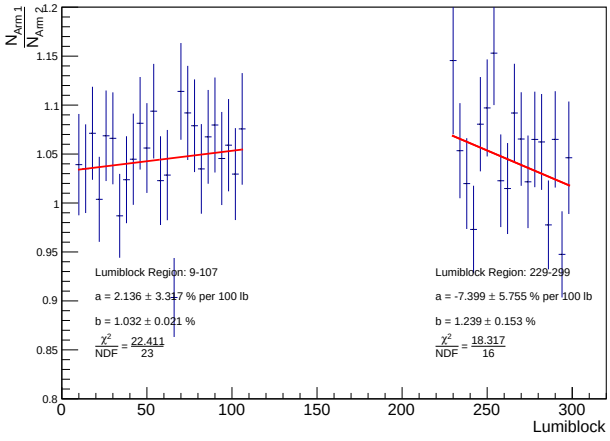

Figure 125: Ratio of number of elastic events in each detector arm as function of lumiblock where $-t \geq 0.1 GeV^2$.

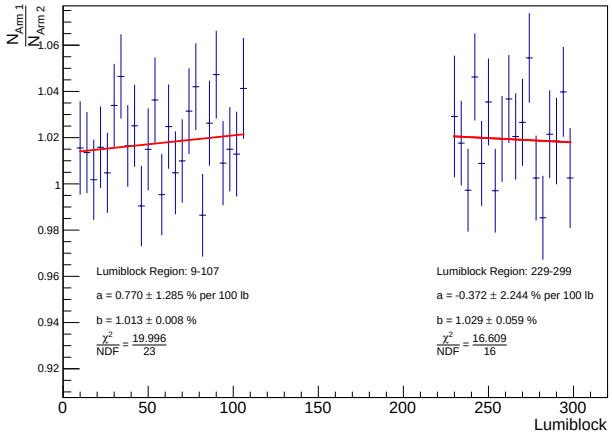

Figure 126: Ratio of number of elastic events in each detector arm as function of lumiblock where $-t \geq 0.1 GeV^2$.

are 82.46% and 75.77% respectively. The probabilities that the slope is greater than ± 0.5 % are 69.88 % and 67.18 % respectively. The effect was found to be of most relevance for large values of Mandelstam t outside the fit range ($-t \geq 0.1$ GeV^2), shown in Figure 125. Specifically in the case of the $229 < \ell < 299$ period, the change in the number of events between arms is consistent with a slope greater than ± 0.5% with a probability of 68.79% and 88.30% respectively. Inside the fit range, as shown in Figure 126, the behavior was consistent with a zero-degree polynomial and so could not explain the differences in fit quality observed between arms. However, the effect may provide some insight as to the poor description of data by MC in the region outside the fit, though it remains unclear as to why the effect would only be observed in one time period and not the other.

The possibility that the geometric cuts were not consistent between data and MC was considered. However, as may be seen in Figures 127 and 128 as well as Figures 129 and 130, the geometric cuts describe the distributions of MC and data similarly at the extreme y co-ordinates in terms of the distribution. The back-to-back elastic cuts shown in Figures 43, 44, 45 and 46 may also be seen to reflect data.

The ratio of the t-spectra of the elastic sample for the two arms was found in order to observe if there was any discrepancy between the distribution observed on a bin-to-bin basis, which is shown in Figure 131. While the tails of the distribution are very different, the main fitting region is consistent with a flat distribution. At the limits of the distribution, these disparities are likely

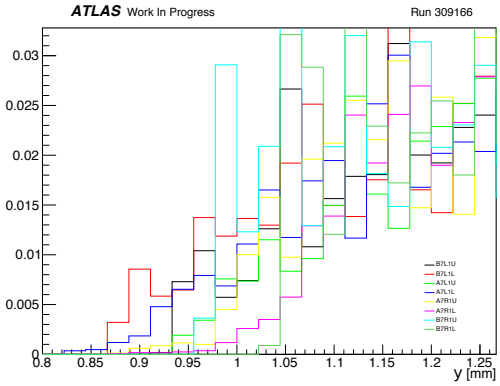

Figure 127: Absolute normalised y distribution of each detector at the detector edge in data.

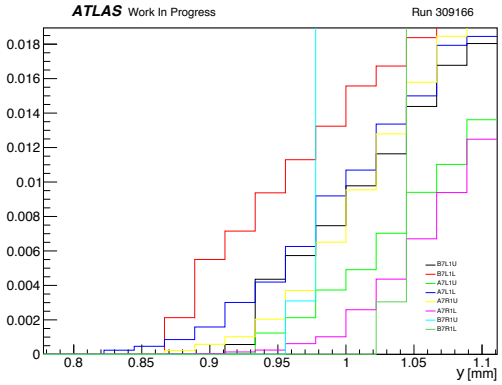

Figure 128: Absolute normalised y distribution of each detector at the detector edge in Monte Carlo.

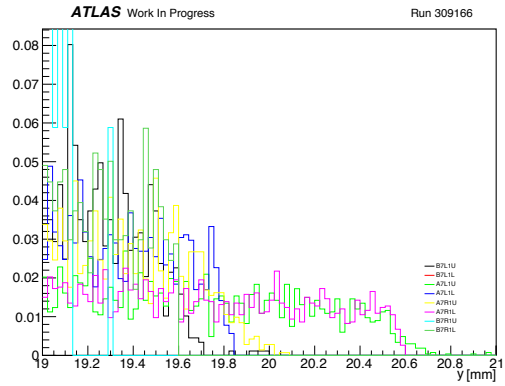

Figure 129: Absolute normalised y distribution of each detector at the beamscreen in data.

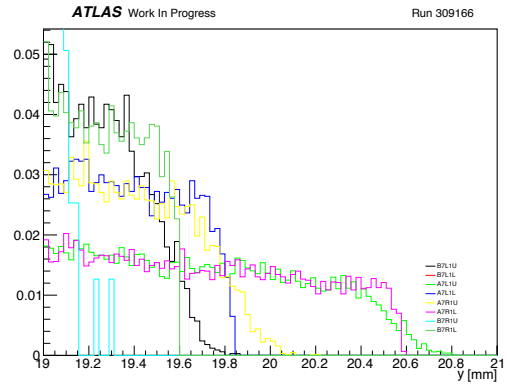

Figure 130: Absolute normalised y distribution of each detector at the beamscreen in Monte Carlo.

due to the individual differences between the edges and beamscreen cuts of each detector. Since the ratios of the track reconstruction efficiencies between arms is approximately unity, one would expect the bin ratios to be one. Within errors, this is what is observed.

It is possible that a time-dependent emittance may have affected the measurement, since the emittance affects many aspects of both simulation and the measured elastic t-spectrum. Therefore, the poor description of the emittance in y observed in the nuisance parameter fits indicates that further investigation is warranted. As may be seen in Equation 50, the emittance is as important to the magnitude of the minimum Mandelstam t values achievable as the β^* parameter. For the sake of simplicity, the emittance was considered a static variable taken in one time period in the simulation used in this analysis, though it is possible that the beam profile evolved in unexpected ways throughout the run. In order to test the hypothesis that the y emittance was time dependent, a measurement of the convoluted divergence over time was made in Figures 51 and 52 and did not indicate any such hypothetical evolution. This, however, only covers the y component of the emittance. The behavior of the beamspot measurement in x shown in Figure 47 suggests a large increase in the x emittance over time. In this case, however, the nuisance parameter for this value appears to be well defined and it is the y emittance nuisance parameters that appear to minimize far from the expected value. This strongly indicates that the assumption of a static emittance does not seem to describe data.

It should also be noted that the track reconstruction efficiency varied significantly between the two periods, as discussed in Section 5.7. This is significant as differences in the track reconstruction efficiency will dictate the overall magnitude of the cross-section. Since the measurement of the parameters of interest are heavily interdependent, it is important that the measurement of the track reconstruction efficiency is valid. The hypothesis that the sample became purer over time, which contributed to the increase in track reconstruction efficiency, was examined by measuring the

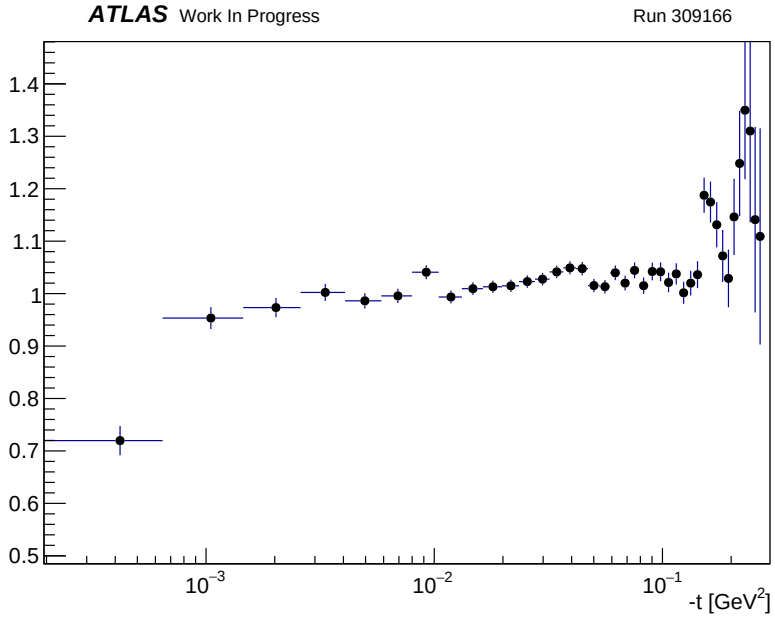

Figure 131: Ratio of Mandelstam t distribution of Arm 1 to Arm 2 of the elastic sample.

change in the total unmatched RUC background sample, where the absolute number of events that pass the elastic criteria in each station of an arm, excluding cuts that require correlations between the sides, were examined as a function of lumiblock. This is shown in Figure 132. It is evident that there is a significantly lower overall magnitude of background in the period $229 < \ell < 299$ than the period $9 < \ell < 107$, which would explain the increase in efficiency. This is likely due to the effect of scraping reducing the overall number of protons in the beam over time, leading to proportionally fewer background events relative to elastics in the sample. The effect must be reflected in the track reconstruction efficiency, since the proportion of background reflects the likelihood of the observation of partially reconstructed tracks. It is notable, however, that the background for Arm 1 did not increase as quickly as for Arm 2 in the period $229 < \ell < 299$. The reasons for this are not immediately apparent. It is also of note that the likelihood of upstream showers appeared to increase over time as shown in Figure 62, which did not seem to be reflected in the track reconstruction efficiency or in a related shower trigger plot, shown in Figure 81. Another important point to note is the contribution of the poor fiber efficiencies observed in Figures 97 and 98 to the track reconstruction efficiency is not necessarily clear. Since this was observed in both arms, the overall effect of this detector problem on the overall track reconstruction efficiency, if any, is currently unknown. An attempt to account for this was made by an examination of the track reconstruction efficiency as a function of the number of fibers used in track reconstruction as shown in Figure 41, but there is no obvious effect that may be observed. This is surprising, as only half of the available fiber layers in A7L1U and A7L1L were measured to be close to design efficiency. Attempts were made to reduce this contribution by only using the outer detectors in the reconstruction of Mandelstam t as mentioned in Section 5.8.1.

There is a possibility of background in the sample that was not accounted for, which would explain the poor fit of the distribution in the Coulomb and CNI regions. This was investigated by measuring the t-spectra of those events which passed all elastic cuts implemented as discussed in Section 5.1 except the *back-to-back* cuts. This would give an indication of the distribution of the background independently of the RUC and antigolden samples. The resulting t-spectra obtained are shown in Figure 133. It is clear to see that there is some level of agreement in the shape of these distributions and the distribution obtained in the background scaling procedure, shown in Figure 91, specifically the DPE contribution. However, at this level, it is not immediately apparent as to whether or not there is any additional background, though it is notable that Figure 133 has significantly larger proportion of events at high values of Mandelstam t than either the scaled RUC or DPE t-spectra.

An attempt to observe the regions where the MC poorly described data was made by subtracting

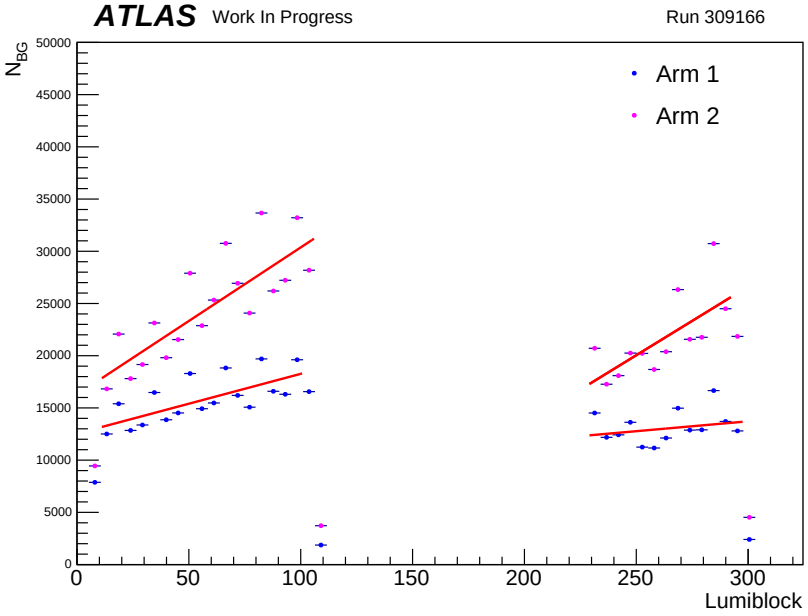

Figure 132: Measurement of the total count of unmatched RUC background as a function of the lumiblock.

Lumiblock Region	p_0 (%)	p_1(%)	$\frac{\chi^2}{NdF}$
$9 < \ell < 107$			
Arm 1	12542.2 ± 68.8801	57.2174 ± 1.15956	$\frac{2426.32}{15}$
Arm 2	16280.6 ± 79.6626	140.889 ± 1.31267	$\frac{5267.25}{16}$
$229 < \ell < 299$			
Arm 1	8046.04 ± 424.925	18.9037 ± 1.61271	$\frac{1876.13}{11}$
Arm 2	-12829.8 ± 604.25	131.503 ± 2.33065	$\frac{3143.71}{10}$

Table 15: Fits to the total unmatched RUC background as a function of the lumiblock.

the sum of the background and fitted MC from the data to observe if any structures were present. This is shown in Figures 134 and 135, where the errors shown are statistical. It is clear to see that the MC is approximately consistent with the fitted result excluding the tails in Arm 1. However, there is clearly disparity between MC and data in Arm 2. As previously mentioned, the MC under-predicts the number of events below a certain value of Mandelstam t and over-predicts the number events at t greater than this value up to the edge of the fitting region. This value is around $-t = 2 \times 10^{-2}$ GeV^2, and, as may be seen from Figure 4, this value is close to the cut-off at which the CNI contribution gives way to the contribution by nuclear interaction. It is possible, in this case, that the MC may have over-estimated the expectation for the number of particles in the CNI region due to a higher-than-expected number of events in the Coulomb region or simply fewer-than-expected events in the CNI region. A possible candidate for this kind of behavior is background at low t-values which has not been included. It is notable, though likely coincidental, that the t-spectrum of the *TIE Fighter* region experienced anomalous results at a similar value as the fitting procedure at around $-t = 4 \times 10^{-2}$ GeV^2. In spite of this analysis, it is not possible to comment with certainty as to whether or not there are any discrepancies, as many of the points shown are consistent with zero within the statistical errors shown.

Particularly worthy of discussion are the parameter space scans shown in Figures 117, 119, 121 and Figure 123. These plots suggests that, in the parameter space, there exists a volume bounded by the error on the χ^2, where each point inside the volume is consistent with the minimized parameters obtained in this analysis with respect to minimization procedure. Specifically, this means that the values and errors on the parameters of interest depend upon those of the others.This is significant, as it implies that a fit of the parameters must take into account the interdependency of the terms when a result is given, as a fit may in fact have several potential minima within the space.

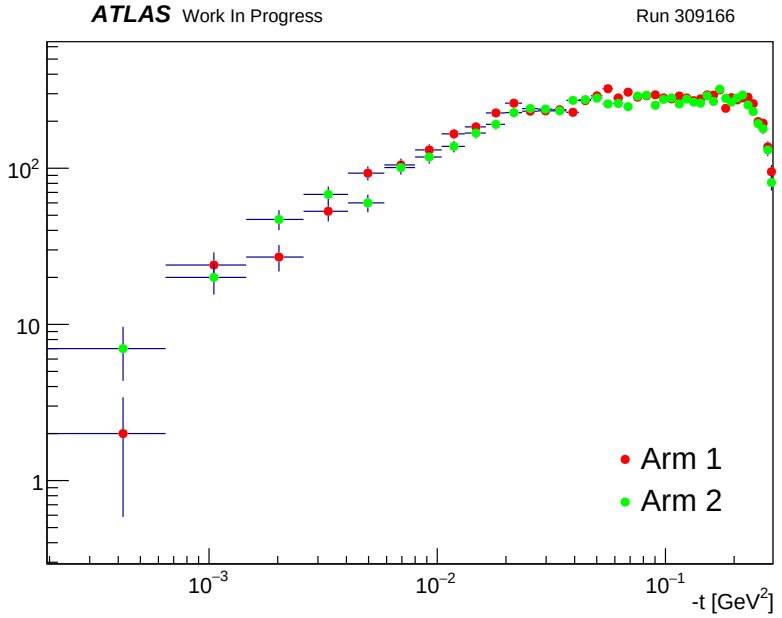

Figure 133: Mandelstram t spectrum of events that passed all cuts but did not pass the *back-to-back* cuts

.

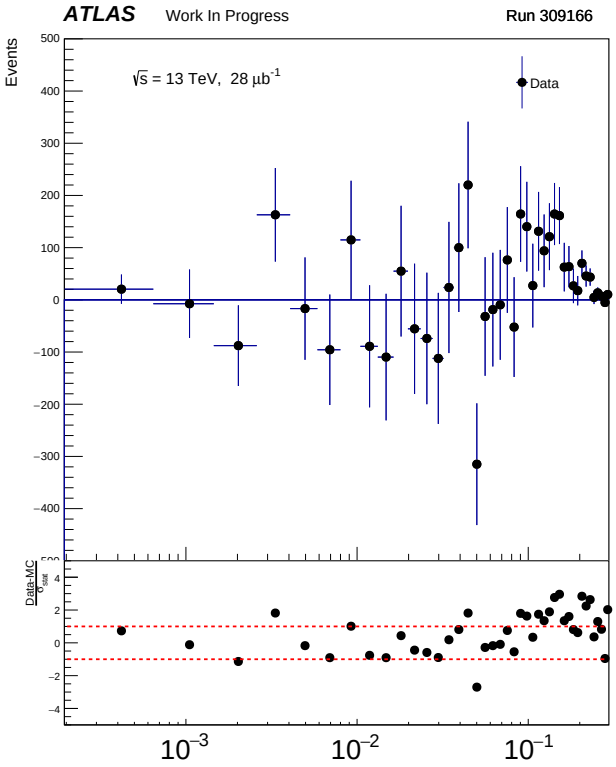

Figure 134: Fit over all available data for Arm 1 with scaled background and MC subtracted.

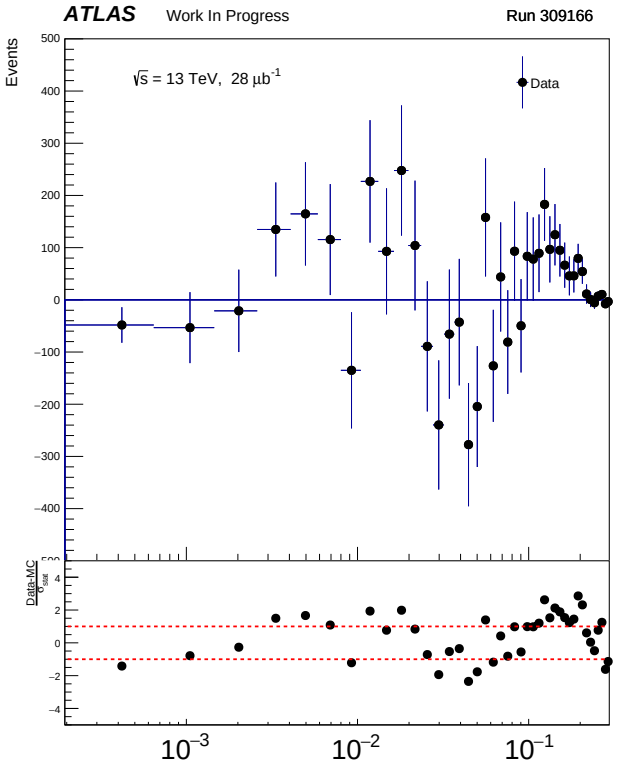

Figure 135: Fit over all available data for Arm 2 with scaled background and MC subtracted.

8 Conclusion and Outlook

A measurement of the total p-p cross-section was achieved by building a Monte Carlo simulation describing the behavior of elastically scattered protons at the LHC and comparing this to ALFA elastic data, including all known detector effects and cuts to ensure as pure a sample as possible. This was achieved through a fit of the differential cross-section between the data and simulation by varying the total cross-section and the other parameters of interest: the ratio of the real and imaginary parts of the scattering amplitude, ρ and parameterization factor B, in order to obtain the closest description to the observed distribution.

The preliminary total p-p cross-section for *Run 309166* was measured to be:

$$\sigma_{tot} = 105.716 \pm 0.129(\text{stat.}) \pm 1.295(\text{syst.}) \text{ mb} \tag{82}$$

Furthermore, the preliminary ρ and B parameters were measured to be:

$$\rho = 0.119 \pm 0.009(\text{stat.}) \pm 0.038(\text{syst.}) \tag{83}$$

$$B = 20.671 \pm 0.062(\text{stat.}) \pm 0.066(\text{syst.}) \text{ GeV}^{-2} \tag{84}$$

The MC poorly described the data observed. Further analysis of the distributions revealed that the time period chosen to make the measurement affected the result of the cross-section fit significantly. It was also noted that the fit produced inconsistent results between detector arms for the later time period in the data. Numerous causes of this effect were considered, specifically time evolution of the emittance due to the large disparities in the resulting nuisance parameter value as well as time-dependence of the detector quantities such as the track reconstruction efficiency, background contribution and distribution of events in each arm over time. Specifically, the primary contribution to the poor χ^2 overall was found to be in Arm 2 for the period $8 < \ell < 107$ over the entire fitting range. In this case, the the MC appeared to underestimate elastics below $-t = 2 \times 10^{-2}$ GeV^2 and overestimate elastics above this value up until the fit range limit. The large Mandelstam t values outside of the fit range were also noted to be poorly described by MC by both arms in this time period. Of the investigated potential causes, no single one could alone described the behavior.

Anomalous peaks at $x \simeq \pm 5$ mm in LHC co-ordinates were also observed in the RUC background template that did not appear in the antigolden template or elastic sample. The *TIE Fighter* structure occurred even in unpaired bunches, which implied that the observed effect was not a consequence of proton scattering from the IP. Previous analyses of the background using the RUC method did not exhibit the *TIE Fighter* effect. Currently, it is suspected that interaction with the collimators caused this result, though this is merely speculation at present. Furthermore, it is possible, given the large disparities between the RUC and antigolden templates in terms of distribution, that an unexpected contribution to background was observed that the scaling method could not account for. It should be noted, however, that the t-spectra of the scaled antigolden and combined RUC background template agreed well. The t-spectrum of the *TIE Fighter* was measured and an unexpected peak was observed at around $-t = 2 \times 10^{-2}$ GeV^2. The reasons for this are unclear.

Of further note is that the results produced by the MC fitting process appear to, in fact, produce a result within an volume in parameter space bounded by the error on the χ^2. This is due to the interdependency of the parameters of interest. It is clear then that the minimization procedure result may be better interpreted as providing bounds on the value of the three parameters of interest, rather than a specific minimized set of values. This arises due to the fact that the fit cannot change one variable without affecting the others.

In future analyses, it is likely that a more sophisticated model of the emittance and the track reconstruction efficiency may be required in simulation, since the time dependency appears to

contribute significantly to the result of the measurement. It is likely that further research into the new effects seen in the background template is required for further analysis. To this end, a full detector simulation of ALFA would be useful to determine if interaction with the LHC machine or some other detector-related phenomenon caused these new observations. In addition, it would also be of interest to see whether this effect occurs in future experiments. A future analysis may also seek, if possible, to decouple the parameters of interest that compose the differential cross-section into variables that are distinct from one another in order to tackle this problem.

Compared to previous analyses, *Run 309166* has defied expectations at a number of turns. It is hoped that in future analyses, any discrepancies will be resolved in order to calculate the total p-p cross-section at ALFA.

9 Appendix

9.1 Theory

9.1.1 Elastic Scattering from Beam Gas

A proposal discussed in this thesis is that there is a possibility that protons from the beam may scatter across quasi-stationary beam gas and that these protons may be incidentally observed by ALFA.

The temperature of the LHC beam pipe is around 5 K under a pressure of 10^{-7} Pa at the IP [17]. A typical beam gas particle is likely hydrogen, which has a mass that may be approximated to that of a proton. As such, the momentum of such a particle may be found to be:

$$p_{avg} = mv_{avg} = m_p\sqrt{\frac{2k_BT}{m_p}} \tag{85}$$

This constitutes a momentum of 28.431 MeV which is negligible compared to the mass-energy of the proton. This result consequently dramatically changes the centre of mass energy available to a collision with a 6.5 TeV proton. However, the elastic collision remains the same in the center-of-mass frame. The scattering angle of such a collision is discussed henceforth.

The total momentum of a fixed target experiment is:

$$\overrightarrow{p_1} + \overrightarrow{p_1'} = (E_1 + m_p) + p_1 \tag{86}$$

From this, the Lorentz β and γ to boost with may be derived from this expression:

$$\beta = \frac{\overrightarrow{p_1}}{p_1^0} \qquad \gamma = \frac{p_1^0}{|\overrightarrow{p_1}|^2} \tag{87}$$

Lorentz β may be found readily:

$$\beta = \frac{p_1}{(E_1 + m_p)} \tag{88}$$

Lorentz γ may be found by considering the absolute magnitude of the total energy-momentum four-vector of the system:

$$|\overrightarrow{p_1}|^2 = |\overrightarrow{p_1} + \overrightarrow{p_1'}|^2 = (E_1 + m_p)^2 + |p_1|^2 \tag{89a}$$

$$|\overrightarrow{p_1}|^2 = E_1^2 + 2E_1m_p + m_p^2 - |p_1|^2 \tag{89b}$$

Using the mass-energy relationship $E_1^2 - |p_1|^2 = m_p^2$,

$$|\overrightarrow{p_1}|^2 = \sqrt{2m_p^2 + 2E_1m_p} \tag{90a}$$

$$\gamma = \frac{E_1 + m_p}{\sqrt{2m_p^2 + 2E_1m_p}} \tag{90b}$$

The boost may then be applied by considering the Lorentz transformation for such a system:

$$\begin{bmatrix} E_B \\ p_B^1 \\ p_B^2 \\ p_B^3 \end{bmatrix} = \begin{bmatrix} \gamma E - \beta\gamma p^1 \\ -\beta\gamma E + \gamma p^1 \\ 0 \\ 0 \end{bmatrix} \tag{91}$$

where p^i refers to the i^{th} index of the four-vector. The scattering angle between the proton and the hydrogen nucleus is given by the ratio of the momenta in the lab frame. We may obtain this by boosting to the centre-of-mass frame, rotating by the angle at which the proton scattered, and then boosting back to obtain the new momenta.

The momentum of the outbound particle was scattered by some angle, θ, and thus the scattered four-vector must be rotated in order to obtain the new momenta. In a boosted frame, the rotated components are:

$$\begin{bmatrix} E'_{1,B} \\ p'^{,1}_{1,B} \\ 0 \\ 0 \end{bmatrix} \times \begin{bmatrix} 1 & 0 & 0 & 0 \\ 0 & \cos\theta & -\sin\theta & 0 \\ 0 & \sin\theta & \cos\theta & 0 \\ 0 & 0 & 0 & 1 \end{bmatrix} = \begin{bmatrix} E'_{1,B} \\ p'^{,1}_{1,B}\cos\theta \\ p'^{,1}_{1,B}\sin\theta \\ 0 \end{bmatrix} \tag{92}$$

Boosting back to the lab frame is achieved by simply changing the sign of β in the Lorentz transformation. We obtain

$$\begin{bmatrix} E'_1 \\ p'^{,1}_1 \\ p'^{,2}_1 \\ p'^{,3}_1 \end{bmatrix} = \begin{bmatrix} \gamma(E'_{1,B} + \beta\gamma p'^{,1}_{1,B}\cos\theta) \\ \gamma(p'^{,1}_{1,B}\cos\theta + \beta E'_{1,B}) \\ p'^{,1}_{1,B}\sin\theta \\ 0 \end{bmatrix} \tag{93}$$

The ratio between the momentum adjacent to the beam proton and the momentum perpendicular to this axis, $\frac{p'^{,1}_1}{p'^{,2}_1}$ is the tangent of the new angle, θ_{Lab}:

$$\tan\theta_{Lab} = \frac{p'^{,1}_{1,B}\sin\theta}{\gamma(p'^{,1}_{1,B}\cos\theta + \beta E'^{,1}_{1,B})} \tag{94a}$$

$$\tan\theta_{Lab} = \frac{\sin\theta}{\gamma(\cos\theta + \beta\frac{E'^{,1}_{1,B})}{p'^{,1}_{1,B}}} \tag{94b}$$

$$\tan\theta_{Lab} = \frac{\sin\theta}{\gamma(\cos\theta + \frac{\beta}{\beta'})} \tag{94c}$$

where $\beta^{'}$ is the relative velocity of the particle in the centre-of-mass frame. Since in both frames the values of β and β' are asymptotically close to unity, they may be treated as such in the relativistic limit.

A further approximation allows:

$$\tan\theta_{Lab} = \gamma^{-1}\tan\frac{\theta}{2} \tag{95a}$$

$$\theta_{Lab} = \arctan(\gamma^{-1})\frac{\theta}{2} \tag{95b}$$

with a 6.5 TeV proton scattering from a fixed target, $\sqrt{s} = 110.434TeV$ and $\gamma = 58.867$.

For the other particle, which scatters with an angle ϕ, the particle scatters in the x plane with opposite direction to that of the forward propagating proton, such that $\cos(\theta) = \cos(\phi)$, $\sin(\theta) = -\sin(\phi)$ and $\beta_\theta = -\beta_\phi$:

$$\tan\phi_{Lab} = \frac{-\sin\phi}{\gamma(\cos\phi - \frac{\beta}{\beta'})} \tag{96a}$$

$$\tan\phi_{Lab} = \frac{\sin\phi}{\gamma(1-\cos\phi)} \tag{96b}$$

$$\tan\phi_{Lab} = \gamma^{-1}\tan(\frac{\pi}{2} - \frac{\phi}{2}) \tag{96c}$$

$$\phi_{Lab} = \arctan\gamma^{-1}(\frac{\pi}{2} - \frac{\phi}{2}) \tag{96d}$$

We see that the angles are now restrained an angle in the direction of the incident proton in the lab frame:

$$\theta_{Lab} + \phi_{Lab} = \arctan\gamma^{-1}\frac{\pi}{2} \tag{97}$$

Another point of observation is that the energy of the scattered proton is always measured to be greatest in the centre of mass frame. The boost will result in an apparent 'energy loss' that will affect the measurement of the energy in the lab frame of the particle.

In order to make a brief analysis of the energy loss scale, we return to the concept of boosting to the centre of mass frame, rotating and then boosting back. The energy following this may be shown to transform as:

$$E'_1 = \gamma(E'_{1,B} + \beta p'^1_{1,B}\cos\theta) \tag{98a}$$

$$E'_{1,B} = \gamma(E_1 - \beta p^1_1), \qquad p'_{1,B} = \gamma(p^1_1 - \beta E_1) \tag{98b}$$

$$\therefore E'_1 = \gamma(\gamma(E_1 - \beta p^1_1) + \beta\gamma(p^1_1 - \beta E_1)\cos\theta) \tag{98c}$$

$$E'_1 = \gamma^2(E_1(1-\beta^2\cos\theta) - \beta p^1_1(1-\cos\theta)) \tag{98d}$$

Taking the assumption again that, for highly relativistic particles $\beta \to 1$ and that for very forward scattering, $\theta \to 0$, Equation 98d may be rewritten to be:

$$E'_1 = \gamma^2(E_1(1-\beta^2\cos\theta)) \tag{99}$$

Then, using small angle approximation:

$$E'_1 \simeq E_1(\gamma^2 - \gamma^2\beta^2 + \beta^2\frac{\gamma^2\theta^2}{2}) \tag{100}$$

$$E'_1 \simeq E_1(\frac{\gamma^2\theta^2}{2}) \tag{101}$$

Therefore the perceived energy loss in the lab frame is directly proportional to the square of the scattering angle:

$$\frac{dE_1'}{dE_1} \simeq \frac{\gamma^2\theta^2}{2} \tag{102}$$

9.1.2 Track Reconstruction Probabilities

The independence of track reconstruction between sides gives rise to the following relations:

$$E_{1234} = P_{12} \cdot P_{34} \cdot E_{Total} \tag{103a}$$

$$E_{\bar{1}234} = P_{\bar{1}2} \cdot P_{34} \cdot E_{Total} \tag{103b}$$

$$E_{\bar{1}234} = P_{\bar{1}2} \cdot P_{34} \cdot E_{Total} \tag{103c}$$

$$E_{1\bar{2}34} = P_{1\bar{2}} \cdot P_{34} \cdot E_{Total} \tag{103d}$$

$$E_{12\bar{3}4} = P_{12} \cdot P_{\bar{3}4} \cdot E_{Total} \tag{103e}$$

$$E_{1234\bar{4}} = P_{12} \cdot P_{3\bar{4}} \cdot E_{Total} \tag{103f}$$

$$E_{\bar{1}\bar{2}34} = P_{\bar{1}\bar{2}} \cdot P_{34} \cdot E_{Total} \tag{103g}$$

$$E_{12\bar{3}\bar{4}} = P_{12} \cdot P_{\bar{3}\bar{4}} \cdot E_{Total} \tag{103h}$$

The value of the error may be estimated as per the following example, applied in all cases:

$$E_{\bar{1}2\bar{3}4} = p_{\bar{1}2} \cdot p_{34} \cdot E_{Total} = \frac{E_{\bar{1}234}}{p_{34}E_{Total}} \cdot \frac{E_{12\bar{3}4}}{p_{12}E_{Total}} \cdot E_{Total} \tag{104}$$

9.1.2.1 E_2

$$E_{\bar{1}2\bar{3}4} = \frac{E_{\bar{1}234} \cdot E_{12\bar{3}4}}{E_{1234}} \tag{105a}$$

$$E_{1\bar{2}\bar{3}4} = \frac{E_{1\bar{2}34} \cdot E_{12\bar{3}4}}{E_{1234}} \tag{105b}$$

$$E_{\bar{1}234\bar{4}} = \frac{E_{\bar{1}234} \cdot E_{1234\bar{4}}}{E_{1234}} \tag{105c}$$

$$E_{1\bar{2}34\bar{4}} = \frac{E_{1\bar{2}34} \cdot E_{1234\bar{4}}}{E_{1234}} \tag{105d}$$

9.1.2.2 E_1 and E_0

$$E_{\bar{1}\bar{2}\bar{3}4} = \frac{E_{\bar{1}\bar{2}34} \cdot E_{12\bar{3}4}}{E_{1234}} \tag{106a}$$

$$E_{\bar{1}\bar{2}3\bar{4}} = \frac{E_{\bar{1}\bar{2}34} \cdot E_{123\bar{4}}}{E_{1234}} \tag{106b}$$

$$E_{\bar{1}2\bar{3}\bar{4}} = \frac{E_{\bar{1}234} \cdot E_{12\bar{3}\bar{4}}}{E_{1234}} \tag{106c}$$

$$E_{1\bar{2}\bar{3}\bar{4}} = \frac{E_{1\bar{2}34} \cdot E_{12\bar{3}\bar{4}}}{E_{1234}} \tag{106d}$$

$$E_{\bar{1}\bar{2}\bar{3}\bar{4}} = \frac{E_{\bar{1}\bar{2}34} \cdot E_{12\bar{3}\bar{4}}}{E_{1234}} \tag{106e}$$

9.2 Supplimentary Information

9.2.1 Emittance

The emittances used in this thesis were extracted from the ATLAS LHC Operations eLog. The emittance

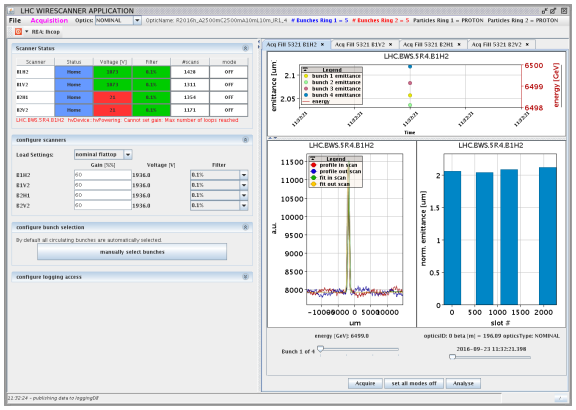

Figure 136: Beam 1 x emiytance.

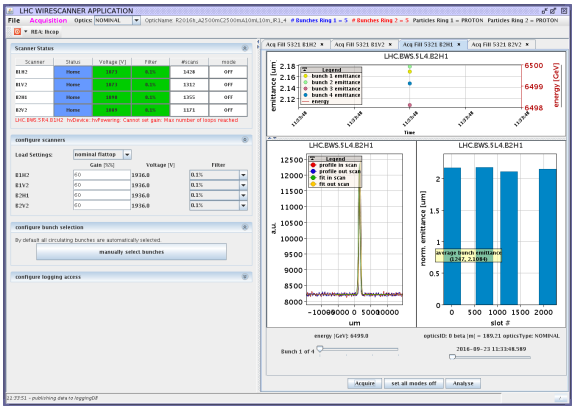

Figure 137: Beam 2 x emittance.

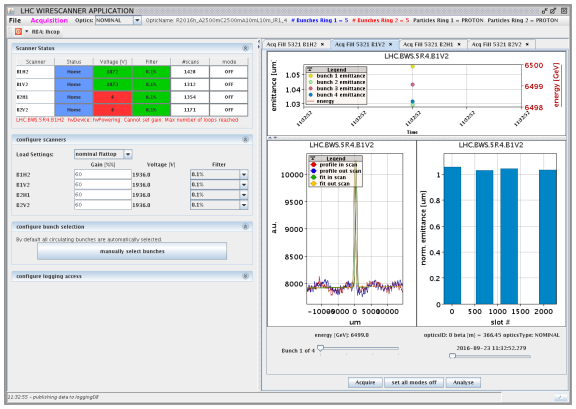

Figure 138: Beam 1 y emittance.

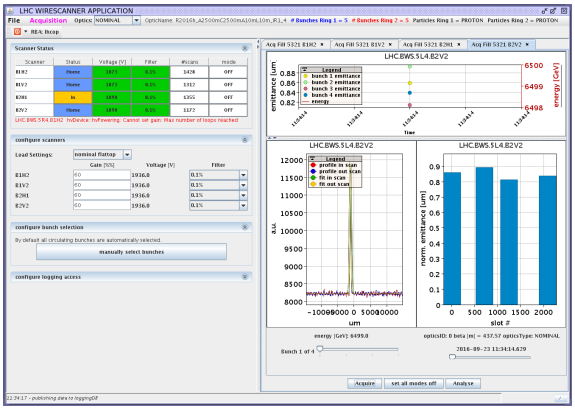

Figure 139: Beam 2 y emittance.

References

[1] "Standard model." https://en.wikipedia.org/wiki/Standard_Model.

[2] S. Jakobsen, P. Fassnacht, P. Hansen, and J. B. Hansen, "Commissioning of the Absolute Luminosity For ATLAS detector at the LHC," *Ph.D Thesis, University of Copenhagen.*

[3] P. Jenni, M. Nordberg, M. Nessi, and K. Jon-And., "ATLAS forward detectors for measurement of elastic scattering and luminosity," *ATLAS TDR 018, CERN/LHCC 2008-04.*

[4] S. Holm Stark, "Study of forward elastic pp scattering at $\sqrt{s} = 8$ TeV with the ALFA detector," *Ph.D Thesis, University of Copenhagen.*

[5] "ATLAS Beam Spot Summary." https://atlas-beamspot.cern.ch/webapp/summary/?type=DB_BEAMSPOT.

[6] ATLAS Collaboration, "Observation of a new particle in the search for the Standard Model Higgs boson with the ATLAS detector at the LHC," *Physics Letters B*, vol. 716.

[7] D. Green, *High p_T physics at Hadron Colliders.* OCLC: 729899578.

[8] P. Hansen, *Particle detectors and accelerators.*

[9] R. G. Newton, "Optical theorem and beyond," *American Journal of Physics*, vol. 44, pp. 639–642.

[10] J. D. Jackson, *Classical electrodynamics.* Wiley, 3rd ed ed.

[11] V. Kundrat and M. Lokajicek, "Coulomb and hadronic scattering in elastic high-energy nucleon collisions," *arXiv:hep-ph/0510040.*

[12] G. B. West and D. R. Yennie, "Coulomb interference in high-energy scattering," *Physical Review*, vol. 172, no. 5, pp. 1413–1422.

[13] TOTEM Collaboration, "Measurement of Elastic pp Scattering at $\sqrt{s} = 8$ TeV in the Coulomb-Nuclear Interference Region - Determination of the ρ-Parameter and the Total Cross-Section," *The European Physical Journal C*, vol. 76, no. 12.

[14] L. Alvarez-Gaume and M. A. Vazquez-Mozo, "Introductory lectures on quantum field theory,"

[15] "First successful beam at record energy of 6.5 TeV CERN." http://home.cern/about/updates/2015/04/first-successful-beam-record-energy-65-tev.

[16] "Taking a closer look at LHC - synchrotron radiation." http://www.lhc-closer.es/taking_a_closer_look_at_lhc/0.synchrotron_radiation.

[17] "LHC superconducting cable." https://lhc-machine-outreach.web.cern.ch/lhc-machine-outreach/components/cable.htm.

[18] "Detector & technology ATLAS experiment at CERN." https://atlas.cern/discover/detector/.

[19] F. Hgging and O. b. o. t. A. Collaboration, "The ATLAS Pixel Insertable B-Layer (IBL)," *Nuclear Instruments and Methods in Physics Research Section A: Accelerators, Spectrometers, Detectors and Associated Equipment*, vol. 650, no. 1, pp. 45–49.

[20] A. Sidoti, "Minimum bias trigger scintillators in ATLAS run II," vol. 9, no. 10, pp. C10020–C10020.

[21] O. Viazlo, "ATLAS LUCID detector upgrade for LHC Run 2," in *ATL-FWD-PROC-2015-004 ,The European Physical Society Conference on High Energy Physics.*

[22] "ATLAS eLogBook." https://op-webtools.web.cern.ch/elogbook/.

[23] "ATLAS Luminosity Public Results for Run 2." https://twiki.cern.ch/twiki/bin/view/AtlasPublic/LuminosityPublicResultsRun2.

[24] "INTERIM SUMMARY REPORT ON THE ANALYSIS OF THE 19 SEPTEMBER 2008 INCIDENT AT THE LHC," in *CERN/AT/PhL*.

[25] Burkhardt, Helmut and Persson, Tobias and Toms, Rogelio and and Wenninger, Jorg and Cavalier, Sophie, "Commissioning and operation at $\beta^* = 1000$ m in the LHC," in *Proceedings, 4th International Particle Accelerator Conference (IPAC 2013): Shanghai, China, May 12-17, 2013*.

[26] "ATLAS Luminosity Calculator." `https://atlas-lumicalc.cern.ch/`.

[27] L. Adamczyk, "Measurement of the total cross section in proton proton collisions at $\sqrt{s}$=7 TeV with the ALFA sub-detector of ATLAS," *23rd International Workshop on Deep-Inelastic Scattering and Related Subjects*.

[28] "Overview of diffractive physics." `http://www.cbpf.br/~gilvan/Proposal/node4.html`.

[29] P. A. P. Nghiem, N. Chauvin, W. Simeoni, and D. Uriot, "Beam halo definition and its consequences," in *Proceedings of HB2012, Beijing, China*.

[30] "Non-linearities: MIGRAD versus HESSE versus MINOS." `http://www.fresco.org.uk/minuit/cern/node32.html`.

[31] F. James and M. Winkler, "MINUIT user's guide."